EVALUATION OF THE THORAX OF THE MANDUCA SEXTA FOR FLAPPING WING MICRO AIR VEHICLE APPLICATIONS

THESIS

Brian C. Cranston

AFIT-ENY-12-D-03

DEPARTMENT OF THE AIR FORCE
AIR UNIVERSITY

AIR FORCE INSTITUTE OF TECHNOLOGY

Wright-Patterson Air Force Base, Ohio

AFIT-ENY-12-D-03

EVALUATION OF THE THORAX OF MANDUCA SEXTA FOR FLAPPING WING MICRO AIR VEHICLE APPLICATIONS

THESIS

Presented to the Faculty

Department of Aeronautics and Astronautics

Graduate School of Engineering and Management

Air Force Institute of Technology

Air University

Air Education and Training Command

In Partial Fulfillment of the Requirements for the

Degree of Master of Science (Aeronautical Engineering)

Brian C. Cranston, BS

December 2012

AFIT-ENY-12-D-03

EVALUATION OF THE THORAX OF MANDUCA SEXTA FOR FLAPPING WING MICRO AIR VEHICLE APPLICATIONS

Brian C. Cranston, BS

Approved:

Anthony Palazotto, PhD (Chairman) date

Lt. Col Jeremy Agte, PhD (Member) date

Mark Reeder, PhD (Member) date

AFIT-ENY-12-D-03

ABSTRACT

In the 1990's, DARPA awarded several contracts to companies to research, design, and construct a Flapping Wing Micro Air Vehicle (FWMAV).

The tobacco hornworm hawkmoth (*Manduca sexta*) provides an excellent model from which to gather knowledge pertaining to the development of a Flapping Wing Micro Air Vehicle (FWMAV). One of the major challenges in design of a FWMAV is the energy demanding nature of low Reynolds number flapping flight. Therefore, an understanding of the power required by the flight muscles to actuate the wings is essential for the design of a FWMAV. The *M.sexta* wing/thorax mechanism was evaluated as a mechanical system in order to gain insight to the mechanical power required to produce the full natural wing stroke. A unique dynamic load device was designed and constructed to mechanically actuate the upstroke and downstroke of the *M.sexta* in order to achieve the full flapping motion. Additionally, the forces applied through the flight muscles were directly measured in order to attain the power requirements of the flight muscles simultaneously. The experiment yielded wing stroke amplitudes of + 60 and – 35, which is what is seen in nature during hovering. The DVM and DLM muscle groups were calculated to have a power density of 112 W/kg with the vehicle energy density being 2 W/kg. The power output requirement indicates the need for a lightweight and energy-dense power source/actuator combination for the development of FWMAVs.

ACKNOWLEDGEMENTS

I would like to thank AFIT for sponsoring my thesis work and Dr. Palazotto for giving me the chance to develop and produce a unique experimental system to show what I am capable.

A. Table of Contents

LIST OF FIGURES PAGE

LIST OF TABLES PAGE

LIST OF ACRONYMS

AFIT – Air Force Institute of Technology

AFOSR – Air Force Office of Scientific Research

DAQ – Data Acquisition (board)

DARPA – Defense Advanced Research Projects Agency

DLM – Dorsolongitudinal Muscle

DoD – Department of Defense

DVM – Dorsoventral Muscle

FWMAV – Flapping Wing Micro Air Vehicle

fps – frames per second

IIT – Instrumented Indentation Testing

MAV – Micro Air Vehicle

***M.sexta* –** *Manduca sexta*

RoM – Range of Motion

UAV – Unmanned Air Vehicle

EVALUATION OF THE THORAX OF THE MANDUCA SEXTA FOR FLAPPING WING MICRO AIR VEHICLE *APPLICATIONS*

I. Introduction

Objective

The following research study examined the flapping flight mechanism of a biological specimen, the Hawkmoth (*Manduca sexta*). In examining the Hawkmoth, the structure and function of the thorax/wing mechanism was evaluated for application to Flapping Wing Micro Air Vehicles. The objective of this research effort is to quantify the power requirement for flapping flight of the Hawkmoth. The hawkmoth exhibits an indirect flapping mechanism, where in the muscles for flight is attached to a flexible segment of the exoskeleton. This mechanism functions utilizing a biological kinematic system to transmit the skeletal deflection to a wing deflection. Therefore, in order to quantify the power output of the moth the muscle/skeletal interaction must be investigated. The objective of this research effort is to quantify the power output of the main flight muscles (DVM, DLM) and power density during hovering flight conditions. To accomplish this goal a mechanical device was constructed that would actuate a euthanized *Manduca sexta* thorax such that the wings will flap though their natural frequency and flapping motion. The full flapping stroke was able to be reproduced in the *M.sexta* as well as instrumenting the vertical and longitudinal forces such that a power measurement was captured for the upstroke and downstroke. This power can then be attributed to each of the main muscle groups, the ventral and longitudinal muscles to attain a specific muscle power density for each group, which ideally would be the same if they are comprised of the same material.

Several different methods have been developed and tested with live and deceased *M.sexta* evaluating their muscle power output and more commonly used power density. Casey, in 1976 estimated the power density based on a calculated power input and an estimate of 20% efficiency. In 1983, Pennycuick estimated the power density of the flight muscle based on a known value of in mitochondria in the muscle. By the 1990's, Stevenson and Josephson studied the ventral muscles utilizing a work loop method which was performed on partially disconnected muscles. Another work loop method experiment was performed by Tu in 2004, where he studied the longitudinal muscle group. In 2009 Zhao determined the power density using a numeric approximation for the inertial forces and an experimental wing for the aerodynamic forces. The two were summed for the total power required for flight by the muscles. Lastly, in 2012 Hollenbeck utilizing some of the existing experimental set-up at AFIT estimated the power density for the ventral muscles using a unique dynamic load mechanism. This research work built upon and improved the work performed by Hollenbeck by being able actuate the entire wing stroke and quantify more accurately and precisely the power required for the DVM and DLM muscle groups simultaneously.

Motivation

Over the last decade, researchers and engineers have designed and built progressively sophisticated unmanned air vehicles (UAV). These vehicles have served military missions for surveillance and decoy applications. With the ever growing war front and increasing intelligence demands there is a desire for the next generation UAVs which are called micro air vehicles (MAV). Ideally, these vehicles would be able to fit in the palm of your hand and would be controlled autonomously or remotely from a local position in which the intelligence would be transmitted to a portable station. Current military UAVs require the vehicles to be carried in multiple parts to be assembled at the location of deployment (McMichael and Francis 1997). This process requires a safe environment to assemble and launch the reconnaissance vehicle. These vehicles wingspans range from 3 to 35 m. The proposed MAVs through DARPA would have wingspans from 7 to 15 cm and many would be able to be carried by military personnel and deployed at a moment's notice (DoD 1997). With technology ever advancing and feasibility of such air vehicles becoming a reality, there is a growing high level of interest in developing MAVs for military and civilian needs. The ability for these vehicles to be locally deployed and operated would reduce the latency exhibited by current reconnaissance vehicles. The desired technology onboard MAVs would be able to give the soldier or civilian operator "unprecedented situational awareness" (McMichael and Francis 1997). This envisioned level of direct connectivity between the user and the vehicle means that the user has to carry the vehicle and the interfaces associated with it. Hence the MAV "must trade favorably with other soldier assets - like water and ammunition. The system must also be affordable. It must have a vanishingly small logistics tail, and for many missions, it must be intrinsically covert. All this points to a highly compact, small system." (McMichael and Francis 1997). An MAV would be in a unique class of its own where the missions would be uniquely designed for the vehicle such as tight quarters within buildings or an environmental terrain where existing systems could not possibly operate.

The desire to build such a system comes with the need to understand how this system would operate. Currently knowledge about low speed aerodynamics for insect sized vehicles is fairly immature and undergoing substantial research. Quite interestingly in the 1930s at Gottingen University the first calculations of bumble-bee aeronautics indicated that the bee should not be able to fly, even though it clearly does, this became known as the bumble-bee paradox (Highfield 2007). It was not until the past decade, thanks to modern technology, that the bee was able to be investigated enough to show how exactly how it generates enough lift to attain flight of its "massive body". Utilizing high speed imaging techniques, it was found that the bee, as well as other insects and mammals, such as the locust, hawkmoth, and bat all flap in such a manner that the wings flex and change effective shape during their upstroke and downstroke to fly (Highfield 2007). Utilizing biomimicry to understand the flight mechanisms for a multitude of specimen would allow researchers and engineers an opportunity to characterize the mechanisms that they exhibit in nature. The knowledge gained from these studies would assist engineers in designing a well-tailored MAV or FWMAV for various mission requirements/profiles.

Using a variety of different models and approaches, there are three main systems of flight that are being examined in MAV research: fixed wing, flapping wing, and rotary wing flight. Using biomimicry for development ensures that a working and functional model is examined for use in experimental testing and design. Insights to be gained include wing/fuselage interactions or the maximal lift capabilities in a given environment.

Each group provides valuable information about natural flight characteristics which helps scientists to better understand how nature has evolved different flying mechanisms over time. In studying these mechanisms, the hope is that we can use these systems to our advantage.

This thesis will focus on one particular insect specimens, the hawkmoth *M.sexta* (Figure 1). The *M.sexta* exhibits all of the qualities that are desired in a Micro Air Vehicle. Specifically, this insect has developed through evolution for millions of years with the unique attributes that DARPA desires in MAVs by 2030 (Table 1) (DoD 1997). The mechanism(s) that enable the flapping motion are of great interest, and will be examined at length with an initial emphasis of first understanding the biological process. The process will be used to construct a testing apparatus to duplicate the thoracic forces produced by the moth in order to quantify the mechanical power required to replicate the flapping stroke of the moth.

Figure 1: *Manduca sexta*: Hawkmoth

Table 1: MAV Design Requirements [Sims, 2009]

Specification	Requirements	Details
Size	< 15.24 cm	Maximum Dimension
Weight	~ 100 g	Gross Takeoff Weight
Range	1 to 10 km	Operational Range
Endurance	60 min	Loiter Time on Station
Altitude	< 150 m	Operational Ceiling
Speed	15 m/s	Maximum Flight Speed
Payload	20 g	Mission Dependent
Cost	$1,500	Max Cost, 2009 (US Dollars)

Research Outline

The only way to accurately reproduce the natural flapping motion of *M.sexta* is to understand how the muscles attach to the exoskeleton, mainly the tergum, and how the muscles interact with the exoskeleton structure to produce wing movements. Previous research efforts have studied the neuromuscular impulses themselves that induce specific wing movements; here a different approach was taken in order to determine the power density of the flight muscles. The approach taken in this research was to mechanically actuate the *M.sexta* so that all natural boundary conditions remained intact in order to reproduce the natural flapping stroke and simultaneously recording the forces through the tergum itself.

This study will attempt to associate the forces sensed through the tergum as the forces that would have been generated from a live moth's flight muscles such that a specific power density of the muscles can be computed. This process will be performed by instrumenting push rods with strain gauges in such way that the thorax is actuated in both the vertical and longitudinal directions and the forces can be recorded to determine the specific power output. The moth will be actuated by a constructed mechanical device utilizing a kinematic linkage to perform both the vertical and longitudinal compression of the thorax with one degree of freedom (one actuator). At the same time of the actuation, and data acquisition a high speed camera will be recording the mechanism's movements as well as the moth's thorax and wing deflections. This will allow for an accurate correlation of the forces through the tergum and the respective thorax/wing displacements.

Document Overview

The research effort presented will be arranged in five chapters: Literature Review, Theory, Experimentation, Results, and Conclusions. Chapter II discusses the specie background and previous work that has been performed relating to the experimentation presented in the experiment chapter. Chapter III explains the theory utilized in the development and execution of the experiment. Chapter IV explains the experimental work conducted at the Air Force Institute of Technology MAV lab. Chapter V gives the results and analysis of the experiment presented. Chapter VI reviews the highlights of each of the preceding chapters to present conclusions and opportunities for future endeavors. Following this chapter is a series of appendices containing all of the Matlab scripts utilized in the execution of the experiment and data analysis, instrumentation documentation, complete FEA analysis, a sample set of images used during the signal processing, and presentation of the hawkmoth habitat. Finally, is a bibliography containing the many different references used in the preparation of this document is presented.

II. Background and Literature Review

This section will discuss background information detailing flapping flight, *M.sexta* characteristics, specimen structural anatomy, specimen flight muscle anatomy, and the flight mechanism. Additionally, current FWMAV projects will be discussed as well as research efforts pertaining to the objectives of this research.

Flapping Flight

As mentioned earlier, the three main systems of flight for MAVs are fixed, flapping, and rotary wing platforms, each having its own advantages and disadvantages. Fixed wing aircraft have the ability for high speed travel and long endurance yet require the need for a launcher; rotary wing aircraft have good hovering performance and the ability for vertical takeoff and landing, yet can have gust sensitivity. These first two forms of MAV flight platforms are fairly well understood and widely established. In looking at flapping flight vehicles such as insects, birds, and small mammals e.g. bats, all exhibit good hovering performance, high maneuverability and stability. The flapping platform, which is seen throughout nature, is an evolutionarily proven flight mechanism for vast arrays of low Reynolds number flight conditions. Flapping flight is particularly subject to the effects of low Reynolds number flight. These effects extend from wind gusts to unstable aerodynamic flow and viscous dominated flow (Shyy 2008).

As stated by Muller “The flapping motion of flexible wings has been considered one of the most graceful and efficient kinds of animal locomotion” (Mueller, Fixed and Flapping Wing Aerodynamics for Micro Air Vehicle Applications 2001). Not until the past twenty years has flapping flight for low Reynolds number really been investigated. Until then, the aerodynamics associated with flapping flight was unclear. The specific functionality of being able to provide low speed aerodynamic stability and propulsive thrust utilizing a single mechanism is what makes flapping MAVs a desired vehicle platform. Below is a description of how flapping flight is created:

“Using only these two degrees of freedom (flapping and feathering), there are 3 important variables with respect to wing kinematics: wing beat frequency, wing beat amplitude, and wing feathering as a function of wing position. When coordinated, these motions can provide lift not only on the down stroke, but also on the up stroke. The ability to generate lift on both strokes results from a change in the angle of attack of the wing. The ability to generate lift on both the up- and down-stroke leads to the potential for hovering flight in entomopters and ornithopters.” (Upton 2005) Being able to understand the kinematics of biological flapping flight has the potential to inspire many new waves of FWMAVs.

Over the past ten years there has been a large surge of development in very small flapping wing vehicles. Presently there are many bio-inspired FWMAVs at various stages of development. Companies and Institutions such as AeroVironment, Inc, Wright State University, Harvard University, and TU Delft have created functioning forms of flapping wing micro air vehicles. AeroVironment in 1998 created, and successfully flew the first FWMAV the “microbat” for 9 seconds. Since then, AeroVironment has redesigned the bat and has increased flight time to 9 minutes. AeroVironment were also contracted by DARPA in 2009 to work on producing a Nano Air Vehicle which was inspired by the hummingbird. AeroVironment as of 2012 has been able to design and build a FWMAV which has exceeded all of DARPAs technical milestones for a NAV (Harvard 2012).

Wright State University over the past few years has developed several FWMAVs bio-inspired insects such as the dragonfly, butterfly, ladybug and cicada. These vehicles operate under a geared motor which powers the wings in a clap and fling mechanism in order to achieve flight. Some of their vehicles have the ability to fly for as long as 20 min and a few can even carry small payloads such as cameras (WSU 2011).

Harvard University's Microrobiotics Laboratory has been able to utilize in house developed microrobotic actuators to design and manufacture a flapping wing vehicle the size of a quarter resembling a bee. This FWMAV utilizes piezoelectric flapper mechanisms to individually flap each wing of the vehicle. They have been able to achieve flight and some control topology with this vehicle, yet the vehicle has a tethered power source and cannot fly under a carried power source (WSU 2011).

TU Delft in 2005 began development of the DelFly I. This project began as an attempt to create a flapping air vehicle that would operate in the very low Reynolds number regime that fixed wing aircraft have difficulty performing. Aerodynamic performance is maintained longer when the wings are flapping instead of fixed. This MAV resembled a dragonfly in nature and was able to carry its own power source, a camera, and a video transmitter. From here the DelFly II was constructed, being a micro air vehicle weighing in at 17 grams still having the capability of carrying a camera and transmitter. This vehicle had an operational time of 17 minutes and the potential to achieve out of line of sight operation. As of 2008 TU Delft is working on an even smaller micro version weighing only 3 grams with a camera and transmitter on board (Delft 2012).

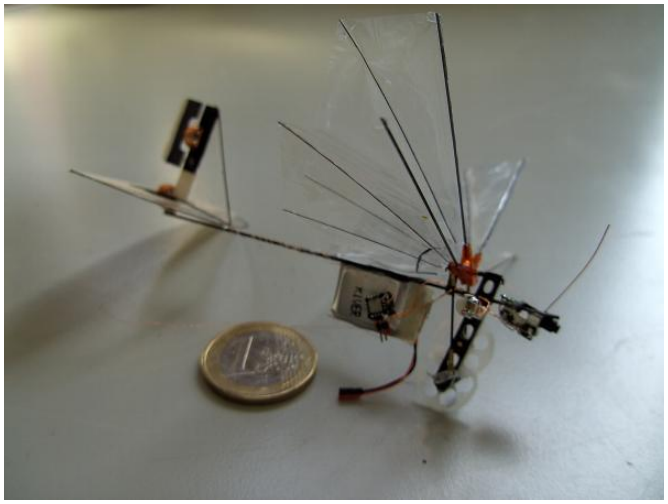

Figure 2: TU Delft DelFly size comparison to a euro.

M.sexta Selection/Investigation

The *Manduca sexta* also known as the Hawkmoth or Tobacco Hornworm Moth is an ideal specimen to study for its size, hovering ability, and remarkable flight stability. The *M.sexta*, according to aerodynamic calculations, has one of the lowest costs for hovering flight (Casey, Flight Energetics of Sphinx Moths: Power Input During Hovering Flight 1976). The *M.sexta* as described by M. A. Frye: 'This nocturnal forager hovers at individual flowers set against a spatially complex and dim visual background while maintaining stability in often turbulent winds" (Frye 2001). Beyond that the *M.sexta* is widely used in current and past lab experiments, has ideal flight speed, wing span, wing loading, maneuverability, gust response, aspect ratio, flight Reynolds number and endurance. All of these attributes are critical to developing a successful FWMAV. **Error!**

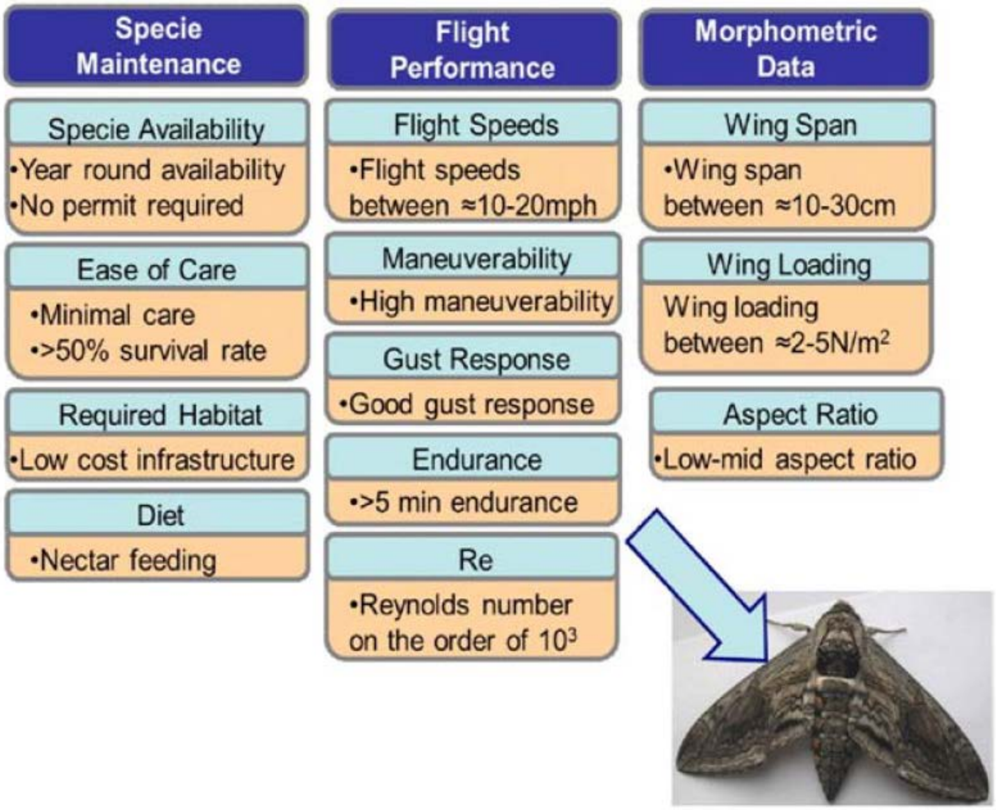

Reference source not found. is a chart displaying specimen maintenance, flight performance, and morphometric data on the hawkmoth as prepared by Guiler (Guiler 2011). This chart further validates the selection of the hawkmoth for investigation for FWMAV; the hawkmoth exhibits all of the size and flight performances that are desired in a FWMAV.

In addition to the exceptional flight characteristics of the *M.sexta* it also exhibits an exoskeleton only seen in insects containing elastic proteins that enable the thorax to efficiently operate as a mechanical spring damper at resonance during flapping flight (Bolsman 2010). For wing actuation, the *M.sexta* has two fairly simple and easily isolated muscle groups. These are known as the dorsolongitudinal and dorsoventral muscle groups. For the purposes of this research effort the areas of interest that are the main focuses are the thorax and the muscle groups of the *M.sexta*.

Figure 3 – Dorsal view of *M.sexta* coloration (scale is in centimeters)

Thorax and Exoskeleton

The body of the *M.sexta* is divided into three major subdivisions which are the head, thorax and the abdomen. The head contains the brain, compound eyes and the proboscis used for feeding. The thorax contains the two main muscle groups for flight and the connections for the legs and the wings of the moth to the exoskeleton. The abdomen contains the organs for digestion, reproduction, and blood circulation.

The exoskeleton of the moth serves not only as a protective covering, but also an elastic surface for muscle attachment. The structure consists of four layers: epicuticle, procuticle, epidermis, and basement membrane. The focus here is the middle layer which is the procuticle. The procuticle is comprised of microfibers of chitin enveloped by a matrix of protein. When the procuticle forms, it is similar to that of a carbon fiber layup. There is a thin layer of lamellae with chitin microfibers oriented at different angles throughout the layup. This layer can in some parts of the body morph into a hard outer layer. This layer, as it forms, can have a differentiation of material properties throughout the exoskeleton. This differentiation occurs when the specimen molts. The outermost layer is a protective waxy like coating that protects the specimen from water loss and invasion of foreign material (Meyer 2006).

For the *M.sexta*, the thorax is the single largest continuous section of exoskeleton. This is common as with other specimens that utilize an indirect flight mechanism. The thorax/tergum absorbs and returns substantial amounts of internal energy during flapping flight. As the wings elevate and descend, a large amount of kinetic energy are produced which must be counteracted during stroke reversal (Wu, Stanford and Ifju 2009). Therefore, if the tergum were a rigid plate and no bending occurred, the amount of energy required by the muscles to counteract the kinetic energy of the wings during flapping flight would be tremendous. The bending of the tergum allows for inertial energy to be stored during flexure and released during relaxation. This property is inherent in elastic materials and some composites. For flapping efficiency it has also been shown that insects with indirect flapping mechanics flap near or at the resonant frequency of the system (Khan and Agrawal 2011).

M.sexta Flight Muscles

This research will focus primarily on the two major power producing muscles in flying insects, the dorsal longitudinal muscles (DLMs) and the dorsal ventral muscles (DVMs).

The DVMs are the elevator muscles that indirectly cause the upward movement of the wings in all insects. This occurs because when the DVM muscles are contracted, they pull down the tergum (dorsal surface of the thorax), which moves the point of articulation of *M.sexta*'s wing down as well (Figure 4) (Chapman 1998). In most insects (including *M.sexta*), the downward wing (depression) is caused indirectly when the DLMs contract; then, the center of the tergum becomes bowed upward, and this moves the upper wing joint upward and the wing flaps down (Figure 4C) (Chapman 1998).

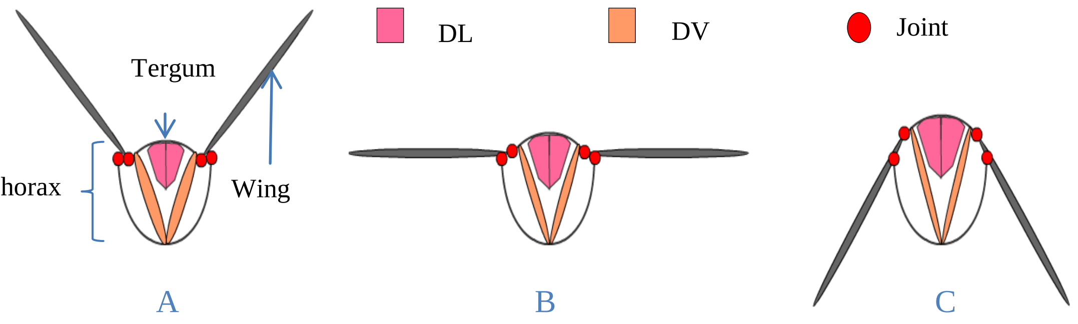

Figure 4: A cross-sectional view of a *M.sexta* thorax showing the primary flight muscles: A) DVM contracting, causing an up-stroke; B) DVM relaxing, while the DLM begins to contract; C) DLM contracting, causing a down-stroke

M.sexta is amongst the largest of all flying insects. Their flight is powered by two sets of synchronously activated muscles in the thorax (Figure 5). The DLMs are the largest muscles in the moth, comprising 5-8% of the total body mass (Tu and Daniel 2004). The activation of these muscles can easily be detected with EMG because these synchronous muscles are usually activated only once in each wing stroke (Kammer 1971). During flight, the DLM muscles function exclusively

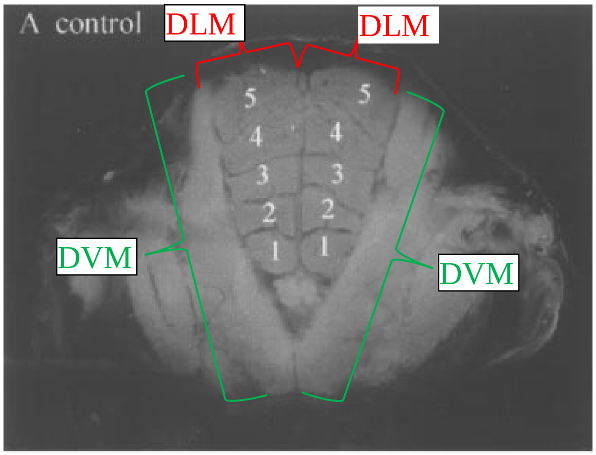

Figure 5: X-ray cross section of *M.sexta* thorax indicating the 5 muscle fiber bundles of each

to generate the mechanical power used to depress the wings by compressing the thorax from the head to the abdomen in the longitudinal direction. (Tu and Daniel 2004). The DVMs compress the thorax in the vertical direction to power the wing up-stroke (Bertrand, Regnier and Daniel 2008).

The DLMs and DVMs are made up of multiple muscle units (MU). The DLM has five muscle units or bundles (DLM 1-5) (Figure 6). The DVMs have six muscle units. The muscle units are controlled by motoneurons which electrochemically signal the contraction of the muscle fibers. (Bayline, Duch and Levine 2001).

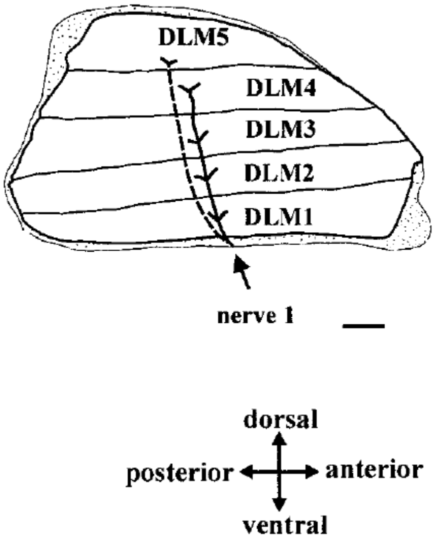

Figure 6: Side view depiction showing the motoneuron (MN1-4 solid and MN5 dashed) placement in the muscle.

Another related fact is that in the *M.sexta* and other insects, there is a one-to-one correspondence between electrical potential recorded from the nervous system and the time it takes for the muscle to shorten and relax, which means that one signal produces one wing movement; this is not the case for insects that have asynchronous flight muscles (Chapman 1998).

Literature Review

The following sections detail a series of experimental and analytical methods that have been implemented over the past forty years with the main focus on determining the specific power density of the Manduca sexta flight muscles. The methods range from direct muscle studies, oxygen consumption during flight converted to power output, indirect muscle studies, and mechanical actuation of the thorax/flight muscles for power output. Each of these methods has obvious benefits and detriments it their techniques to compute the power density of the flight muscles.

Power Input Method

One of the earlier attempts to determine the power density of moths was performed by Timothy Casey of The University of California in 1976. The method that Casey followed was study of the power input during hovering flight and was based off of an assumed muscle efficiency yielding power output density. In order to compute the measured power input the specimens' metabolic rates were recorded. The metabolic rates were determined by placing the specimen in a jar with a known amount of air and the specimen were induced to hover for at least two minutes time. From here samples of chamber air were collected and analyzed utilizing an oxygen analyzer. The rates of oxygen consumption were then converted to energy by assuming fat utilization during flight. The average value for power input of the Manduca sexta was 237 W/kg. The mass value here is the entire mass of the specimen. Based on an assumed 20% efficiency factor, the power output was calculated from the measured power input. This value was compared to calculated power requirements based on momentum theory and blade-element theory of helicopter aerodynamics. The calculated output power density using the 20% efficiency factor was 47 W/kg for the entire specimen weight. However, in just looking at the muscle power density, if the muscle mass was assumed to be 20% of the entire body mass that would yield a value of 237 W/kg for the muscles themselves (Casey, Flight Energetics of Sphinx Moths: Power Input During Hovering Flight 1976).

Muscle Study Method

Another unique effort pursued by C.J. Pennycuick in 1983 was to look at muscle power density from an anatomical point of view, studying the mitochondria in the myofibrils within aerobic muscle groups. Under this computational method, stress and strain values were assumed for the muscle myofibrils during shortening. For this method the volume of mitochondria is assumed to be directly proportional to the mechanical output of the muscle fiber itself. It was later assumed that if the specimen's muscles operate at high frequencies, greater than 10 Hz, then the dominate variable in determining the mechanical power output is within the mitochondria. If this is true then a value for specific power output could be determined of any aerobic muscle with the use of an electron micrograph. For this experiment, muscle fibers were extracted from two specimens of birds and analyzed for their mitochondrial densities. From here, and with all of the assumptions made, values of specific power output vs. operating frequency were obtained for fibrillar and non-fibrillar muscles. This chart is shown in Figure 7. In comparing this information to hawkmoth flight conditions estimates of power density can be obtained. For the fibrillar muscles, under an operating frequency of 25-30 Hz, the power density of the muscles according to Pennycuick is estimated to be 82-97 W/kg (Pennycuick and Rezende 1984).

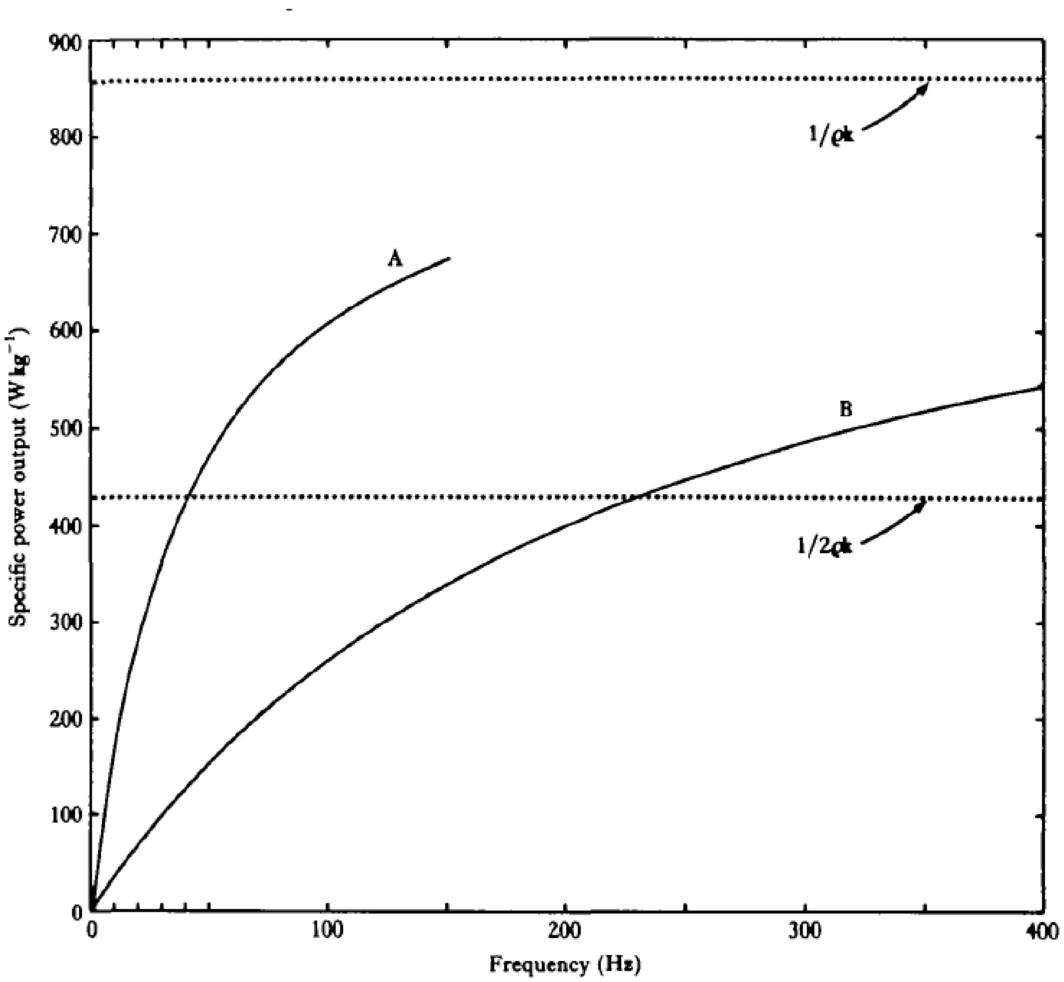

Fig. 6. Estimated mass-specific power output plotted as a function of operating frequency for (A) non-fibrillar, and (B) fibrillar muscle, from equation 17. The respective values for stress and strain are taken from Table 1, and k, the inverse power density of mitochondria, is taken to be $1{\cdot}1\times10^{-6}\,\mathrm{m}^3\,\mathrm{W}^{-1}$. The upper dotted line is the asymptote for both curves, and the lower one corresponds to $q = 1$, that is, equal volumes of mitochondria and myofibrils.

Figure 7: Specific power output plotted as a function of operating frequency. *M.sexta* falls under line (B).

Work Loop Method

The work loop method was a technique developed by Bob Josephson in 1985, in which electronic signals are measured from the muscle fibers themselves. This allowed a characterization of the muscle neuron signals during contraction and relaxation. The method utilized *in vivo*, an experiment using the whole living organism, ("within the living") simulation of muscles in order to determine their mechanical function. Many animals in nature employ rhythmic operation of muscle units. These units are phasically controlled, where a pulse of neural stimulation occurs with each cycle muscular movement. When the muscles are stimulated, a force is generated which usually shortens the muscle unit. In utilizing the work loop technique, forces are measured within an isolated muscle while cyclic length changes and phasic stimulation patterns are imposed. In recording these forces, as well as length changes, a force vs. length loop is generated in which the area within equals the mechanical work performed by the muscle. The force generated during the shortening/contraction of the muscle generates the work output from the muscle on its environment. Likewise, the force generated during the lengthening/relaxation of the muscle generates the work input to the muscle from the environment. This is shown in Figure 8. In order to calculate the total work performed for the cycle, the work input is subtracted from the work output. This yields the work per cycle performed by the muscle. Typically, a muscle generates positive work when the force peaks during the shortening portion of the total cycle. From here, the power created by the muscle can be calculated by taking the area inside the work loop, divided by the time required to complete the loop (Ahn 2010).

When utilizing this method, there are two different types of muscles that can be assessed, which are asynchronous and synchronous. Asynchronous muscles are muscles that do not require a pulse from a neuron for every contraction; this is how very high flapping frequencies are achieved. Synchronous muscles are muscles that do require a pulse from a neuron for every contraction. Most muscles are synchronous muscles. The main source of complication in employing this method is that the fashion in which the muscles are stimulated is extremely specific and replicating how this is done *in vivo* can be tasking. It has been shown that any deviation in how the stimulation occurs has a considerable effect on muscle work and power. Yet, if performed with great care and exactness the work loop method is a very valuable method in evaluating muscle work and power performances.

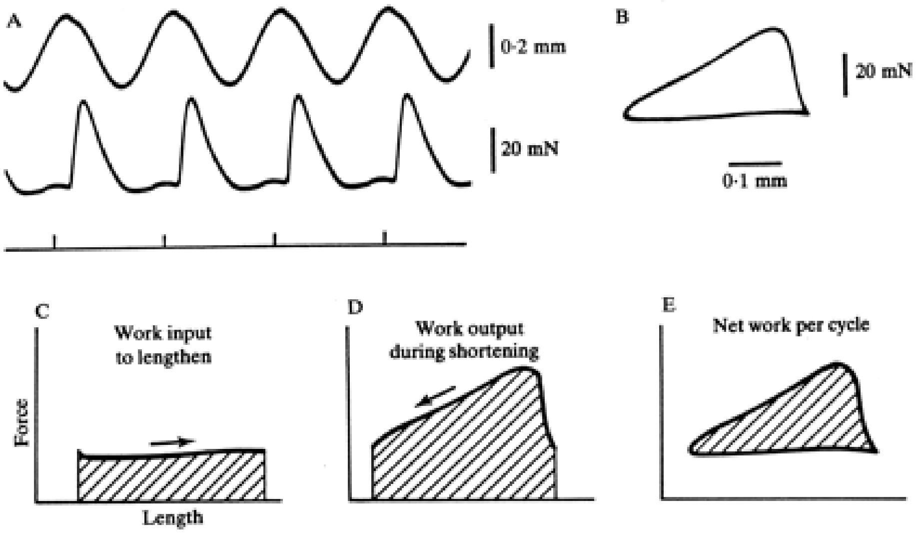

Figure 8: Work loop technique: Work measurement process and determination of the Work.

Josephson in 1989 along with R.D. Stevenson studied the *Manduca sexta* first dorsal ventral flight muscles utilizing the work loop method. The results of their experiment showed that there is an optimal temperature and frequency to operate the flight muscles to maximize the power output. At all optimal settings, muscle temperature of 40 deg C and frequency of 28.3 Hz, the calculated maximum power density of the muscle unit was 90 W/kg (Stevenson and Josephson 1990).

In addition to the work performed by Josephson, Tu and Daniel in 2004, used the work loop method developed by Josephson to determine the submaximal power and maximal power produced by the dorsolongitudinal muscles of the hawkmoth. Their results were a value of 83.3 W/kg for maximum power output and 47.4 W/kg for submaximal power output under observed *in vivo* flight conditions. An interesting point made by Tu and Daniel was that the “aerodynamic power generation by the wings may not be directly coupled to variation in mechanical power generation by the DL muscles.” (Tu and Daniel 2004).

Inertial and Aerodynamic Power Method

In 2009, Zhao and Deng took an inertial and aerodynamic approach to determine the power consumption during hovering flight for the *Manduca sexta*. An experiment was carried out in which both analytical and experimental methods were used to investigate the power consumption by the moth’s wings. During the analysis, the forewings of the moth were the main focus of the study. It has been shown that the hindwings are unnecessary for normal flight. For the experiment, a flapper, as well as a model wing, was constructed to perform the experimental portion of the experiment. The inertial forces were calculated based on wing kinematics and mass distribution equations and modeled numerically. The aerodynamic forces were measured using the constructed wings, and then scaled to the forces on insect wings. The results of the experiment showed that the peak aerodynamic forces were greater than that of the inertial forces, however the mean powers were almost equivalent. The average aerodynamic and inertial power was 11.8 mW and 9.8 mW, respectively. A correlation can be made utilizing the aerodynamic and inertial power obtained by Zhao and Deng to a power density of *Manduca* flight muscles. If it is assumed that the combined aerodynamic and inertial power is produced by the flight muscles, then a power density of the muscles can be extracted. Assuming a moth's average weight of 2 grams and 20% of that mass composed of the muscles, a power density combining the two forces would yield a 54 W/kg power density (Zhao and Deng 2009).

Dynamic Load Technique

The dynamic load technique is a method developed by Alex Hollenbeck of AFIT. A mechanical load is applied dynamically to a euthanized specimens thorax in such a manner that mimics the muscle interactions. This method currently can only be applied to specimen that employs an indirect flapping mechanism. For this method, a mechanical device was constructed that dynamically compressed the thorax of a hawkmoth at its natural flapping frequency to reproduce the upstroke of the moth. Using a load beam balance setup, the force transmitted through the thorax was recorded in order to compute the power density of the dorsal ventral muscles. The power density was computed by taking the recorded force and displacement measurements to calculate the work output for an individual upstroke. This work was then divided by the time over which the force was imparted over to get the corresponding power output. Form here, the power density is simply the power output divided by the mass of the DVMs. This method's unique advantage is that it allows the studied muscle group to keep all its natural boundary conditions intact during testing. The results of this experiment showed the power density of the dorsal ventral muscles spans between 72-143 W/kg based on a flight muscle ratio of 15-30% of the total muscle mass (A. C. Hollenbeck 2011).

This research effort will further the work performed by Hollenbeck and obtain the entire power output necessary for hovering flight of the *M.sexta*. The experiment will actuate the moths' thorax in the vertical and longitudinal directions in order to reproduce the entire wing stroke, whereas Hollenbeck only characterized the vertical compression or the upstroke portion of a flap. The research will be the first to simultaneously characterize both the DVM and DLM muscles groups with a single testing procedure as well as leaving all boundary conditions intact. The power density for both muscle groups will be able to be determined utilizing the load cell data in the respective compressive directions.

III. Theory

The following chapter is related to the mathematics and physics theory utilized to perform the objective research work. The linkage kinematics section explains the physics and kinematics relevant to the linkage design and functionality. The specific power density section describes the equations and methodology used to in order to compute the power output from the thorax during the dynamic load experiment. The signal sampling section describes the equations used to analyze and condition analog signals used for the data acquisition for the dynamic load experiment.

Matlab

The programming software utilized for the data acquisition and processing for this research was Matlab. Matlab is a "numerical computing environment" which allows for matrix manipulations, plotting of functions and data, implementation of algorithms, creation of interfaces, and interfacing with other languages. Matlab was used to script many algorithms for the data acquisition and processing of the data developed in presented research experiment. All of the scripts are presented in Appendices B-F.

Linkage Kinematics

For the purposes of the dynamic load experiment, it was necessary to develop an experiment that would transform the existing experimental set-up to actuate the thorax in both the vertical and longitudinal direction as opposed to only the vertical direction. In order to accomplish this, two approaches were considered for the longitudinal actuation. The first consideration was a linkage system to actuate both the vertical and longitudinal compression with a single degree of freedom. The second was to duplicate the vertical compression method in the longitudinal direction, which would denote an additional shaker, amplifier, and actuator. Based off of resources available and superior design attributes, the first method was the system that was explored and developed.

Linkage systems are an assembly of bodies normally rigid to control forces and movement. The movement of the bodies or links is governed by geometric relationships. Connections between the links or bodies are known as ideally moving pivots. These pivots can be sliders, pinned rotations, and free moving pivots. The benefits in utilizing a linkage system are that it allows you to gain a mechanical advantage based on the design of the system and computable movements from each of the components in the system. An example of some common linkage systems can be seen in Figure 9. These systems can have a vast array of pivot and link arrangements in order to achieve almost any desired movement for an output(s) (Slocum 2008).

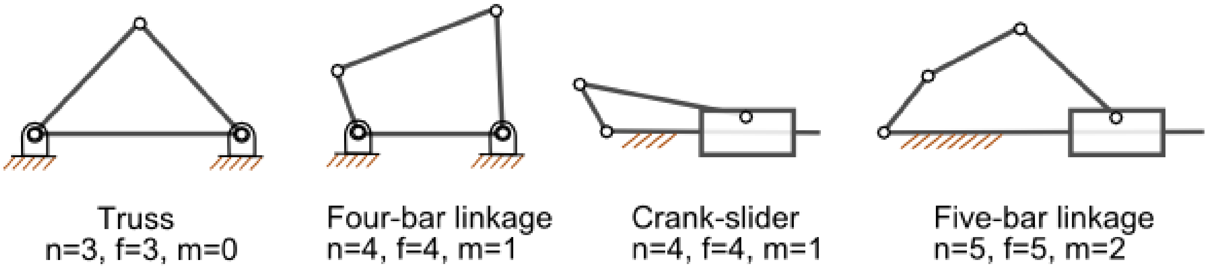

Figure 9: Various samples of multi-bar linkage systems: specifically noting the crank-slider.

The designed linkage system was decided to be a slider-crank mechanism and the equations relating the pivot and slider movement will be characterized below. The positional values of the pivot and slider are developed knowing three primary values: crank and shaft length and crank angle. Figure 10 shows a kinematic representation of a slider crank mechanism with the geometric relationships.

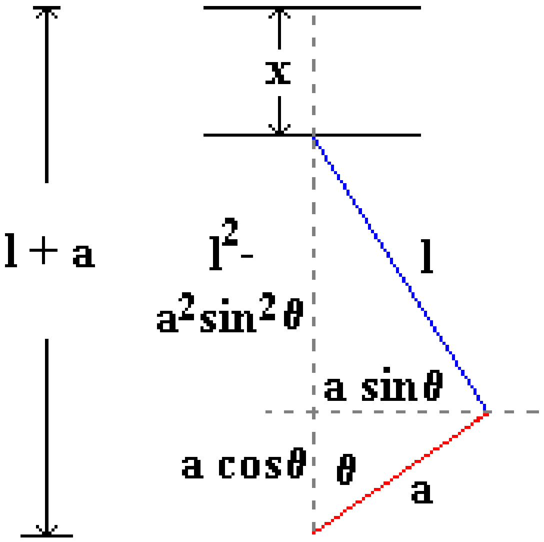

Figure 10: Geometric relationships of a slider-crank mechanism

The slider actuator displacement is denoted by Equation 1.

Equation 1

$$x = a + l - \left[(l^2 - a^2 \sin^2 \theta)^{1/2} + a \cos \theta\right]$$

The pivot point joining the connecting rod (*l*) and the crank (*a*) has a horizontal displacement shown in Equation 2.

Equation 2

$$y = a \sin \theta$$

In knowing the (l) and (a) lengths and the (x) displacement, the angle Ө can be back calculated by solving Equation 1 for Ө. With all of the unknowns established, all of the kinematics of the slider-crank mechanism can be determined.

Finite Element Analysis (FE)

Finite element modeling is typically used to analyze the structure of a system under a load in order to determine stress and strain values within the model. This methodology has been employed in various forms since the 1940's, yet then the original methods allowed for simple structural analysis to be performed by solving the stiffness parameter by hand. With modern advancements in computing technology, FEA has evolved past simple analysis to extremely complex analysis requiring large amounts of processing power and time. Finite element modeling was utilized in order to validate the assumptions made that the pushrods used in sensing the force signal are sufficiently stiff such that no deformation occurs during loading and unloading.

The first analysis presented will be for the vertical push rod, and the second will be for the longitudinal push rod. The material properties of both push rods are identical; the properties are shown in Figure 11. The mesh properties and image of the mesh for both the push rods are shown in Figure 12 and Figure 13. The displacement results from the FEA are displayed for both rods in Figure 14 and Figure 15.

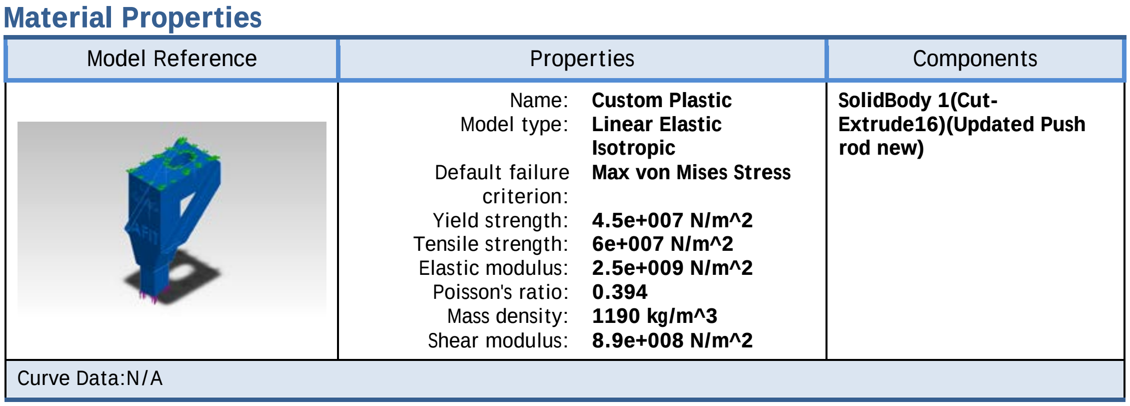

Material Properties

Model Reference	Properties	Components
	Name: **Custom Plastic** Model type: **Linear Elastic Isotropic** Default failure criterion: **Max von Mises Stress** Yield strength: **4.5e+007 N/m^2** Tensile strength: **6e+007 N/m^2** Elastic modulus: **2.5e+009 N/m^2** Poisson's ratio: **0.394** Mass density: **1190 kg/m^3** Shear modulus: **8.9e+008 N/m^2**	**SolidBody 1(Cut-Extrude16)(Updated Push rod new)**
Curve Data:N/A		

Figure 11: Material properties of the plastic-like 3D printed parts

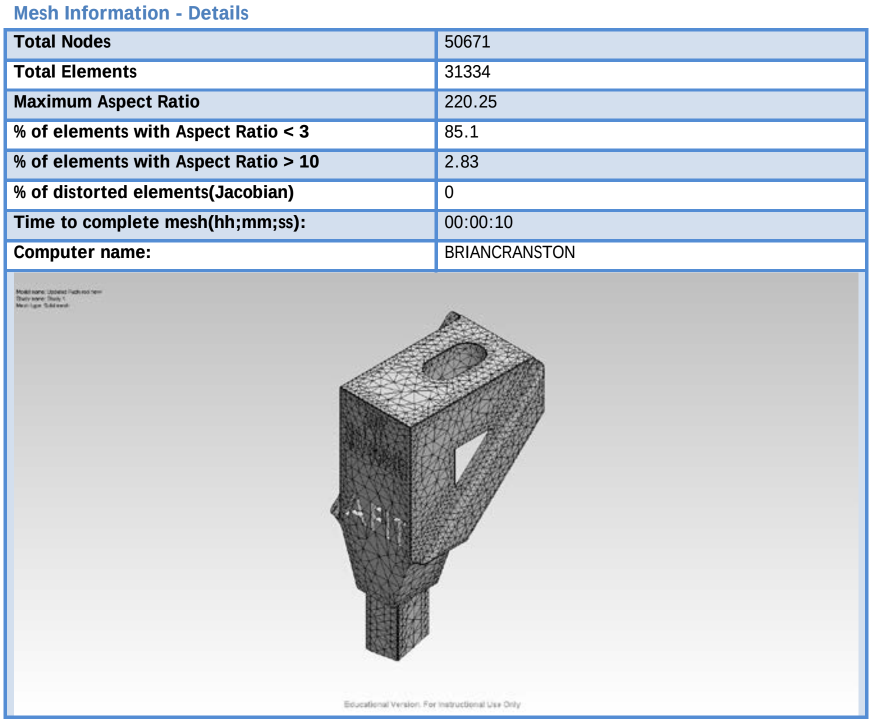

Mesh Information - Details

Total Nodes	50671
Total Elements	31334
Maximum Aspect Ratio	220.25
% of elements with Aspect Ratio < 3	85.1
% of elements with Aspect Ratio > 10	2.83
% of distorted elements(Jacobian)	0
Time to complete mesh(hh;mm;ss):	00:00:10
Computer name:	BRIANCRANSTON

Figure 12: Vertical push rod mesh and element details

Mesh Information - Details

Total Nodes	28887
Total Elements	17509
Maximum Aspect Ratio	10.211
% of elements with Aspect Ratio < 3	94.9
% of elements with Aspect Ratio > 10	0.0114
% of distorted elements(Jacobian)	0
Time to complete mesh(hh;mm;ss):	00:00:04
Computer name:	BRIANCRANSTON

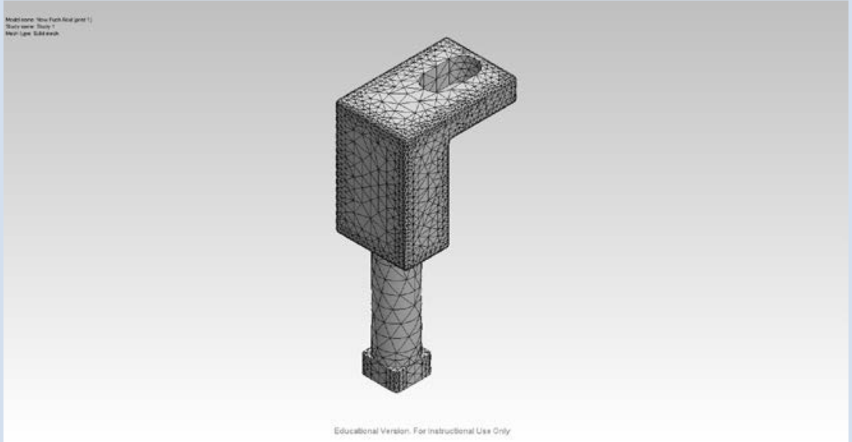

Figure 13: Longitudinal push rod and element details

Name	**Type**	**Min**	**Max**
Displacement1	URES: Resultant Displacement	0 mm Node: 34	1.7902e-005 mm Node: 1
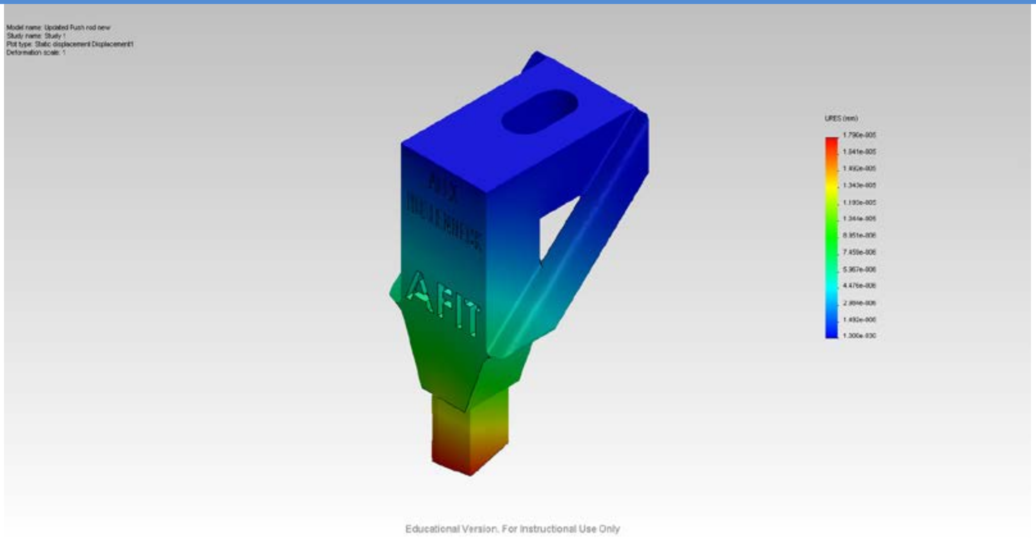 Updated Push rod new-Study 1-Displacement-Displacement1			

Figure 14: Vertical push rod displacement contour plot with min max displacements listed.

Name	Type	Min	Max
Displacement1	URES: Resultant Displacement	0 mm Node: 57	1.69527e-005 mm Node: 4409

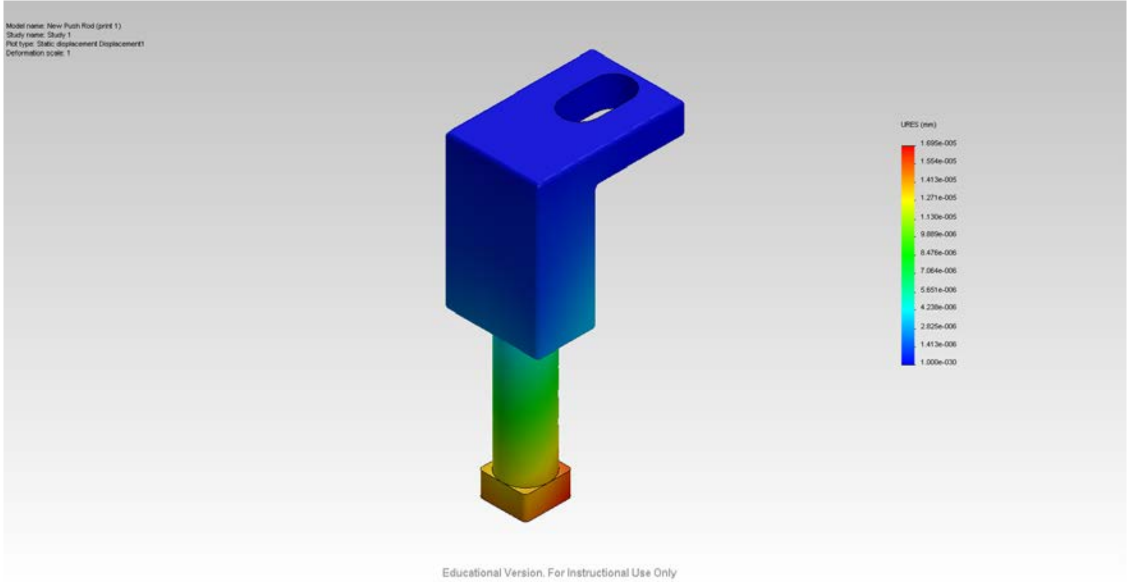

New Push Rod (print 1)-Study 1-Displacement-Displacement1

Figure 15: Longitudinal push rod displacement contour plot with min max displacements listed.

The rods were both modeled with 8 noded linear constant strain elements. Both rods were fixed at the top base and a maximum force obtained from test data was applied to the ends in contact with the specimen for the analysis. The area of interest for this analysis was the displacement of the loaded tip. The analysis produced a maximum displacement of 1.79x10^-5 mm and 1.69x10^-5 mm for the vertical and longitudinal push rods, respectively. The results from the analysis do show that the tip displacement is extremely small or negligible, therefore for the experiment; the rods will be treated as infinitely stiff where no displacement occurs. The FE modeling elicits all displacement that is produced from the actuation of the moth during the experimental testing to be only the displacement of the specimen and not of the rods themselves.

Specific Power Density

The specific power density and energy density are extremely useful values in determining the energetics of a material composition by weight. In general, higher values of power density are better than those of lower values. Typically, when investigating power densities of materials/fuels that are small, compact, and portable the main energy source is batteries. Commonly known battery types are those of the “dry cell” type, these include nickel-cadmium, nickel-zinc, nickel metal hydride, and lithium ion (ordered by increasing power density). This information is of importance when looking to compare the muscle power density of the specimen to available commonly used energy sources and actuators for FWMAV applications, which are mostly battery driven. The power density presented in the results chapter is computed from the force, displacement, and time data recorded using the dynamic load apparatus.

The first value to be computed is work. Work can be calculated by computing the area under the force vs. displacement curve, or the integral of the force with respect to the corresponding displacement. This is illustrated in Figure 16. Work is also calculated by explicitly integrating the force-displacement area.

Equation 3

$$W = \int_{x_1}^{x_2} F(x)dx$$

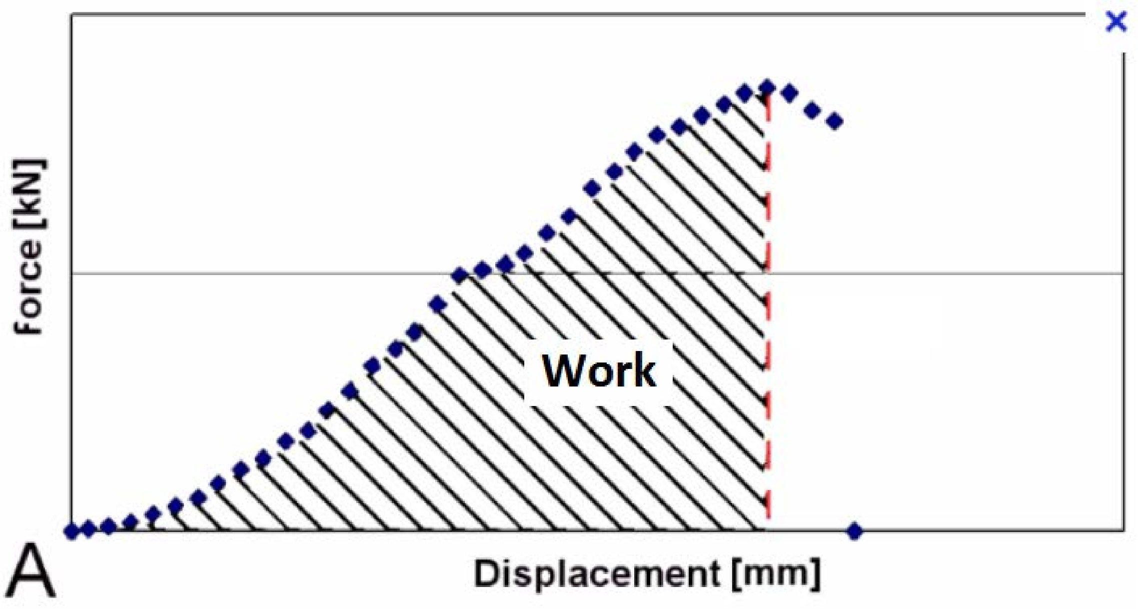

Figure 16: Example Force vs. Displacement plot, Work area under the curve

The trapezoidal rule was used in order to compute the area under the force vs. displacement curve. The trapezoidal rule is a numeric approximation where a function over an interval *a* to *b* is discretized over the entire interval. Small steps are taken and the function is evaluated at those points and added to each other and that quantity is divided by 2 and multiplied by the step size. The sum of all of the small steps is the area under the force vs. displacement curve. The expression is shown in Equation 4.

Equation 4

$$\int_a^b f(x)dx \approx (b-a)\frac{f(a)+f(b)}{2}$$

After the work has been computed, the raw power quantity is simply the work divided by the amount of time the work occurred over. Power is in units of Watts or Joules per second.

Equation 5

$$P = \frac{W}{t}$$

From here the specific power density is the power computed from the work and time divided by the mass of the material/object that is performing the work. Hence, a large power density means the material can deliver large amounts of power for little weight.

Signal Sampling

When recording electronic signals, Shannon's or Nyquist sampling theorem states that the signal must be sampled at a frequency greater than twice as high as the highest frequency present in the signal itself. The reason why the signal must be sampled greater than twice the highest frequency is because if the signal is undersampled then the entire "picture" of the data is not attained and the recorded signal may be misleading. Sampling at twice the highest frequency allows the user to ensure that the entire scope of the data is being recorded with intermediary data points for improved signal analysis. This minimum sampling rate is called the *Nyquist sampling frequency* (f_n). In practice, most biomechanists usually sample 10x the highest frequency.

The signal can be expressed using Fourier series:

Equation 6

$$h(t) = a_0 + \sum [b_n \sin(2\pi f_n t) + c_n \cos(2\pi f_n t)]$$

The Fourier coefficients can be calculated using these formulas:

Equation 7

$$a_0 = \frac{1}{T}\int_0^T h(t)dt$$

Equation 8

$$b_n = \frac{2}{T}\int_0^T h(t)\sin{(2\pi f_n t)}dt$$

Equation 9

$$c_n = \frac{2}{T}\int_0^T h(t)\cos{(2\pi f_n t)}dt$$

The power spectral density (PSD) plot will be used to emphasize the frequencies that are most influential in creating the recorded waveform. The PSD shows which frequencies of the outputted signal are the strongest and weakest. From here it can be determined which frequency or frequencies contain the desired and undesired information. Now knowing this, signal conditioning can be performed on the output signal to highlight the desired frequency(ies) and degrade the undesired frequency(ies).

Signal Conditioning

The two methods of signal conditioning that were implemented for this research work were oversampling and a low pass filter. Oversampling in practice is implemented to achieve a cost efficient higher resolution analog to digital signals. This also can increase the signal-to-noise ratio, thus reducing some of the inherent noise in the signal. Oversampling can also assist when implementing any type of anti-aliasing filters. By assisting, it would increase the bandwidth of the sampled signal which would relax the constraints put forth by the filter itself. Relaxing these constraints would allow for the sampled signal to more easily be filtered because the available bandwidth would be much greater that the Nyquist limit. The amount of oversampling is defined as Equation 10.

Equation 10

$$\beta = \frac{f_s}{2B}$$

Where f_s is the sampling frequency, B is the highest frequency of the signal, and β is the oversampling factor. Figure 17 shows a comparison of an audio signal sampled at some frequency f_s (upper graph) and a frequency which is twice of that (lower graph).

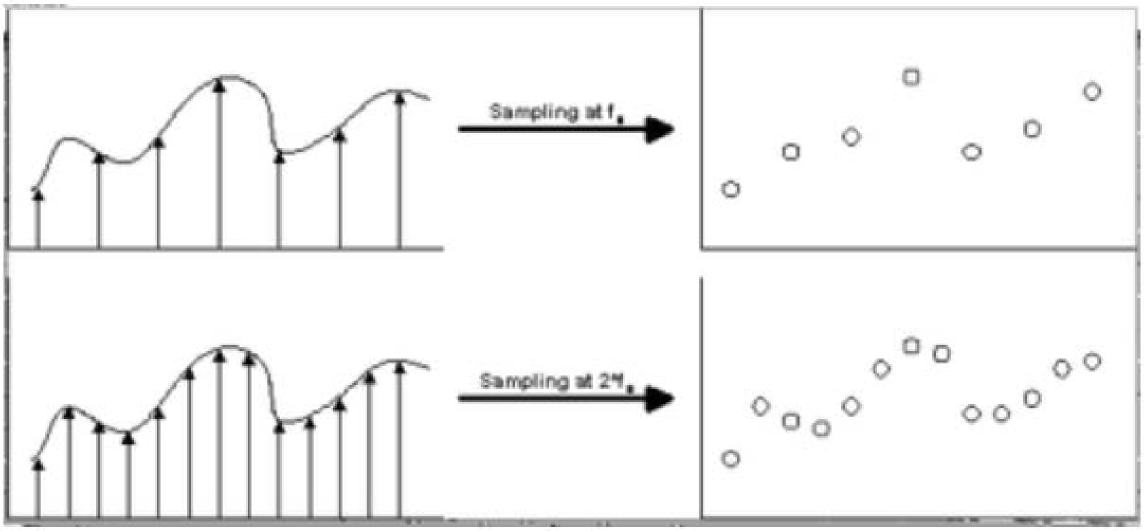

Figure 17: Top showing a situation where normal sampling occurs, bottom is the same signal oversampled.

Briefly, aliasing in signal processing is when "a signal is discretely sampled at a rate that is insufficient to capture the changes in the signal" (aliasing). Again, according to Nyquist sampling theorem, the sampling frequency should be at least double the highest frequency within the sampled signal. The issues that can arise are that if the signal is not properly sampled the resulting points may mislead the user into thinking that the signal has quite a different form than it actually does. This can be very dangerous when interpreting a signal that is unknown in nature.

In dealing with signals that have a broad spectral signal it is possible to get high order frequencies that “fold over” into the lower frequency spectrum and appear as false information that cannot be separated from the valid sampled data (anti-aliasing KH). This also is known as a form of aliasing. Therefore, in order to “eliminate” the higher order frequencies anti-aliasing filters can be implemented. For this experiment the type of filter that will be explored is a low-pass filter. A low-pass filter is a filter that can be hardware applied to the signal itself or software applied to the signal during post-processing. The filter itself allows low frequency signals to pass and attenuates signal frequencies higher than that of the chosen cutoff frequency. The type of low-pass filter that was implemented was a second order low-pass filter. This filter can be expressed as Equation 11, which is the general form of a low pass filter.

Equation 11

$$H(s) = \frac{\omega_n^2}{s^2 + 2\zeta\omega_n s + \omega_n^2}$$

Where ω_n is the undamped natural frequency and ζ is the damping ratio. Within MatLab the denominator of Equation 11 is the transfer function used for the filter. Once this transfer function is developed, it and ω_n^2 are placed within the *filter* command which defines the numerator and denominator of the designed filter. The value of ζ used for the constructed low-pass was unity, which yields all real poles.

In utilizing any anti-aliasing filter there are three things to take note. These are time response, phase distortion/time delay, and amplitude distortion. An ideal low-pass filter characteristic is shown in Figure 18 (Morisak 2012). The ideal characteristics develop a "brick wall" type filter where the cutoff frequency has an immediate drop off for any frequency above the cutoff. This type of response however cannot be achieved in a physical circuit.

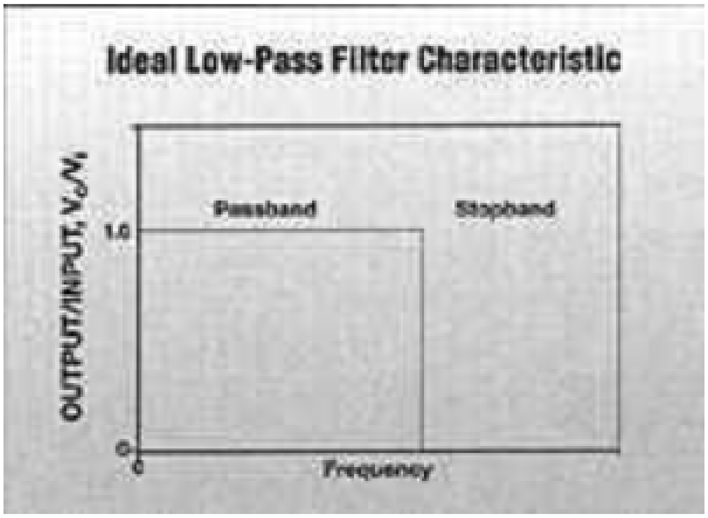

Figure 18: Ideal Low-pass filter characteristics

The actual response of a low-pass filter has a gradual sloped drop off after the cutoff frequency, this drop off can be adjusted based on the number of poles used for the filter. The response is shown in Figure 19.

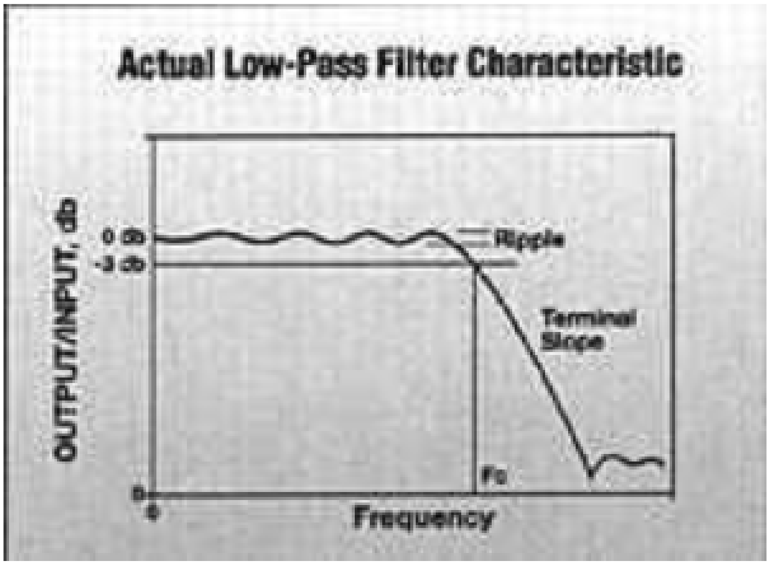

Figure 19: Actual Low-Pass Filter Characteristics

The actual filter works by attenuating any frequency higher than the cutoff frequency. Therefore, the higher the frequency is from the cutoff, the larger the degradation will become for that frequency as shown in Figure 19. This form of chart is known as a bode plot. As shown in Figure 20, a bode plot displays the time response, phase distortion and the amplitude distortion. The top plot shows what was shown previously in Figure 20 with the amplitude distortion/degradation. The bottom plot shows how the signals phase will be affected for the corresponding cutoff frequency chosen in the above amplitude plot. Phase distortion can be a problem when comparing multiple sensors with different cutoff frequencies because the higher frequency signals will occur later than the low frequency signals. The amplitude distortion would in turn minimally affect the desired signal output, yet this result is known by definition of a filter. The time response or shallowness of the roll-off after the cutoff frequency can be increased by increasing the order of the filter. In theory an infinitely high order filter would be the "brick wall" filter. However, an extremely high order filter can produce undesirable effects to the signal. With these characteristics known, a desirable low-pass filter would be one with the strongest effect to the higher frequencies, but one that would also distort the desired low frequency signal the least.

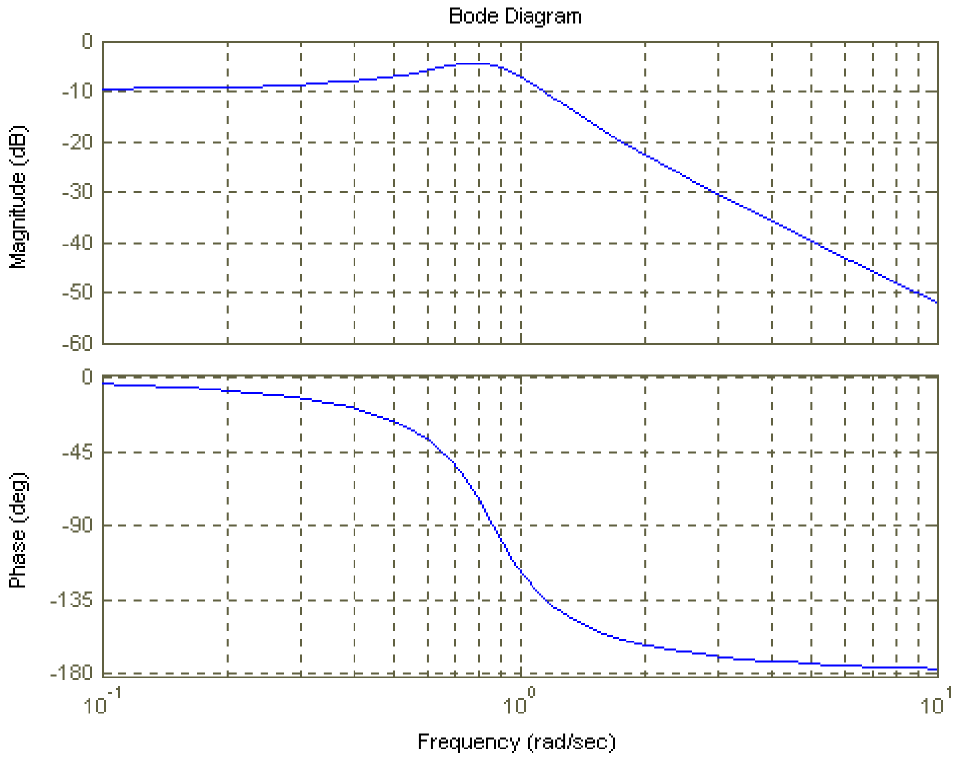

Figure 20: Example Bode Diagram

.

As mentioned earlier, in utilizing oversampling and a low-pass filter one can achieve a "higher" resolution signal and be able to filter the signal of high frequencies more easily. The increased sample rate allows for the filter to have a higher cutoff frequency, while still eliminating aliasing. With the combined signal conditioning, the filter roll off slope can be shallower i.e. more poles, the filter would not attenuate the lower frequency of interest and the phase distortion of the cutoff frequency can be pushed higher. This would not affect the low frequency of interest as much (Stilson 1996).

IV. Experimentation

Design, construction, implementation, and processing of the dynamic load experiment are detailed in the following chapter. The dynamic load experiment dynamically applied a vertical and longitudinal compressive force through the thorax at the natural flapping frequency and natural thoracic displacement. In compressing the thorax, this forced the indirect flapping mechanism within to actuate and flap the wings to full elevation and de-elevation. This experiment is a build off and improvement over previous work performed by Alex Hollenbeck, apart from the work performed at AFIT, this technique of mechanically actuating the thorax is a unique technique.

Experimenting with Living Organisms

The key factors in this research are the physiological and behavioral responses of *M.sexta*. As with all living creatures, the only way to provide proper handling and care is to understand the life cycle and the developmental process that occurs naturally. All living specimens used in this thesis were handled with the utmost care and with as much respect as possible, but due to the nature of the experiments, some degree of physical damage was necessary for scientific knowledge. Other than the documented experiments, the subjects were at no time mishandled or abused.

Initial Design

The initial design of the experiment was based on modifying an existing experimental set-up provided by Hollenbeck. Hollenbeck's experimental apparatus exhibited the ability to compress the thorax in the vertical direction and record the forces within to develop a power output value for the upstroke only or DVMs. In order to reproduce the full flapping motion the thorax needs to be actuated in the vertical and longitudinal directions to reproduce the forces produced by the DVMs and DLMs. From here it was decided that there were two potential modifications that would evolve the existing apparatus to also longitudinally compress the thorax. The first possibility was to create a duplicate of the mechanism for the vertical compression in the longitudinal direction. The second possibility was to devise and construct a linkage mechanism that would longitudinally and vertically compress the thorax with the single existing actuator. Based off of materials available, ease of fabrication, and functionability the second modification was chosen to explore, design, and construct.

The steps taken for the design process of the mechanical linkage and eventual adaptation to the current test bed were to select a kinematic linkage design, understand the kinematics involved, design the appropriate linkage to achieve the displacements desired, and adapt the designed linkage to the existing system such that complete flapping is achieved. For completeness, the current systems operation will be described such that a basis can be understood for which the linkage will be designed to adapt to. The original existing vertical dynamic flapper utilized a shaker device to oscillate the specimen vertically into a “push rod” which was constructed by a rapid prototyping machine at AFIT. The shaker was found to be one of the design drivers in the design of the linkage system producing a +- 3 mm stroke. The next design driver was the single point of actuation i.e. a single point of actuation would be permitted for the linkage system. The last design driver was a mechanism that could produce a longitudinal motion/force with a vertical actuation. From here, the simplest single degree of freedom linkage systems was evaluated in order to determine the most optimal system to continue forward with. The simplest mechanism is the four-bar-linkage or variations of. The notion of simplicity and the fewest pivot joints was also taken into account for fabrication and implementation purposes. The linkage system chosen was a slider-crank mechanism. The reasoning for this selection was that the mechanism is very well understood, easy to implement, simple, and fit all of design criterion set forth by the actuator and desired system movements.

Evaluation of the Slider-Crank Mechanism

The slider-crank mechanism operates under simple geometric relationships. Knowing the slider and crank length, and the crank angle, all of the positional quantities of the system can be solved for. Typically, a slider-crank mechanism involves a single actuator connected to the crank which drives the slider. This mechanism is commonly seen in car engines and is implemented in the form of a crankshaft. A slider-crank mechanism consists of three rotational joints and one slider, where the first joint is fixed and only free to rotate, the second is free to rotate and displace in two dimensions, and the last is free to rotate and displace in only 1 dimension. Through kinematic and geometric evaluation of the mechanism, it was determined that the second pivot joint could be used to transmit the longitudinal force necessary to actuate the downstroke of the moth. At small crank angles, less than 20 degrees, the pivot displaces mainly in the longitudinal direction. This is shown in Figure 21 and Figure 22. The difference between Figure 21 and Figure 22 is that Figure 21 is shown to accentuate the difference between the vertical and horizontal displacements. The vertical displacement is shown to be small, the average slope being ¼, compared to that of the horizontal displacement. The pivot travel shown in the figures corresponds to a shaker total travel of 1.08 mm and an angular rotation of 20 deg to 5 deg. The specific scenario shown in the figures is the one that was documented to have taken place for the actual longitudinal displacement during the experiment.

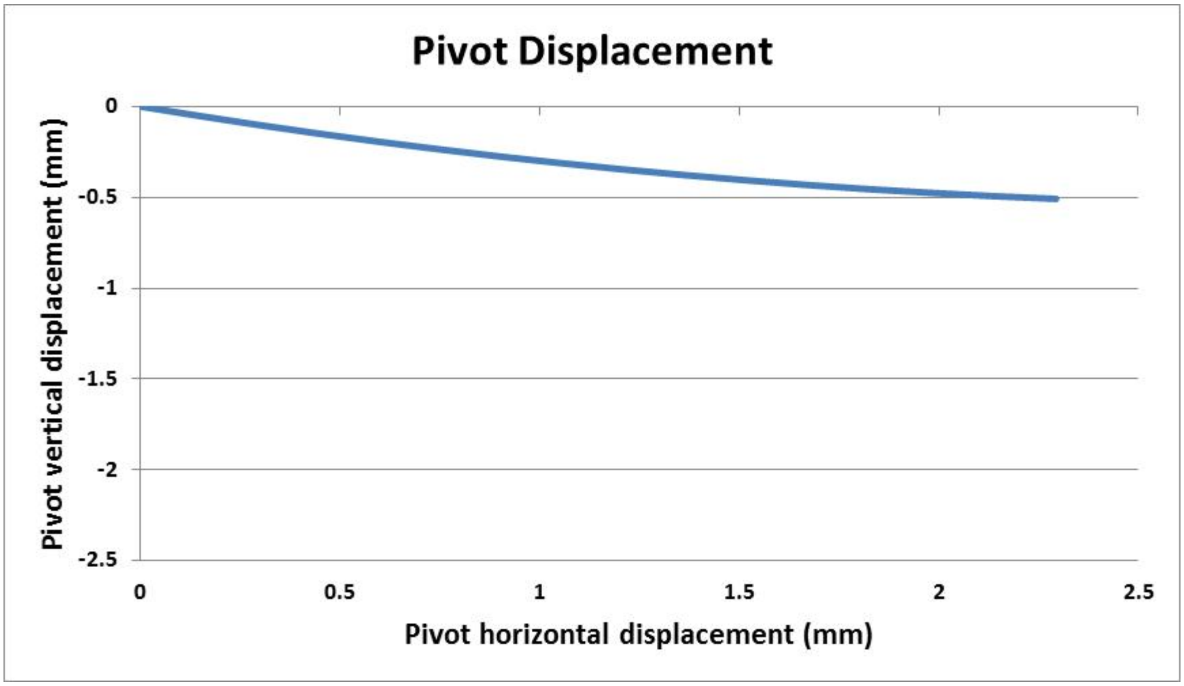

Figure 21: Pivot Displacement in the vertical and longitudinal direction (equal axis)

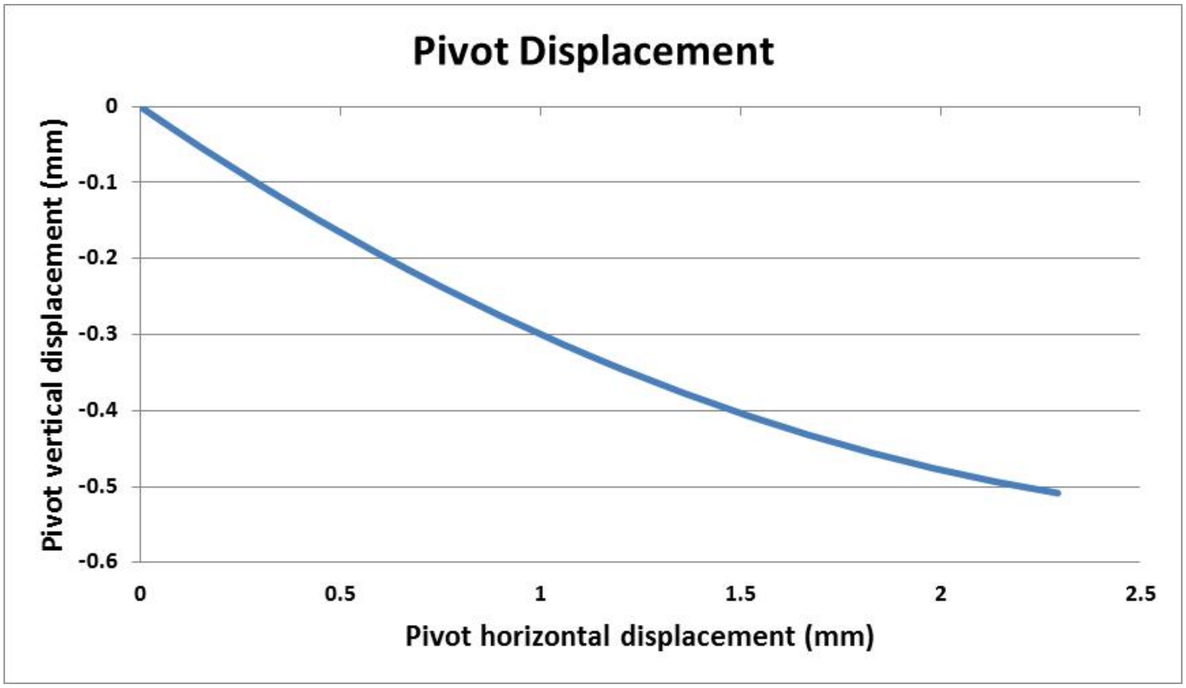

Figure 22: Pivot Displacement in the vertical and longitudinal direction

Knowing that for small angles the horizontal displacement is approximately four times larger than the vertical displacement, the designed linkage system proved to sufficient for the proposed experiment. Apart from the pivot displacements, the other factor that needed to be satisfied for the system was the shaker displacement. The presented design produced a 1.08 mm displacement, which is well within the operational range of the shaker from zero-center. Other additional factors that constrained the linkage design were spatial considerations, such as pivot location constraints and lengths necessary to actuate the moth's rear phragma in the proper position. After several iterations, the linkage that produced the above pivot displacements was chosen to construct for the proposed experiment. The specifications of the linkage are shown in Table 2. The constructed linkage represented in SolidWorks is shown individually and connected to the system in Figure 23.

Table 2: Linkage Specifications

Linkage Specifications		
Crank length	9	mm
Slider length	8	mm

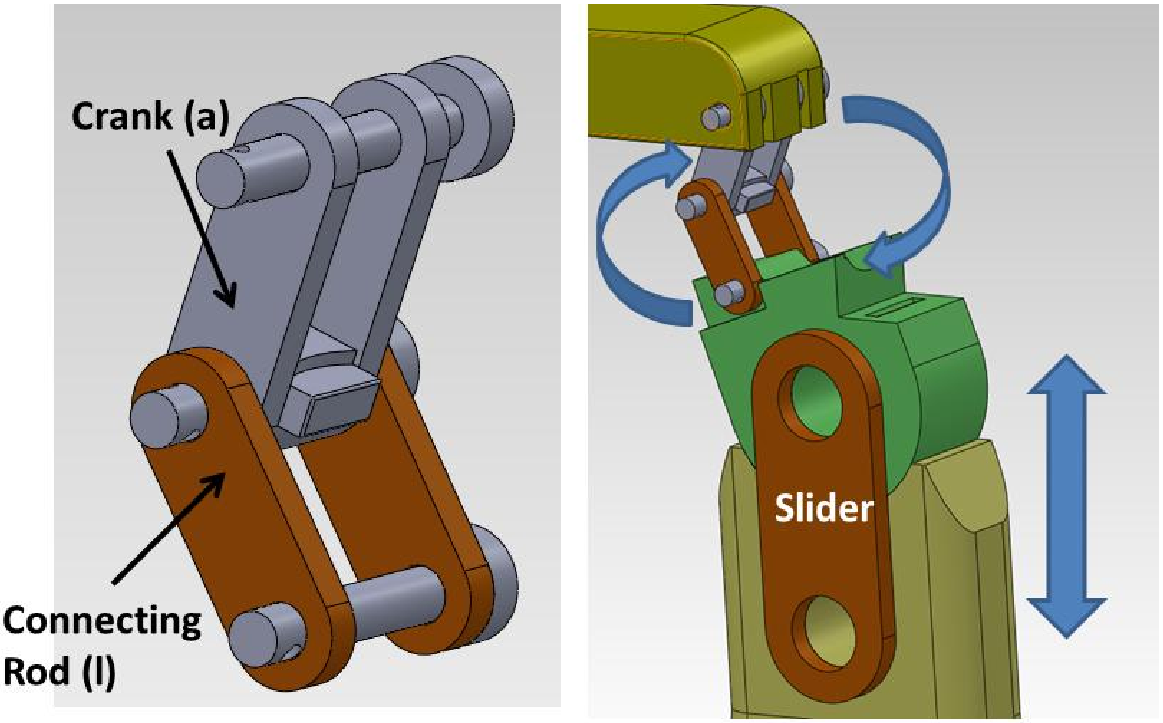

Figure 23: Slider-crank assembly as shown in SolidWorks

Dynamic Load Mechanism: Design and Construction

The mechanism’s design was a modification to the apparatus that Hollenbeck had created for his vertical compression testing. The mechanics were a shaker fixed to the ground plane, a saddle for the moth to be mounted to, and a push rod fixed to the ceiling plane with a load cell in-between. The specimen was oscillated vertically into the push rod at approximately 25 Hz to obtain a 55 deg upstroke. This system characterized the specific power density of the dorsoventral muscles. The original apparatus is shown in Figure 24. From here it was necessary to determine the modifications necessary to evolve the existing system to one that reproduces the full flapping motion. The constructed new design was able to flap the wings at 28 Hz with amplitude of +- 55 deg to achieve a complete natural flapping stoke as well as force data for the respective compression directions.

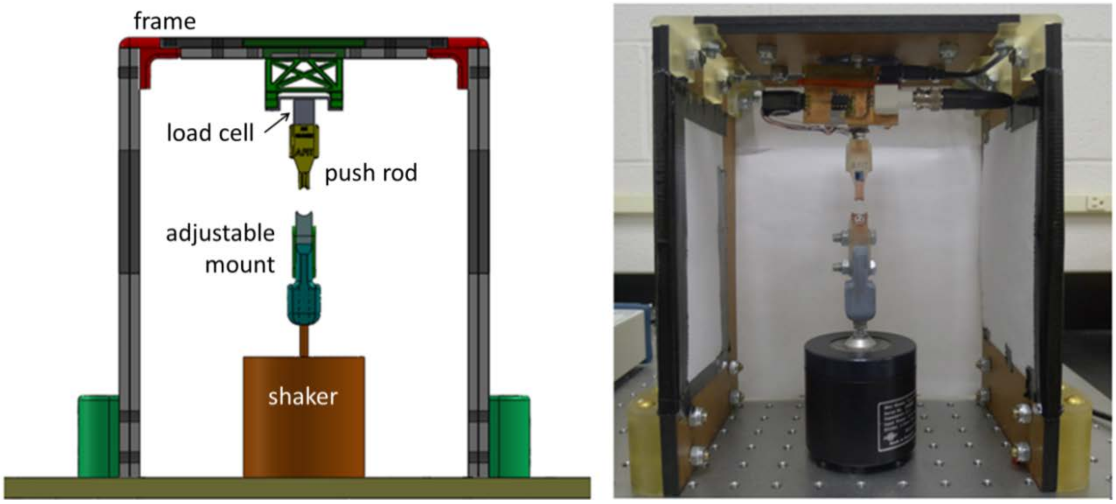

Figure 24: Upstroke only configuration of the dynamic load experiment as built by Hollenbeck

When considering imposing a force that would actuate the dorsolongitudinal muscles, one needs to identify the attachment points of the muscles to impose the force. Quite differently than the ventral muscles, the longitudinal group lies between the head and the thorax. Therefore, in order to access the attachment points of the longitudinal muscles, the head and the thorax needed to be removed. Removing these exposes the front and rear phragma, the attachment points of the muscle group. This exposure being necessary for actuation drove the design of the modified dynamic load platform.

The new design followed many of the existing features of the apparatus. After much iteration, two versions of the full flapper were devised. The version that will be documented here is the isolated component design. This design allowed for the forces to be more accurately analyzed and examined. The new design featured several new components which were: a saddle mount, linkage mechanism, linkage mount extension, and longitudinal push rod with assembly. The new set-up was modeled in a 3-D modeling program, SolidWorks, to attempt to work out design flaws and interferences within the system. The new design is shown in Figure 25. The new design rotated the moth 90 deg to the right looking into the rig to allow for the longitudinal push rod to be mounted to the load cell and load cell mount. This rotation was necessary to allow for an open space for the high speed camera to capture the shaker displacement and wing flapping.

The new construction evolved the original design, making it capable to perform both the upstroke and downstroke, while recording force measurements for both simultaneously. This system can fully replicate the full wing stroke of the hawkmoth as it flies in nature. The major additions include a linkage mount, linkage system, specimen mount, longitudinal push rod and force balance. Minor frame adjustments were also made to accommodate for the added side forces.

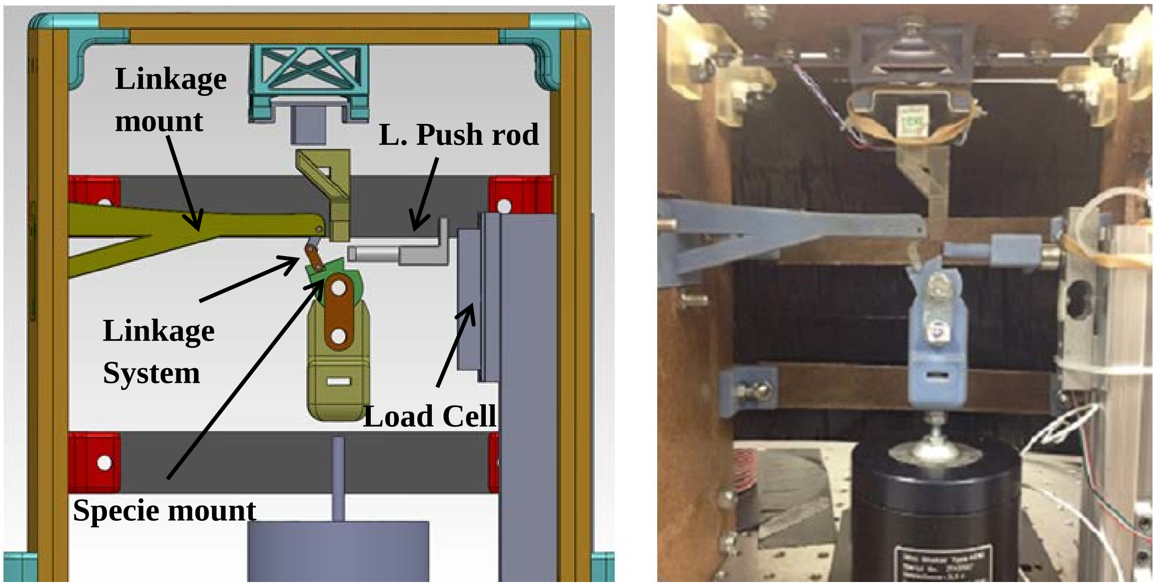

Figure 25: New build-up of the dynamic load experiment, accounting for vertical and longitudinal compression

The smaller more articulate pieces were printed using an Objet Eden500V™ 3-dimensional printer. The mechanical properties of the printing material are detailed in Appendix G. Instrumentation and Equipment Used. The material of the printed parts most closely resembles common ABS plastics. The larger flat pieces for the frame construction were made out of wood.

For the experiment, the specimen was moved vertically upward into the vertical push rod to produce the upstroke of the moth. At the same time the linkage pivot moves away from the rear of the specimen. As the mount moves downward, the pressure from the vertical rod is released and the linkage pivot swings forward into the rear phragma producing a longitudinal compression of the thorax yielding the downstroke of the wings. This process occurs 28 times a second (Hz). The mount is driven by a Brüel & Kjaer Mini Shaker Type 4810. As mentioned in the theory section, the push rods are both considered to be sufficiently rigid to produce an “infinite” stiffness thus requiring no adjustments for potential rod deformation.

Instrumentation and Data Acquisition

This section will detail all of the instrumentation utilized in order to achieve the desired specific power output results. The instrumentation is as follows, two 3 kg strain gauge cantilever beam load cells, a high speed camera, a laptop, and a data acquisition device (DAQ). The DAQ board used was a National Instruments USB-6251 BNC Data Acquisition device, the specifications of this device is located in Appendix G. Instrumentation and Equipment Used. The load cells were both powered through external power sources and their signals were sent through a designed and constructed amplifier board to yield a 0-5 Vdc signal to the DAQ. Before utilization of the load cells in the experiment, they required to be calibrated. The calibration process that was used involved taking a series of known weight values and placing them on the load cell and recording the signal voltage to the DAQ. The signal was observed utilizing the National Instruments *Measurements and Automation* software. The calibration curves for both are shown below in Figure 26 and Figure 27. The calibration yielded a linear relationship of mass to volts which was converted to force in Newtons for analysis of the power density.

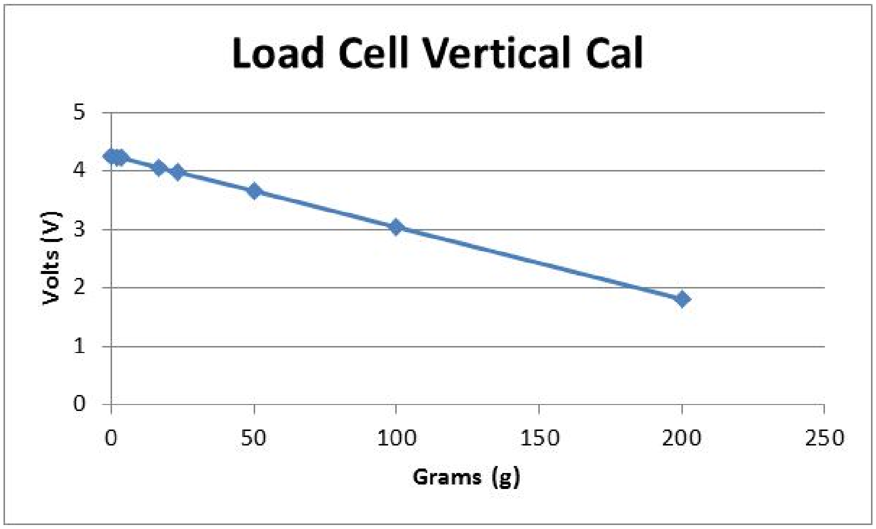

Figure 26: Calibration curve for the vertical load cell

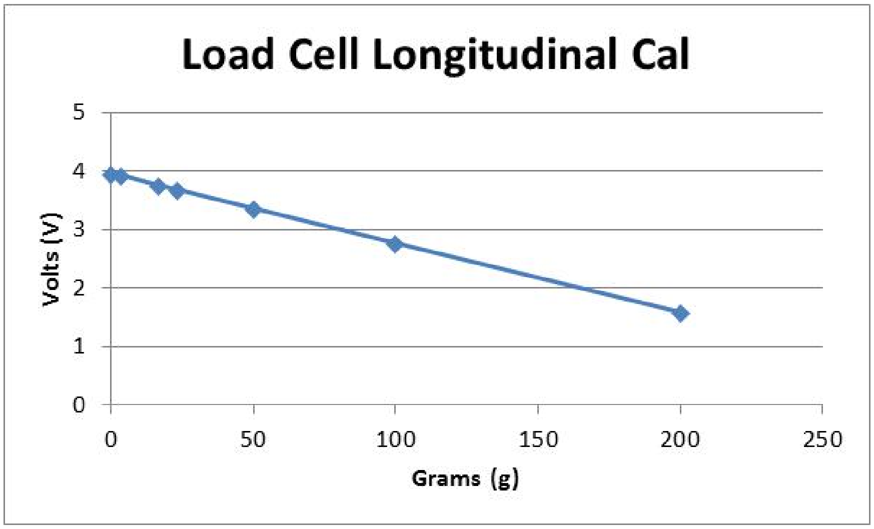

Figure 27: Calibration curve for the longitudinal load cell

The high speed camera that was used was a Dantec Dynamics NanoSense MkII high-speed video camera with a Nikon AF Nikkor 28 mm lens. The camera was triggered to begin to start recording at a specified frequency when the oscillatory signal sent to the shaker was executed. This ensured that each camera frame corresponded to a force signal from the load cell. Both the camera and load cells were set to record at 2500 Hz. This equal image to force data allowed for simpler processing and analysis. The software used to operate the camera was Motion Studio x64. The control hub for the signal retention and analysis was a laptop loaded with Windows 7, National Instruments drivers (specifically NI-DAQmx), MatLab R2011a x32, and Motion Studio x64. All of these pieces of software and their respective versions were necessary for the data acquisition portion of the experiment. A note of importance is that the 32 bit version of MatLab was necessary to communicate with the NI-DAQ drivers and components. A schematic of the communications connections of all of the above components is shown in Figure 28.

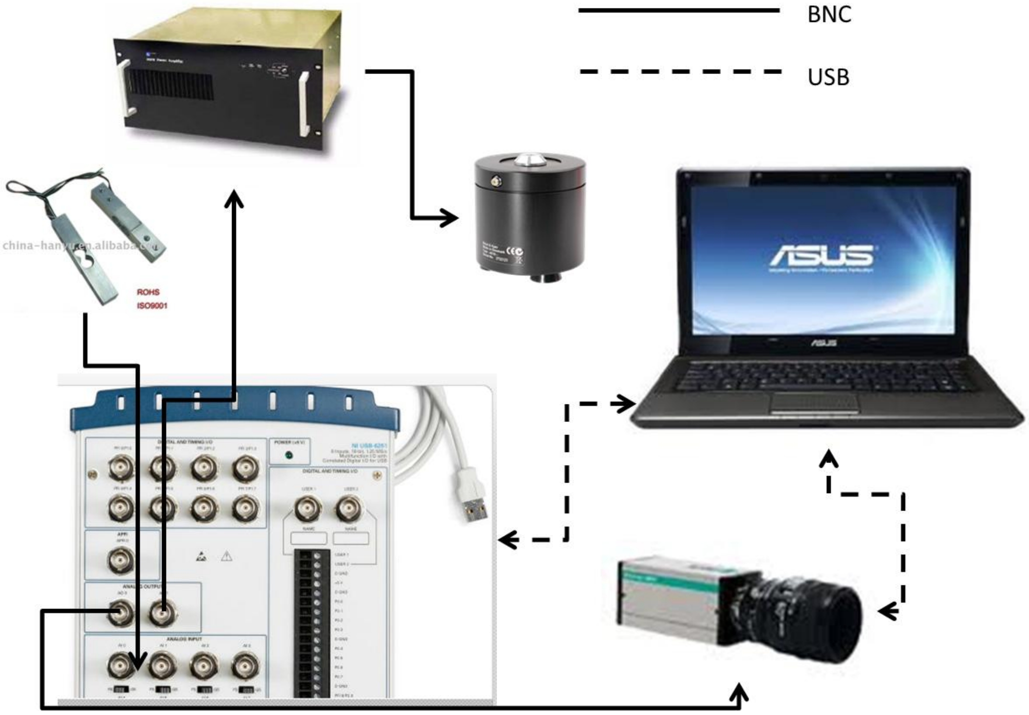

Figure 28: Wiring communications schematic of the experimental set-up

An image of the actual experimental set-up is shown in Figure 29. The communication chain between all of the components is as follows: The PC utilizing MatLab written code sends an input signal via USB to the NI-DAQ, the NI-DAQ sends two output signals, one to the camera and the other to the shaker amplifier, through the amplifier the shaker gets a sinusoidal forcing signal which drives the shaker and at the same time the camera is capturing images. After one second, 2500 data points are collected from the camera and each of the load cells and is sent back to the computers Matlab code for storage and analysis.

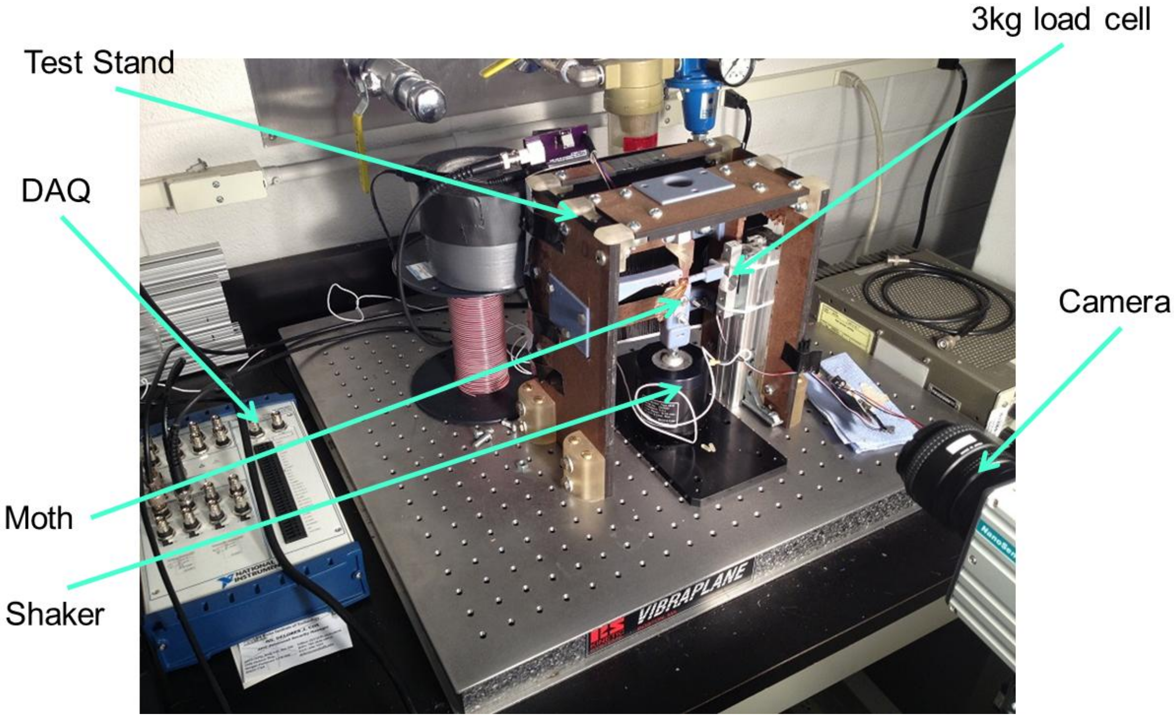

Figure 29: Experimental setup

Optimization of the System Design

Initially when the new experiment was devised, the main goal was to create a mechanism that could compress the thorax in such a manner that the full wing stroke would be reproduced. This was achieved by designing a single component with all of the functionality of the linkage mount and longitudinal and vertical push rod. This part as shown in Figure 30 was able to envelop all of the functionality of the three parts mentioned above and did yield a mechanism that reproduced the full flapping stroke. Connections to the two load cells were formed at the top and right side with the linkage assembly being pinned through the slot of the left. Some minimal force data analysis was performed to ensure the workings of the load cells. However, this data was unusable due to interferences from all of the connection points on the single part. For this reason the multi-part design was thought to remove all of the interactions during actuation. This single piece design provided great insight for the final design of the dynamic load mechanism. In seeing the large load interactions from the single part it became apparent that a multi-part system was necessary to obtain the desired load data for each direction. The multi-part system that was designed and built encompassed all of the functionality of the single part system, yet allowed for recording uncompromised signals from the load cells.

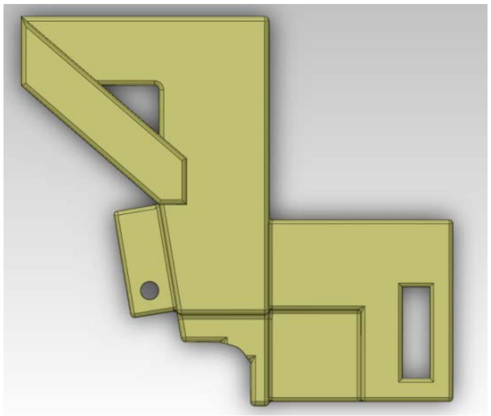

Figure 30: Initial design all-in-one test piece

Signal Communication Code

This section will detail the MatLab code that was written to communicate with the NI-DAQ for data acquisition. The segment of the code that will be discussed is the inputs to the system as well as the signal generation for the shaker. The entire signal code is presented in appendices B-F.

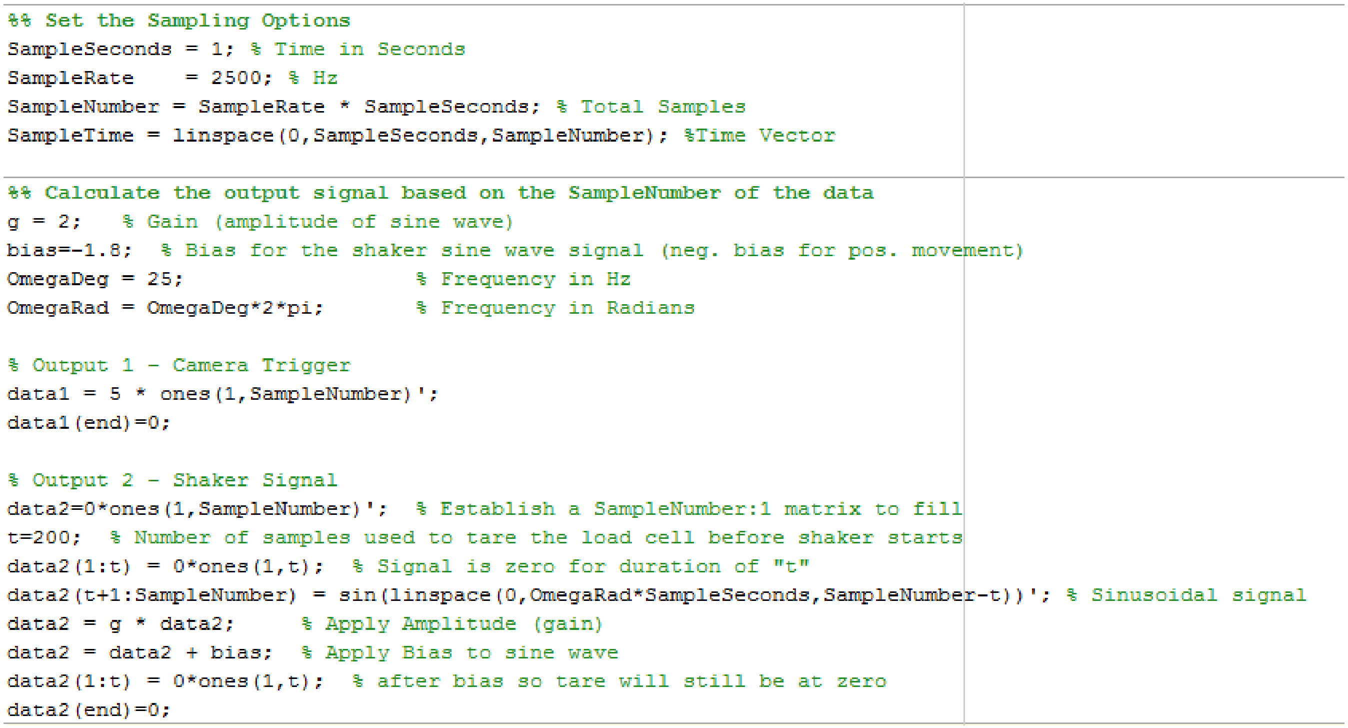

```
%% Set the Sampling Options
SampleSeconds = 1; % Time in Seconds
SampleRate    = 2500; % Hz
SampleNumber = SampleRate * SampleSeconds; % Total Samples
SampleTime = linspace(0,SampleSeconds,SampleNumber); %Time Vector

%% Calculate the output signal based on the SampleNumber of the data
g = 2;    % Gain (amplitude of sine wave)
bias=-1.8;  % Bias for the shaker sine wave signal (neg. bias for pos. movement)
OmegaDeg = 25;                    % Frequency in Hz
OmegaRad = OmegaDeg*2*pi;         % Frequency in Radians

% Output 1 - Camera Trigger
data1 = 5 * ones(1,SampleNumber)';
data1(end)=0;

% Output 2 - Shaker Signal
data2=0*ones(1,SampleNumber)';  % Establish a SampleNumber:1 matrix to fill
t=200;  % Number of samples used to tare the load cell before shaker starts
data2(1:t) = 0*ones(1,t);  % Signal is zero for duration of "t"
data2(t+1:SampleNumber) = sin(linspace(0,OmegaRad*SampleSeconds,SampleNumber-t))'; % Sinusoidal signal
data2 = g * data2;     % Apply Amplitude (gain)
data2 = data2 + bias;  % Apply Bias to sine wave
data2(1:t) = 0*ones(1,t);  % after bias so tare will still be at zero
data2(end)=0;
```

Figure 31: Signal Acquisition Code

The initial segment of the code mainly contains variable inputs. These consist of variables such as SampleSeconds, defines the total number of seconds to collect data, SampleRate, and sample frequency. The next section in the code defines the sin wave shape sent to the shaker. The value g is the gain (amplitude) of the sin wave and the bias is an adjustment to the signal, i.e. a negative bias drives the shaker more upward then downward for the oscillation. The last section of the code composes the sin wave to be sent to the shaker and the trigger to the camera. The sin wave is generated by creating an array that is filled with the total number of samples in the run, *SampleNumber*, with an initial tare period, *t*, and the sin wave that was defined by the frequency of flapping, length of test and tare, gain, and bias. The camera output, *data1*, is an array filled with fives then length of the total sample numbers in the run. This sends a voltage signal to the trigger of the camera, which tells the camera to begin to record images for as long as a trigger signal is being received. From here the code executes input output communications with the NI-DAQ to transmit the created signal and obtain the force data from the load cells. The force data is then converted using the calibration equations developed and plotted versus time to display the signals produced by the load cells.

Specimen Preparation

This section will detail how the specimen was prepared for the experiment and data collection. For the vertical compression test, the specimen was left mostly in its natural state apart from the euthanization and the legs being removed. This was possible because the area of required compression was on the top and bottom of the moth's thorax which is readily exposed. As mentioned earlier, in order to expose the attachment points of the longitudinal muscles the head and thorax would need to be removed to mechanically actuate the front and rear phragma. The specimen preparation and procedure was as follows:

1) Upon successful molting, the moth was removed from its habitat as shown in Figure 64 and transferred to a mesh cage that received light at all times, which inhibited the moths from flying.
2) While in the mesh cage, the moths were not fed any sort of diet, therefore their life span was fairly short (3-5 days). This meant that if the experiment was not ready for testing, the moths would be placed in a re-sealable plastic bag with a paper towel slightly moistened and placed into the freezer. This dampening of the cloth was noted to preserve the moth's integrity when thawed. However, all of the moths used for the results were fresh and not frozen.

3) When a moth was to be tested it was asphyxiated in a re-sealable plastic bag with a cloth dampened with acetone.
4) The moth was then weighed on a digital scale
5) Prior to testing is when the moths head, abdomen, and legs were delicately removed.
6) At this point the moth was now ready for testing and placed into the test fixture.

Experimental Procedure

This section will discuss the first process of the experiment, being the moth setup and live data acquisition. The moth, as prepared, was placed head towards the longitudinal push rod on the mount. A thin coating of dissection wax was placed between the moth and mount to reduce any slipping that might occur. At this point the shaker mount assembly is disconnected from the linkage assembly to allow for ease of aligning the specimen on the mount. From here the mount is slid into place and the linkage assembly is pinned to the mount. Being that the mount and linkage system were point designed, the mount needed to be in a single specific point vertically and horizontally for the linkage to work as designed. This being true, if any height adjustment was necessary to gain the desired spacing between the moth and the vertical push rod, the rod assembly was removed and the push rod was shimmed up or down with thin washers to accommodate for the spacing. The same technique was performed on the longitudinal push rod if adjustments were necessary. The moth as placed in the system is shown in Figure 32.

Figure 32: Close-up view of the test apparatus with the specimen in place

After numerous test runs, varying the amount of vertical and longitudinal pre-load compression, that is placing the rod in such a position that it would initially be compressing the specimen in either or both directions, the arrangement that yielded the most life like flapping was when both rods were in contact with the specimen with little to no deformation observed. Contact with the push rod prior to the test would cause a force being measured by the load cell, for this effect the load cell as mentioned earlier has a tare period to zero out the force of the pre-load. An LED spotlight was used to illuminate the area of the moth for the camera to have sufficient light for image capturing. The higher the frame rate of the camera, the lower the exposure time of each image, therefore a large amount of direct light was needed to provide the light source for each image. The camera was aligned, using a tripod, perpendicular to the longitudinal axis of the moth and roughly centered about the moth. Once everything was in place the camera was set to receive a trigger signal and the signal communication code was executed through MatLab which began the test. Through significant data analysis while the wings were on, it was shown that the wings have an interference with the force being applied through the thorax which had an effect on the force data that the load cell was receiving and therefore skewed the data for the power calculation. The effect is thought to be inertially and aerodynamically related due to the forces on the wings generated through the flapping motion. The wings added a “dampening” effect to the force signal being sensed by the load cell. This dampening effect is shown in Figure 33 and Figure 34. Figure 33 is of the vertical load cell with the image on the right being with wings and the image of the left being without wings. Figure 34 displays the same information, just in the longitudinal direction. The boxed ranges in the figures denote the force signature when contact and compression were made. The wings-on effect is shown to be a “dampening” effect because one would assume that the wings act as another source of resistance to the system, therefore the forces with the wings should be greater than those without the wings, this is not the case for the data collected. The forces sensed by the load cell are less with the wings-on case then they are with the wings-off case. This is thought to occur because when the moth is being compressed the wings are below the body and resistive forces on the wings reduce the force seen by the load cell until the wings pitch upward. For both test cases, with and without wings in both directions, the with-wings case did impose a “dampening” effect on the force to the load cell, which skews the end desired result of specific power density output. Through further analysis, the overall goal is to be able to characterize the thorax deformation that the muscles provide to indirectly flap the wings. After many test runs, one test with wings-on yielded the results of the off wings case. This was possible because of a “sweet spot” position that the moth was placed in that yielded a case where the wings did not affect the signal to the load cell. Attempts were made to replicate this scenario with many moths and none yielded the results of the one in the “sweet spot”. It was found through more testing, that removal of the wings did not have a significant effect on the forces required to deform the thorax and actuate the wing hinge motion. Removal of the wings purely exposes the forces necessary to mechanically compress the thorax and therefore the work that the muscles would have to provide to compress the thorax.

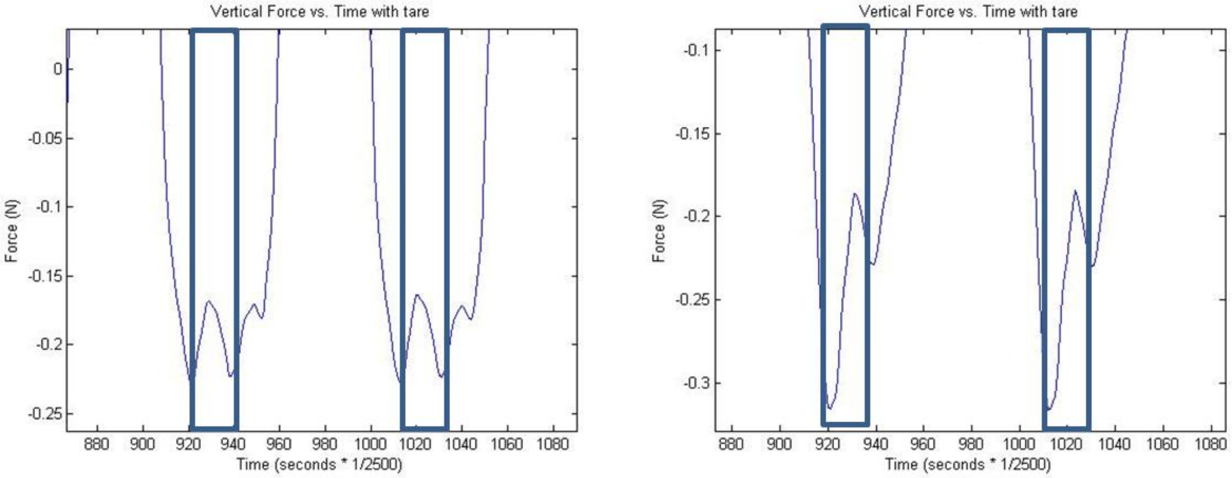

Figure 33: Left is the load cell data for the with wings case. Right is the load cell data for the no-wings case. (Force output for the upstroke) Blue box represents the area where the force was applied.

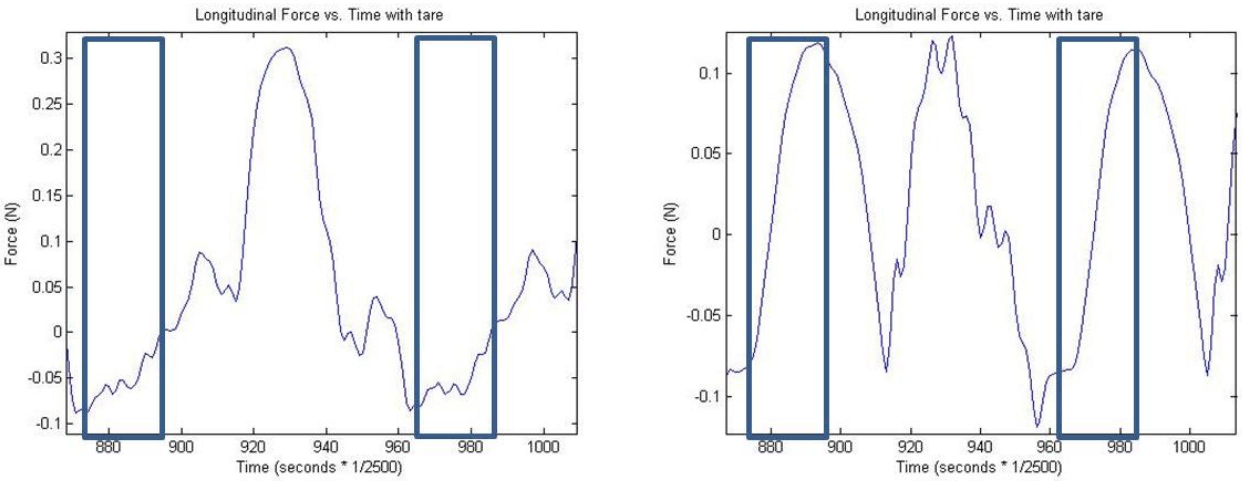

Figure 34: Left is the load cell data for the with wings case. Right is the load cell data for the no-wings case. (Force output for the downstroke) Blue box represents the area where the force was applied.

In order to ensure that the wings still reached the full range of motion, the moth was tested with wings on and the video recorded by the camera was observed ensuring full wing displacement occurred. When satisfactory wing angles were achieved, the moth was left in the test rig in the exact position and the wings were removed using a pair of scissors.

The filtering of the load cell data was performed after the data was collected. The post processing process was to first run a Fast Fourier Transform on both load cell data arrays and determine the highest primary frequency of the signals. An FFT of the vertical and longitudinal load cell data are shown in Figure 35.

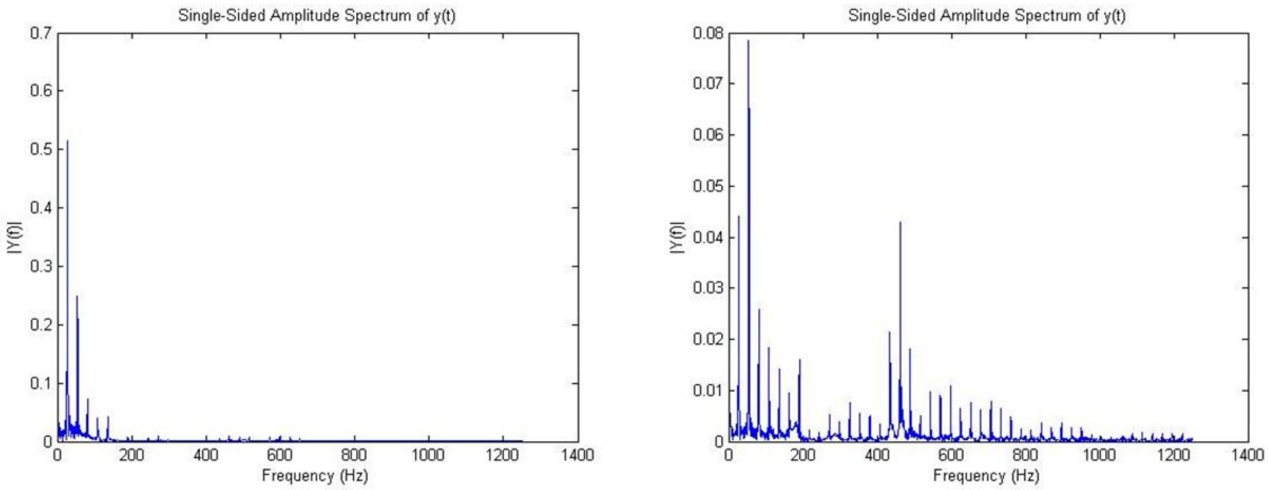

Figure 35: Left is the frequency response of the upstroke data, Right is the frequency response of the downstroke data.

The dominate frequency for both of the load cell responses was approximately 28Hz. This was determined by analyzing the FFT signals for the largest amplitude signal. This value was expected since the moth was flapped at that approximate frequency. The other peaks in the signal are harmonics of the 28 Hz signal. With the verification from the FFT that the signal of interest lays at or below 28 Hz the 2nd order low pass filter was set at a frequency of 30 Hz. The bode plot for the filter applied to the force and displacement signals is shown in Figure 36 and a part of the code used to implement the filter is shown in Figure 37.

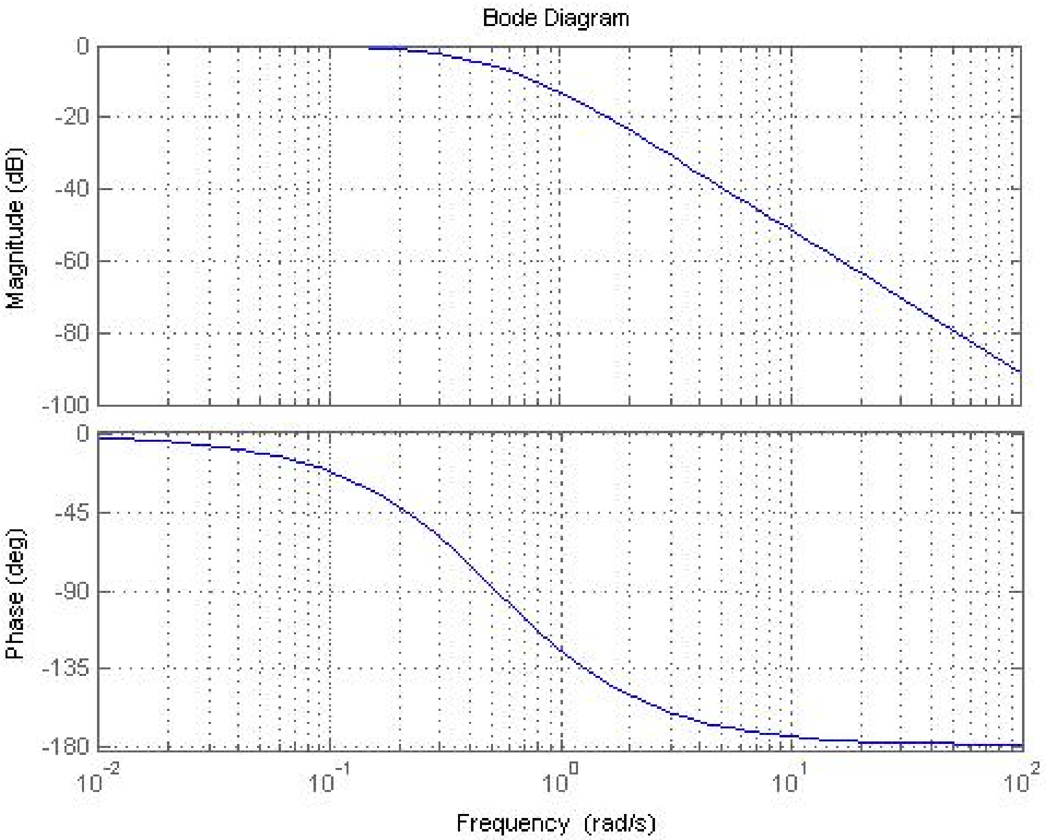

Figure 36: Bode diagram of the 2nd order low-pass filter implemented

The first segment of the filter code established the number of poles and the frequency of the low pass filter. The *tf* function in MatLab creates a continuous-time transfer function in the form of Equation 11’s denominator. Next, the code converts the transfer function from a continuous-time dynamic system to a discrete time system. Finally, the MatLab command *filter*, which is a one dimensional digital filter described by the numerator and the denominator of the discrete transfer function created. The filter is then applied to the signals for further data processing. Figure 38 shows an example of the filtered data versus unfiltered data.

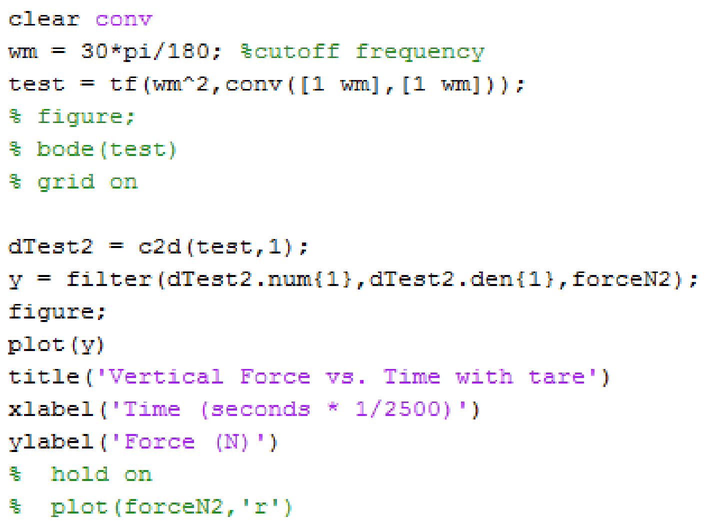

```
clear conv
wm = 30*pi/180; %cutoff frequency
test = tf(wm^2,conv([1 wm],[1 wm]));
% figure;
% bode(test)
% grid on

dTest2 = c2d(test,1);
y = filter(dTest2.num{1},dTest2.den{1},forceN2);
figure;
plot(y)
title('Vertical Force vs. Time with tare')
xlabel('Time (seconds * 1/2500)')
ylabel('Force (N)')
%  hold on
%  plot(forceN2,'r')
```

Figure 37: Matlab code constructing the low-pass filter

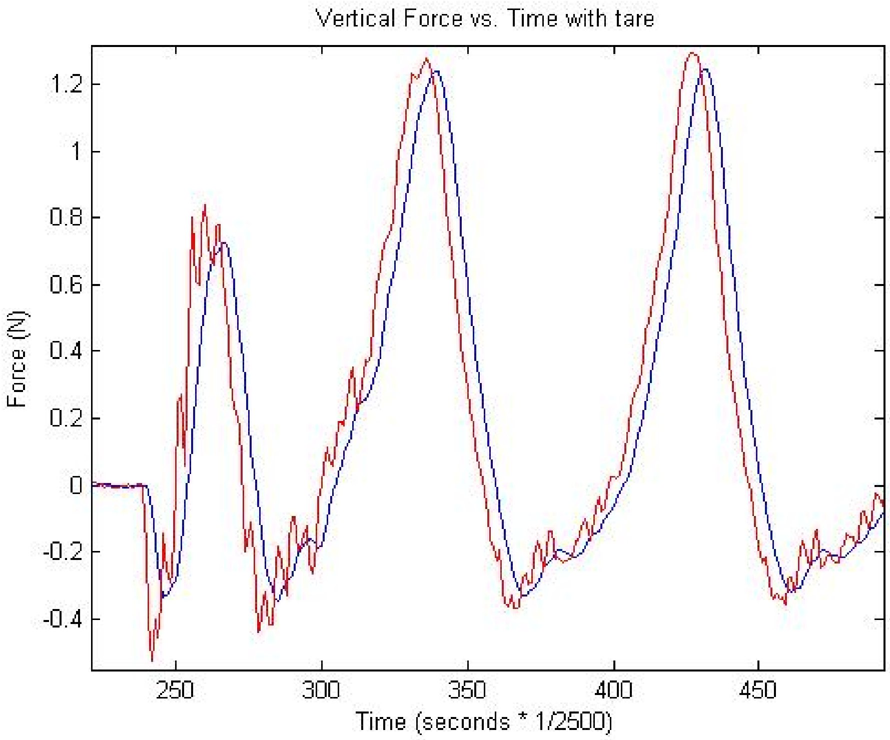

Figure 38: Unfiltered response (red), Filtered response (blue)

Wing stroke angle approximation

In order to ensure that the wings stroke amplitude was that expressed in natural flight, a method was needed to measure the wing angles achieved during testing. Live wing tracking was not an option available due to the resources available. The most important values as far as the wing stroke angles are concerned were the peak values associated with the upstroke and downstroke. Therefore, a method for approximating these two wing angle values was determined utilizing the camera images acquired during testing. For the wings, no-wings scenarios the method remained the same. A point near the root of the chord was chosen for the on-wings case, and for the no-wings case the chord length of the remaining wing stub was used. The wings originating position was determined by inspection of the first 200 images during the tare period. Because the camera was positioned orthogonally to the wing stroke angle plane the methodology is quite simple to determine the wing angle at any image frame. In order to approximate the wing angles a simple trigonometric relationship was formed. Figure 39 displays the triangle relationships in order to approximate the peak wing amplitudes. Since the images were acquired perpendicular to the specimen, the vertical distance tracked position traveled is the y value and the r value is the chord length measured.

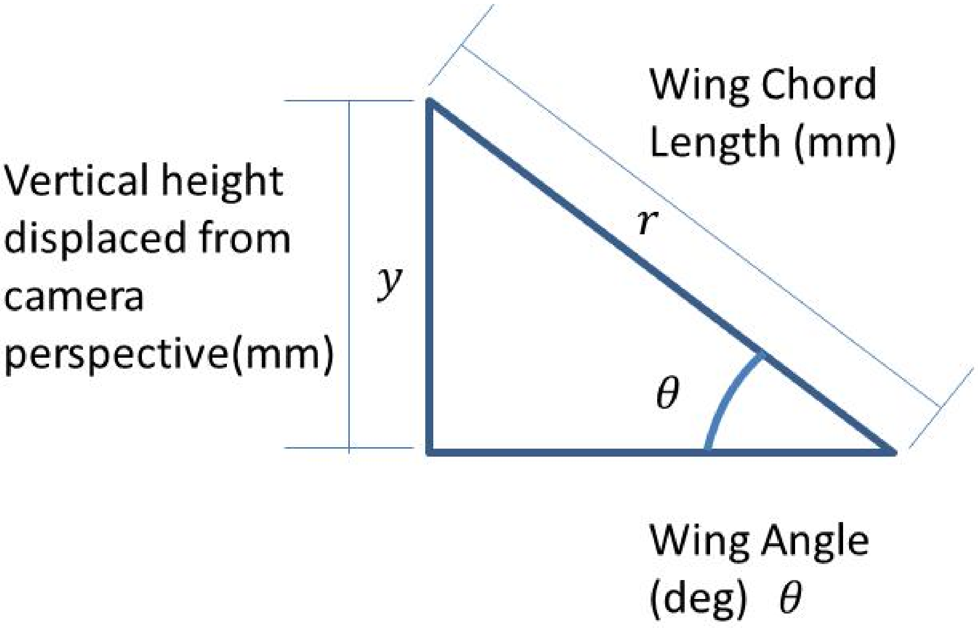

Figure 39: Geometric method used to determine the wing angle

Let it be noted that the angles calculated were from a reference point near the root of the wing where the wing is fairly rigid. An assumption will be made that the point used to measure the wing angle undergoes only rigid body motion. For the purposes of this experiment it is necessary to ensure the maximum upstroke and downstroke angles are approximately the values obtained from nature. Using trigonometry the wing angle can be approximated by Equation 12.

Equation 12

$$\theta = \sin^{-1}\frac{y}{r}$$

Relevant research was performed by Guiler where live *Manduca* were instrumented with tracking points where a sophisticated camera network and positioning system was able to track the wing stroke angles for multiple phases of flight, such as forward flight and hovering. The wing tracking system used had a reference point on the wing hinge and another near the root of the wing similar to the point chosen for the method described above for calculating the wing angle. Figure 40 presents Guiler's wing angle tracking data with respect to flight modes (Guiler 2011).

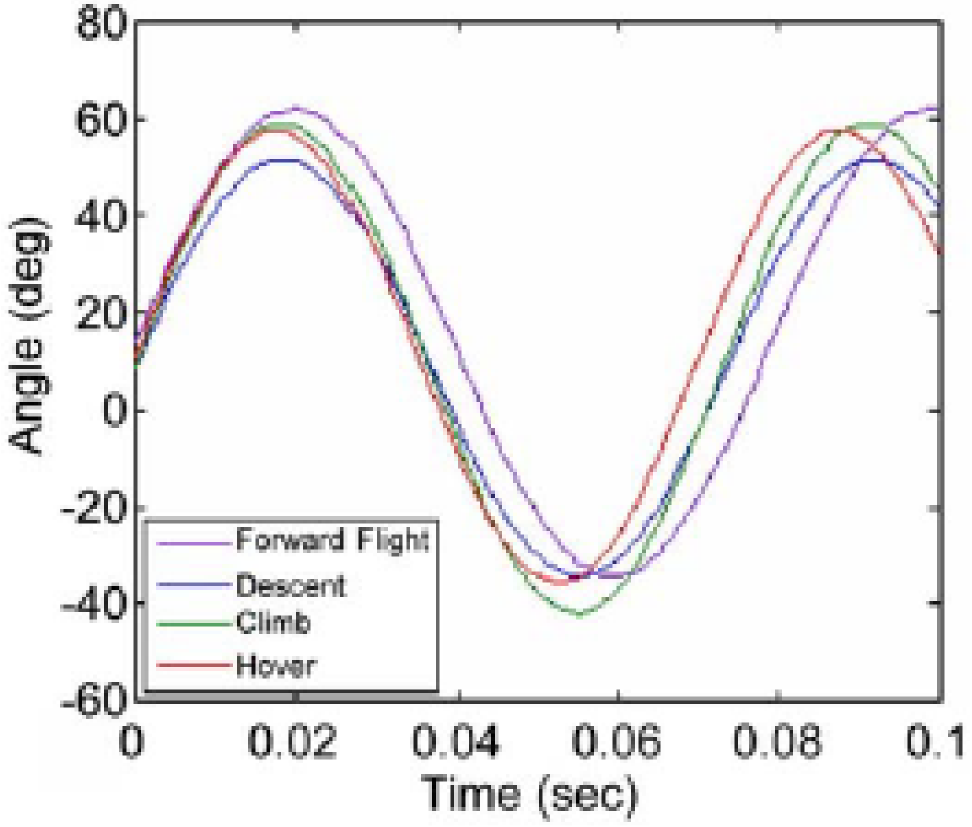

Figure 40: Wing stroke angles for multiple flight modes of the *M.sexta*

From the figure it is shown that during hovering flight the hawk moth's wing stroke amplitude is approximately + 55-60 deg to -35-40 deg.

Signal Processing

The signal processing comprised of three parts, two of which will be discussed here. These two are image tracking and implementing the post-processing low-pass filter. It was pointed out in the theory section that there are three parameters that are necessary in order to mechanically compute the power of a system, and they are force, displacement, and time. The force data is directly output from the signal communications code that executes the shaker movement and camera triggering. An example force plot for the longitudinal and vertical load cell is shown in Figure 41 and Figure 42. The force plots shown are post filtering.

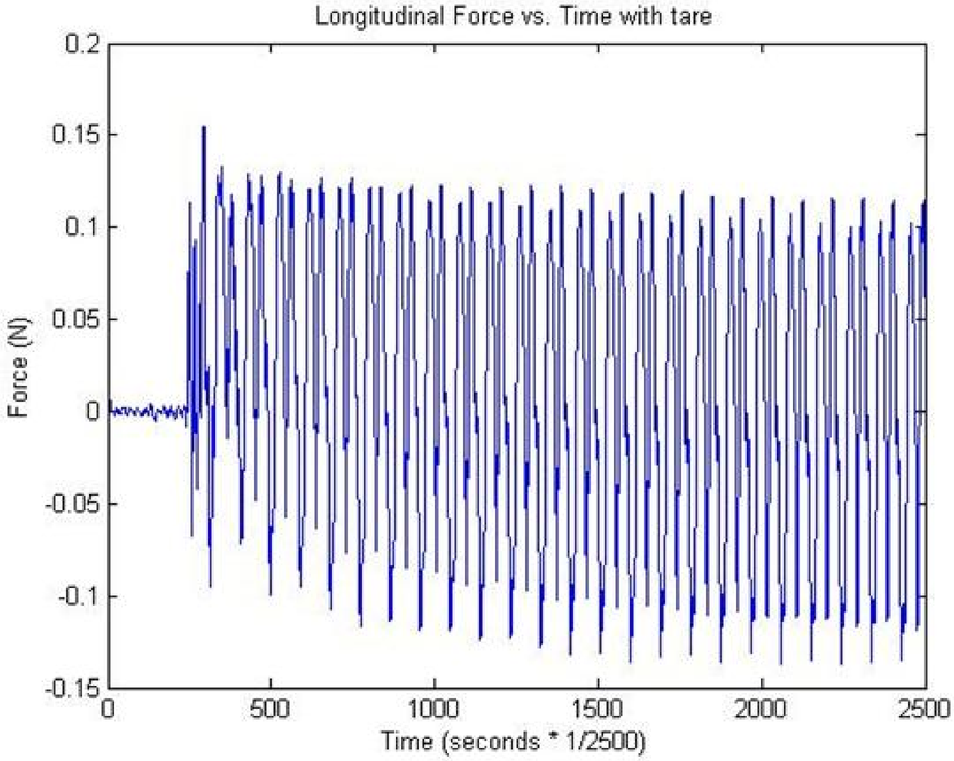

Figure 41: Longitudinal load cell force data, converted to Newton's and plotted vs. time.

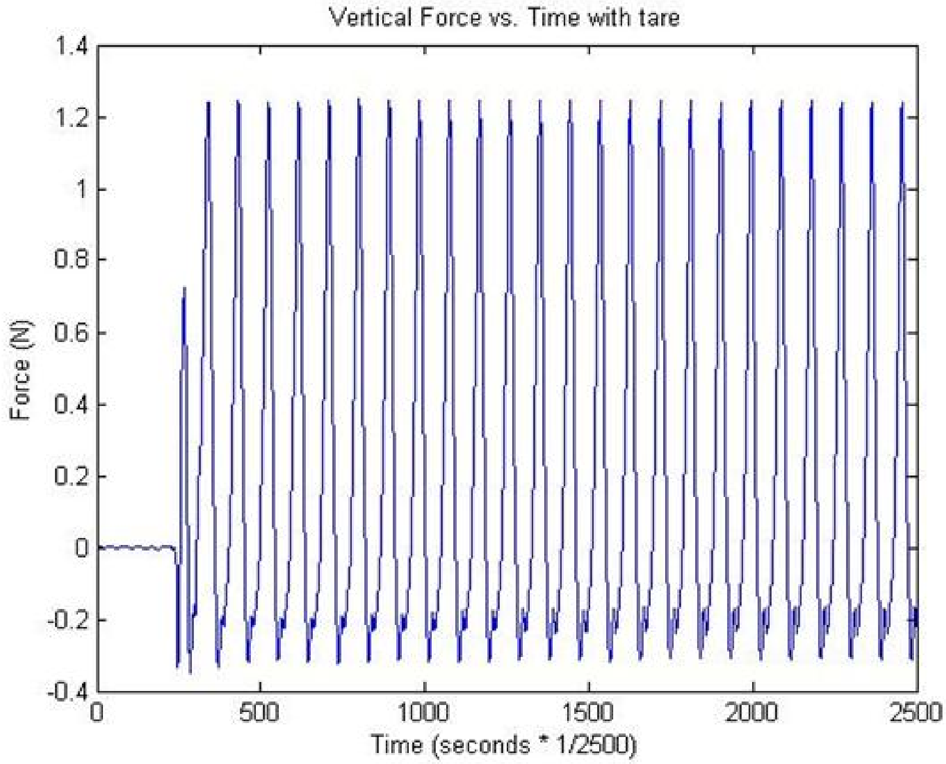

Figure 42: Vertical load cell force data, converted to Newton's and plotted vs. time.

From here the displacement of the shaker and linkage system is the next parameter necessary for the power computation. The displacement data for the shaker is back calculated from the images taken by the high speed camera. The images for a single run would be saved to an individual folder where the tracking code would be placed and ran. The point(s) tracking code was modified from a code written by Murray (Murray, O'Hara and Palazotto 2011), which was written to track up to a dozen points along a flapping *Manduca* wing. The code works by computing a normalized cross correlation between one image and the next, looking for the originally selected sub-image which should have moved only a few pixels between frames. In the case of the current experiment, the only pertinent motion to track was the vertical translation of the shaker, so only one sub-image was selected. A distinct shape with clear lines was found to be the most reliable tracking target, as shown in Figure 32. The program tracks the selected points in terms of pixel location in the image, therefore there is a need to convert that pixel location to a meaningful value. The originating pixel was set to a zero location and any variance off of that registered pixel indicated either a positive or negative value which was then converted to mm through a pixel to mm conversion factor. This factor typically remained constant for all test runs; the only way this value would change is if the camera was moved.

The next segment of the code uses a built in MatLab function to create a movie file of the acquired images. The coordinates of the tracked point were imposed, in the form of a red plus, on the images for the movie file, allowing the tracked point to be visualized as the movie plays. This helped indicate any oddities in the displacement data.

Lastly, the script creates displacement arrays for both the shaker and the longitudinal motion of the pivot. Figure 43 shows the respective segment of code.

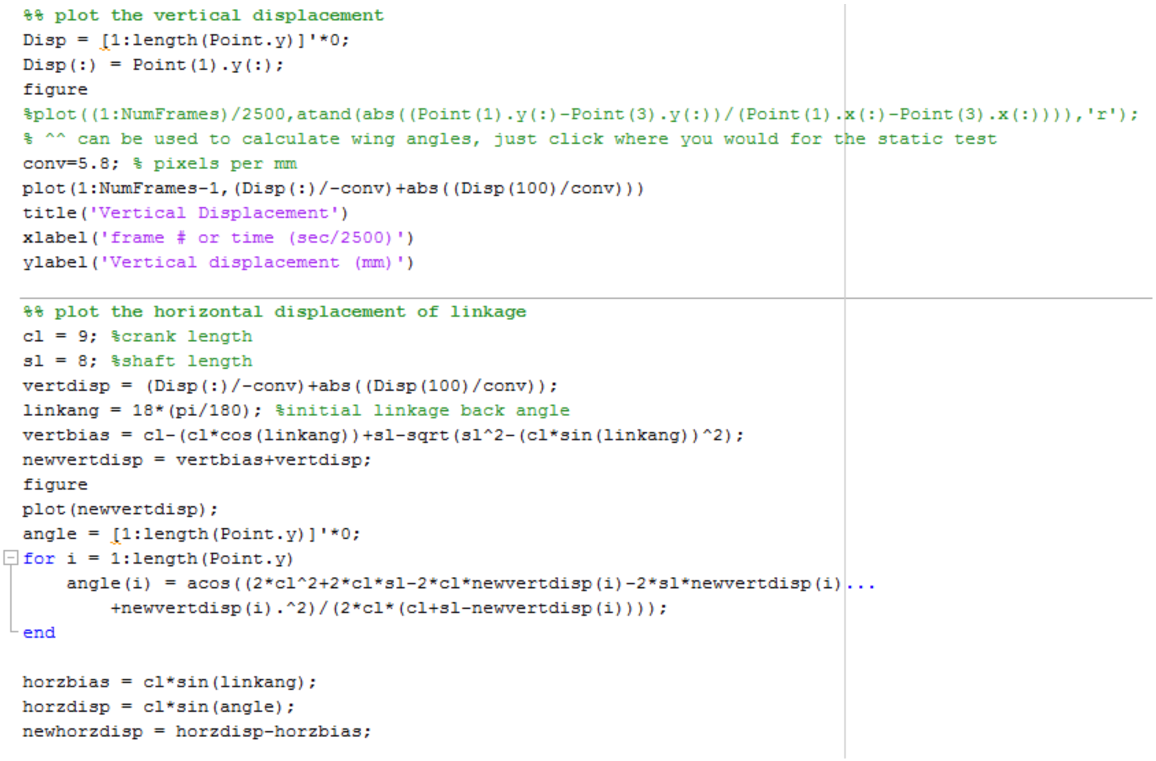

```
%% plot the vertical displacement
Disp = [1:length(Point.y)]'*0;
Disp(:) = Point(1).y(:);
figure
%plot((1:NumFrames)/2500,atand(abs((Point(1).y(:)-Point(3).y(:))/(Point(1).x(:)-Point(3).x(:)))),'r');
% ^^ can be used to calculate wing angles, just click where you would for the static test
conv=5.8; % pixels per mm
plot(1:NumFrames-1,(Disp(:)/-conv)+abs((Disp(100)/conv)))
title('Vertical Displacement')
xlabel('frame # or time (sec/2500)')
ylabel('Vertical displacement (mm)')

%% plot the horizontal displacement of linkage
cl = 9; %crank length
sl = 8; %shaft length
vertdisp = (Disp(:)/-conv)+abs((Disp(100)/conv));
linkang = 18*(pi/180); %initial linkage back angle
vertbias = cl-(cl*cos(linkang))+sl-sqrt(sl^2-(cl*sin(linkang))^2);
newvertdisp = vertbias+vertdisp;
figure
plot(newvertdisp);
angle = [1:length(Point.y)]'*0;
for i = 1:length(Point.y)
    angle(i) = acos((2*cl^2+2*cl*sl-2*cl*newvertdisp(i)-2*sl*newvertdisp(i)...
        +newvertdisp(i).^2)/(2*cl*(cl+sl-newvertdisp(i))));
end

horzbias = cl*sin(linkang);
horzdisp = cl*sin(angle);
newhorzdisp = horzdisp-horzbias;
```

Figure 43: Matlab code that generates the numerical arrays of vertical displacement of the shaker and longitudinal displacement of the pivot.

The first segment of the code as described above creates an array the length of the number of images filled with the y-coordinate values of the tracked point. The arrays values are then converted from pixels to mm. The conversion factor is determined by taking a known measurement value in an image and correlating that to a pixel equivalent. The images produced by the camera were 512x512 pixels resolution. A negative conversion factor is necessary to construct the correct manipulation of the pixel data. The pixels are numbered (0, 0) at the top left and increase to the bottom right (512,512). Therefore, to match an upward direction of the shaker, meaning a positive pixel difference the pixel information was flipped by the negative sign on the conversion factor. The second segment of this code generates the horizontal displacement of the pivot point on the linkage. For the linkage kinematics, in order to solve for the displacement of interest one variable is necessary, the crank angle, however in order to obtain that value it can either be visually captured from the images or back calculated from the vertical displacement of the shaker. Three values are necessary to obtain the crank angle, slider displacement, and the linkage arm lengths. The arm lengths are fixed based on the design and the slider displacement was computed in the above code segment. In order to calibrate the pivot displacement from its initial starting point, the initial crank angle was required. This was determined by manually measuring the angle of the crank from the camera images during the tare period. With the starting point of the linkage system and the vertical displacement of the shaker known, the angle can be computed from the vertical displacement and therefore the horizontal displacement of the pivot is calculated. The values of displacement are again centered on the starting point of the system. A negative pivot displacement corresponds to movement toward the specimen. The units of the angle are in radians and the lengths and displacements are in mm. An example vertical and horizontal displacement and crank angel plots are shown in Figure 44, Figure 45, and Figure 46.

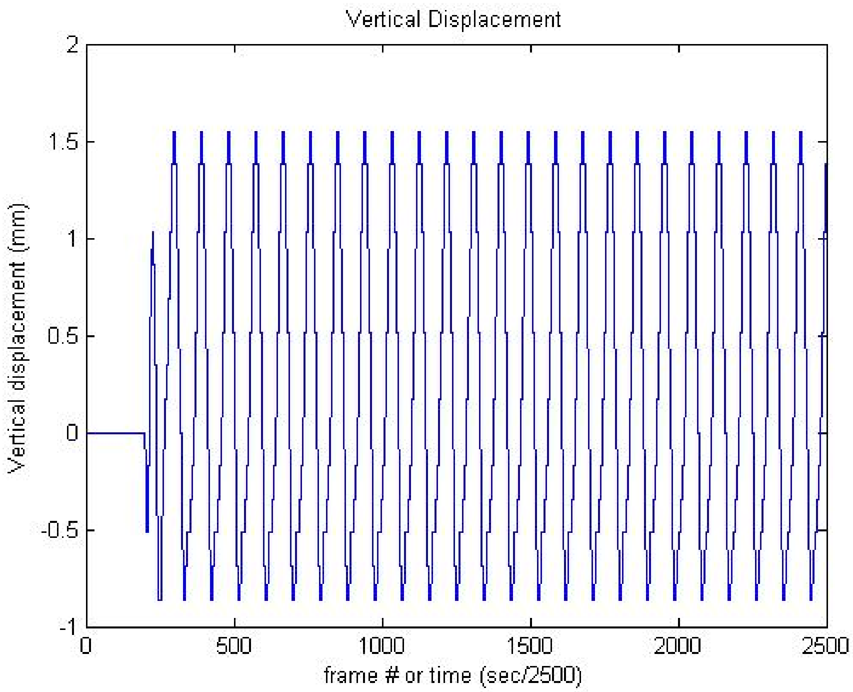

Figure 44: Vertical displacement of the shaker vs. time

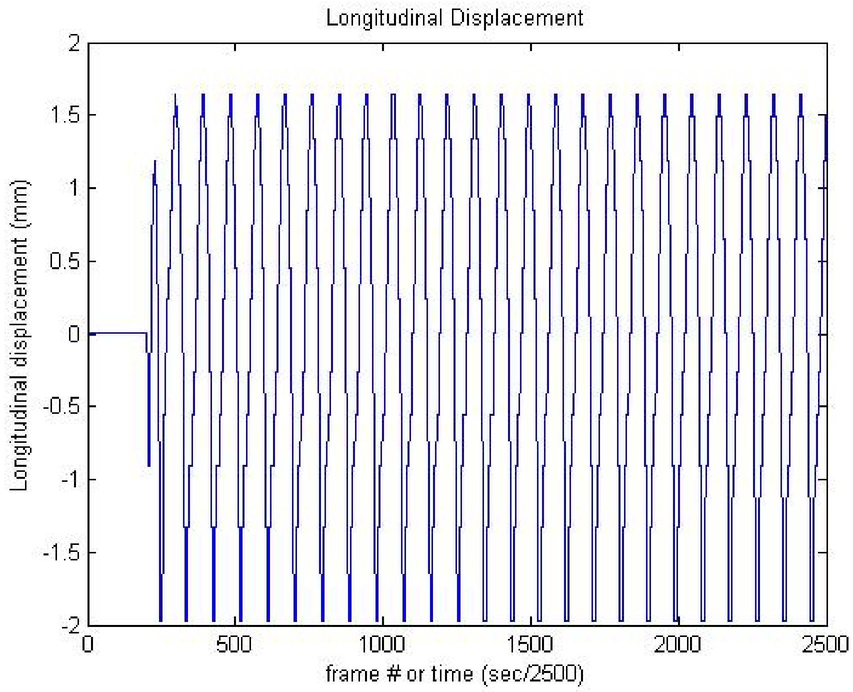

Figure 45: Longitudinal displacement of the pivot vs. time

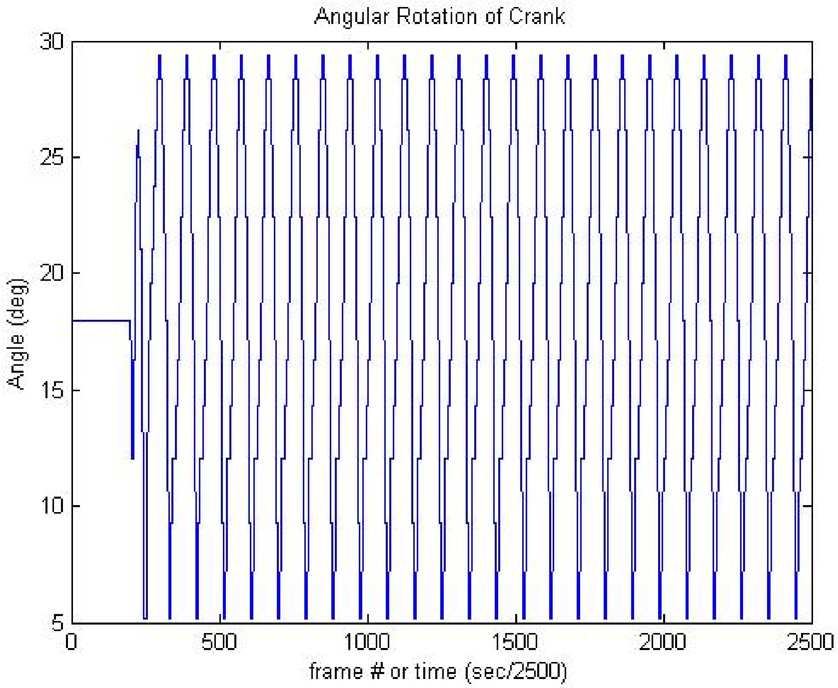

Figure 46: Crank angle position vs. time

For the power calculation processing, when the force data was filtered an added known phase shift occurred and to ensure the force and displacement data matched up, frame for frame, the displacement data was filtered as well (producing mainly just a phase shift of the data).

Power Calculation

With everything now known to calculate the mechanical power output: force, displacement, and time, the first step to computing the power was to determine where contact began on the tergum and phragma and when the corresponding compression ended. This was determined by analyzing the force and displacement data and the camera images. Originally the initial contact point was determined by the combination of the camera image data and the force data. Typically, when contact began, there was a rise in the load cell data from a minimum value in the no-wings condition as opposed to that of the with-wings case where no increase in force was indicated. Initially it was thought that the load cells were not sensitive enough to sense the initial loading by the contact compression of the tergum or phragma due a corresponding flat force signal when contact was observed (A. C. Hollenbeck 2011). The analysis of the wings, no-wings scenarios proved that the flat period in the load data was indeed caused by the inertia and aerodynamic forces on the wings as they are forced to flap by the mechanism. It was confirmed through analysis of many data sets with wings off that the increase in force from a minimum was indeed the frame that contact was made with the tergum or phragma. With this being true a script was written to scan the vertical and longitudinal force data sets to pull out a data time stamp where the force was minimum over a scanned time span for each flap period. An array of 24 points was developed for the corresponding 25 flaps during the 1 second of recording. The first flap forces are typically low in amplitude as the system is approaching steady state for the first couple flaps so the first flap is ignored for power considerations. The entire code is displayed in Figure 47. The version displayed represents the code for the vertical force. The codes are nearly identical for the vertical and horizontal forces and are shown in full in Appendix B-F.

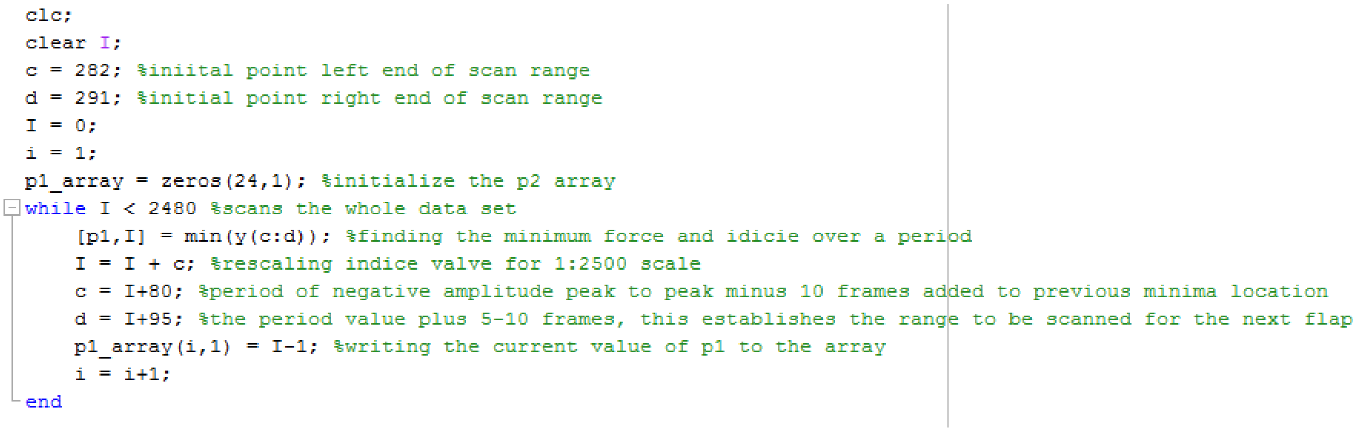

```
clc;
clear I;
c = 282; %iniital point left end of scan range
d = 291; %initial point right end of scan range
I = 0;
i = 1;
p1_array = zeros(24,1); %initialize the p2 array
while I < 2480 %scans the whole data set
    [p1,I] = min(y(c:d)); %finding the minimum force and idicie over a period
    I = I + c; %rescaling indice valve for 1:2500 scale
    c = I+80; %period of negative amplitude peak to peak minus 10 frames added to previous minima location
    d = I+95; %the period value plus 5-10 frames, this establishes the range to be scanned for the next flap
    p1_array(i,1) = I-1; %writing the current value of p1 to the array
    i = i+1;
end
```

Figure 47: Matlab code for scanning the load array for minimum values just as contact is made.

This code functions by setting up an initial frame range to scan for a minimum value. This must be determined by visually inspecting the force and image data for the first minimum amplitude peak before contact was made for the first flap. From here the period of this value for flap to flap was determined and was used to establish the next scanning region. The period was fairly constant from flap to flap differing by a couple frames maximum which is why an area around the period is scanned for the minimum value to account for the potential couple frame difference. The p1_array is then formulated which contains the 24 frame values corresponding to the point of contact.

A similar code was developed in order to determine the end of the compression of the tergum or phragma. This code is shown in Figure 48. This code performs identically the same operation except it uses the displacement data and scans for maximum values of displacement. This generates a p2_array which denotes the frame numbers where maximum displacement/compression occurs for each flap.

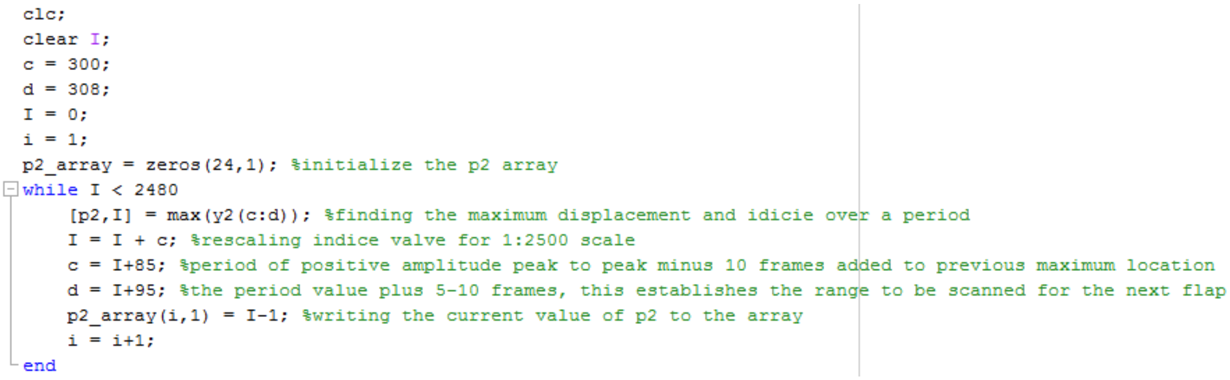

```
clc;
clear I;
c = 300;
d = 308;
I = 0;
i = 1;
p2_array = zeros(24,1); %initialize the p2 array
while I < 2480
    [p2,I] = max(y2(c:d)); %finding the maximum displacement and idicie over a period
    I = I + c; %rescaling indice valve for 1:2500 scale
    c = I+85; %period of positive amplitude peak to peak minus 10 frames added to previous maximum location
    d = I+95; %the period value plus 5-10 frames, this establishes the range to be scanned for the next flap
    p2_array(i,1) = I-1; %writing the current value of p2 to the array
    i = i+1;
end
```

Figure 48: Matlab code for scanning the displacement array for maximum values just as contact is made.

These values for the p1 and p2 arrays were then entered in to the final power processing code, which calculates the power for each of the 24 flaps characterized by the location finding codes. The final processing code required that the force, displacement, and p1/p2 array data points were loaded into the variable workspace within MatLab. This was accomplished by loading the saved load and displacement workspaces into MatLab and running the location finder codes to have all of the variables in the workspace. The power calculation code used the p1/p2 array values in order to determine the frame ranges to compute the work and power output for each flap. The segment of the code that details this is shown in Figure 49.

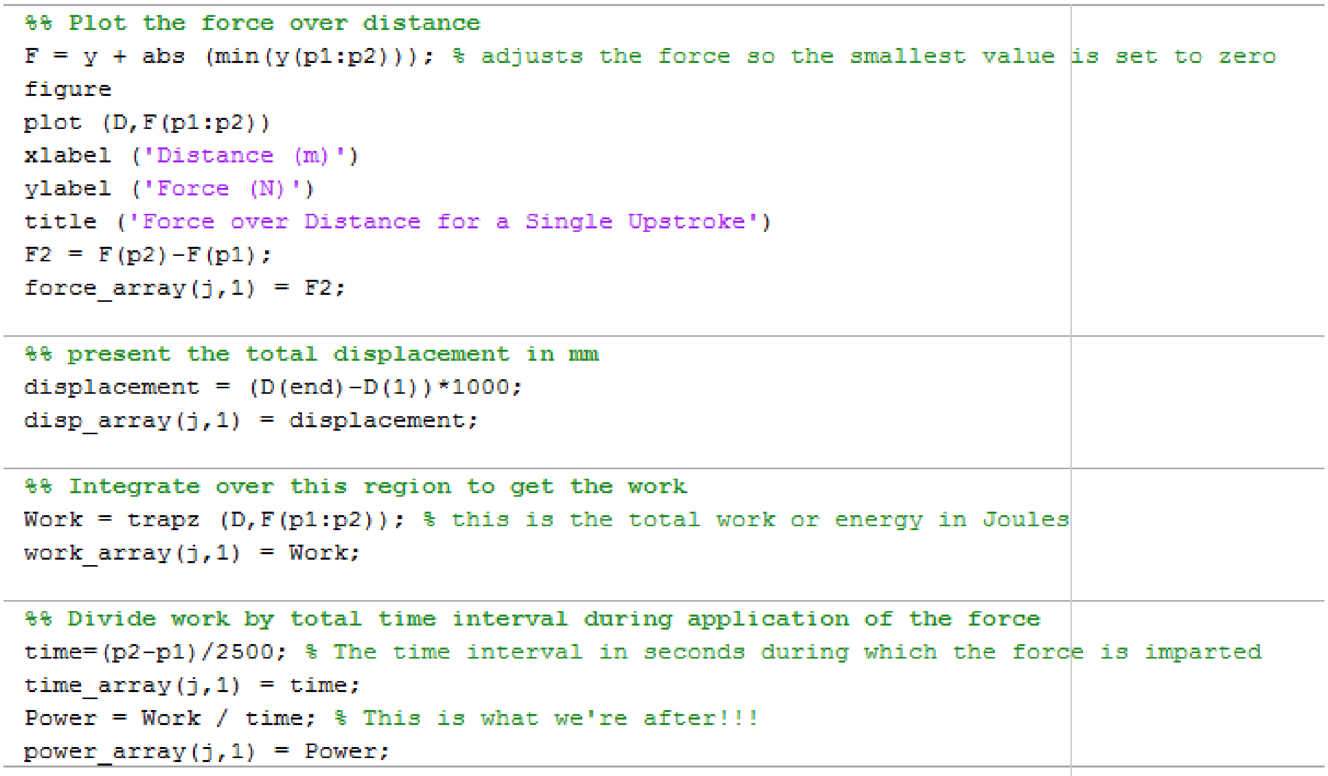

```
%% Plot the force over distance
F = y + abs (min(y(p1:p2))); % adjusts the force so the smallest value is set to zero
figure
plot (D,F(p1:p2))
xlabel ('Distance (m)')
ylabel ('Force (N)')
title ('Force over Distance for a Single Upstroke')
F2 = F(p2)-F(p1);
force_array(j,1) = F2;

%% present the total displacement in mm
displacement = (D(end)-D(1))*1000;
disp_array(j,1) = displacement;

%% Integrate over this region to get the work
Work = trapz (D,F(p1:p2)); % this is the total work or energy in Joules
work_array(j,1) = Work;

%% Divide work by total time interval during application of the force
time=(p2-p1)/2500; % The time interval in seconds during which the force is imparted
time_array(j,1) = time;
Power = Work / time; % This is what we're after!!!
power_array(j,1) = Power;
```

Figure 49: Matlab code for the numerical computation of absolute power with the recorded force and displacement data.

The first part of the code is modifying the force array over the p1/p2 range such that the minimum value is set to zero and all others are biased up. This bias is added because the values of force used to compute work must be positive values. An example single flap force and displacement data set for an upstroke and downstroke is shown in Figure 52. Next, the work and power are computed. The work is numerically integrated by using a built in MatLab function *trapz*, the integration is of the force over with the displacement being the limits. Lastly, the power is computed by taking the work value and dividing it by the time interval that the work occurred over. This series of calculations is in a *while* loop and runs 24 times for each set of p1/p2 points. All of the displacement, time, work, and power values are saved to respective arrays containing the information for all 24 flaps. The power is then averaged over the series of flaps to get an average power to perform the respective motion, upstroke or downstroke. The ability to compute all of those variables for each individual flap allows for a more in depth power analysis for the full flapping stroke. The important trends that were searched for during the analysis of all of the flaps were consistency and overall repeatable data from flap to flap. A close up view of a force vs. displacement chart for the vertical and longitudinal motion is shown in Figure 50and Figure 51.

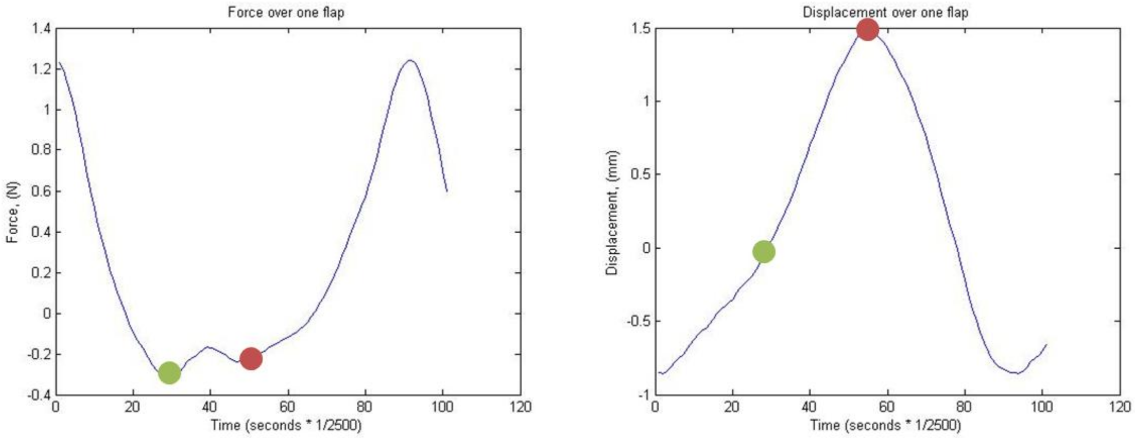

Figure 50: The range of force and displacement from green to red (grey to black) for the upstroke.

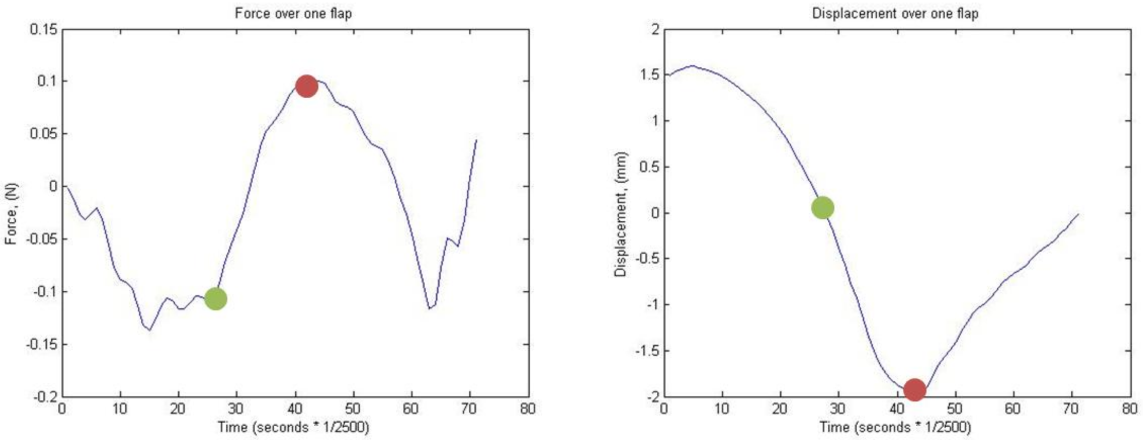

Figure 51: The range of force and displacement from green to red (grey to black) for the downstroke.

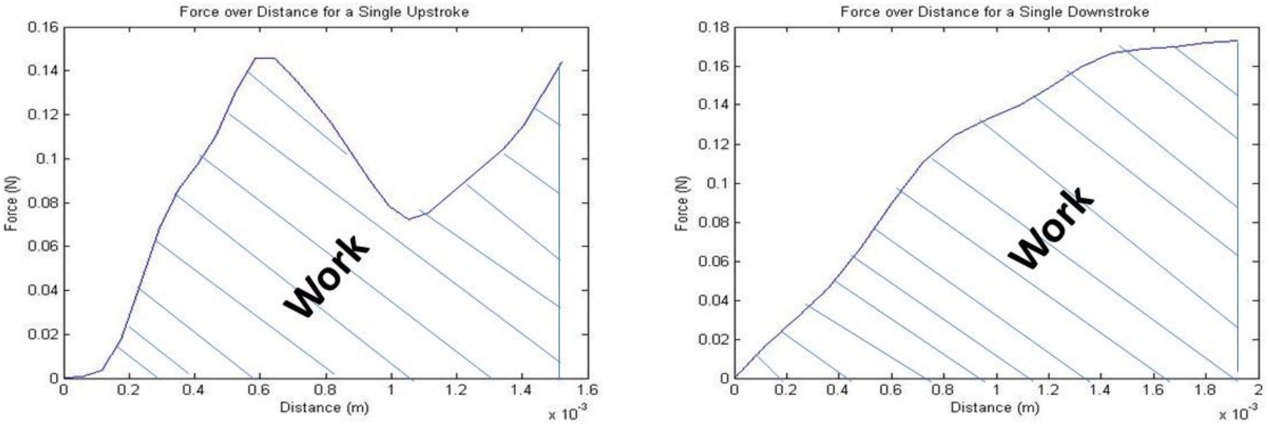

Figure 52: Close-up view of the Force vs. Displacement for the upstroke (right) and the downstroke (right).

Experiment Summary

The experimentation process presented required many failed attempts at data acquisition, set-up, and procedure. However, through these failed attempts and incessant analysis much insight was gained on how exactly to conduct the experiment so that accurate and reliable results could be generated. This chapter detailed the design and construction of the experimental apparatus, specimen preparation, wing angle approximation, the Matlab code written and utilized for the experimentation, and the initial processing methods of the data acquired.

V. Results and Discussion

The modified dynamic load experiment was implemented to simultaneously determine the power output of the DVM's and DLM's for 5 *Manduca sexta* specimens. The average mechanical power required to produce the upstroke and downstroke replicating the natural flapping motion of the *M. sexta* was found to be 13.34 ± 1.08 mW and 31.36 ± 2.55 mW respectively totaling to 44.92 mW. The respective flap angles for the power results were calculated based on the trigonometry relationship in Equation 12 to be a 60 deg upstroke and a 35 deg downstroke. These values were confirmed to be the flap amplitudes observed by the *Manduca* in nature during hovering flight as shown by the work performed by Guiler in Figure 40. The results provided for displacement, time, work, and power are all averages of flap number 15-25 in Figure 56 and Figure 57. The average was taken at this point because this is where steady-state flapping was determined to occur for most cases. One definite distinct difference occurred when analyzing the wings vs. no-wings results. Frequently, but not observed in all wings cases the absolute power for the upstroke was initially large and as the flaps continued the power decreased by approximately half to a steady state value. This is shown in Figure 53. Let it be noted that for this test and others that observed this trend the force vs. displacement plots for all flaps were nearly identical in trend only the amplitudes lessened as flaps progressed. The resulting power array could have many implications such as, a settling time for the moth to reach steady state flapping, the initial flaps are the most energy demanding and require an energy density of approximately 216 W/kg (roughly double what is required for steady state flapping (112 W/kg)), and elastic energy storage of the thorax as it becomes energized. On the other hand all of the no-wings cases did not display this trend and had more consistent absolute power measurements spanning all flaps. This is shown in Figure 54 and Figure 55. Another point of interest that was observed was that the absolute power required for the no-wings case equals approximately the settled steady state value of that reached for the with-wings cases. If the assumption is made that the steady with-wings case and no-wings case produce approximately equal values of absolute power, which was observed, then combining the resulting power data would be justified. The resulting charts shown in Figure 56 and Figure 57 do combine the with-wings cases and no-wings cases for an averaged absolute power required for the upstroke and downstroke.

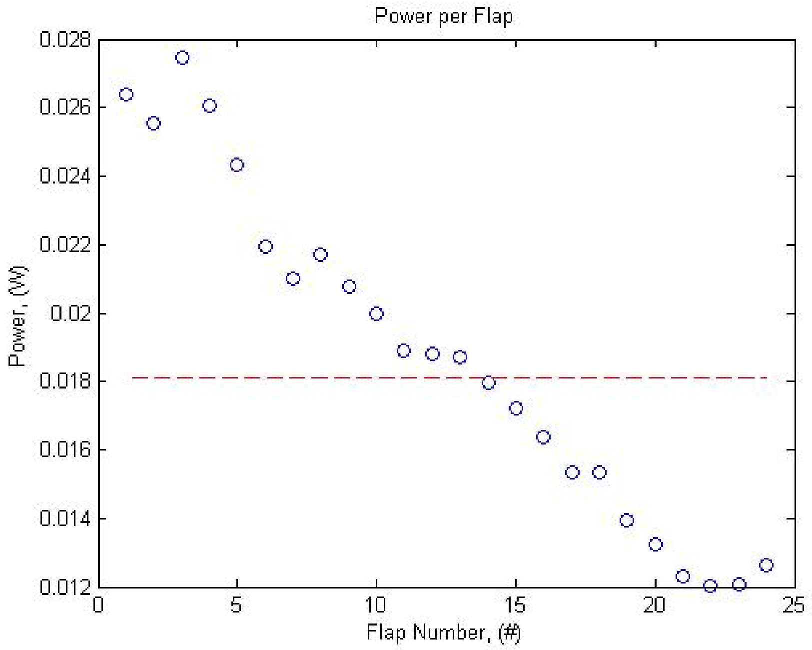

Figure 53: Absolute Power per Flap for upstroke for the 11/5/12 with-wings specimen test (red dashed line is the average for last 15 flaps)

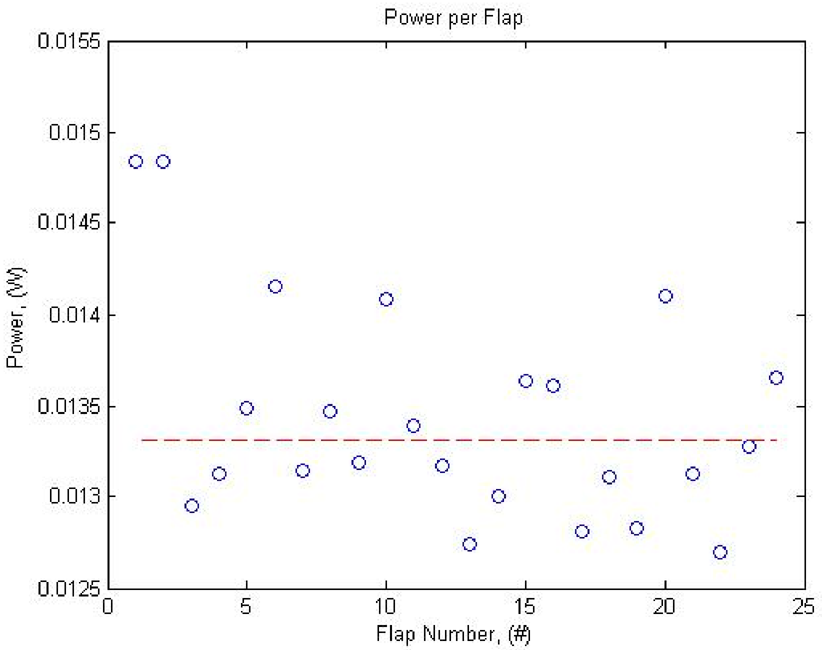

Figure 54: Absolute Power per Flap for upstroke for the 11/12/12 with no-wings specimen test (red dashed line is the average for last 15 flaps)

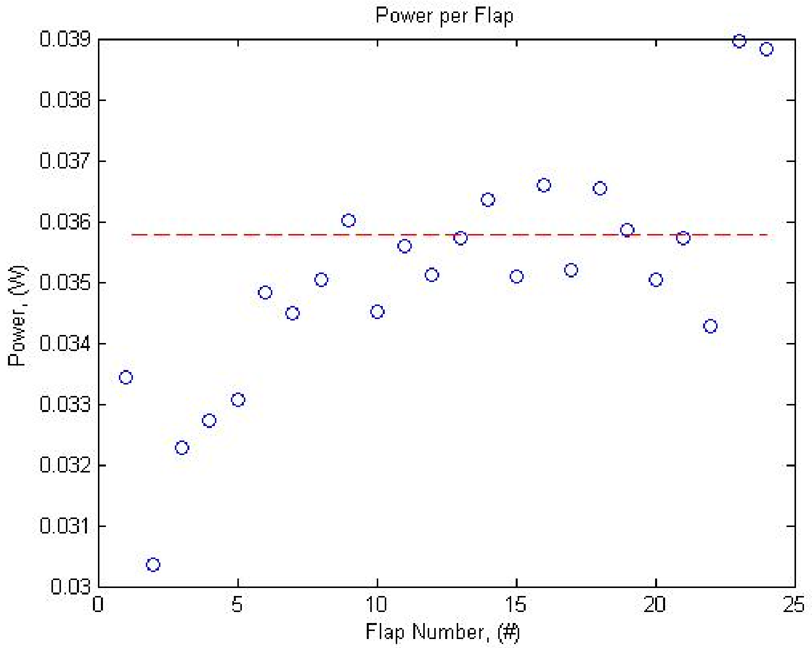

Figure 55: Absolute Power per Flap for downstroke for the 11/12/12 with no-wings specimen test (red dashed line is the average for last 15 flaps)

Upstroke Power Data						
Specimen	Date	Mass (g)	Disp (mm)	Time (ms)	Work (J) x10^{-4}	Power (mw)
1	10/17/2012	1.74	1.16	9.3	1.42	15
2	10/18/2012	1.82	1.09	9.6	1.28	13.4
3	11/5/2012	1.95	1.56	10.5	1.27	12
4	11/12/2012	1.85	1.47	10.2	1.37	13.3
5	11/14/2012	1.7	1.5	10.3	1.34	13
Average		1.81	1.36	9.98	1.34	13.34
St.Dev		0.10	0.21	0.51	0.06	1.08

Figure 56: Upstroke Power Data for the 5 test specimens (first 3 with-wings, last two without wings).

Downstroke Power Data						
Specimen	Date	Mass (g)	Disp (mm)	Time (ms)	Work (J) x10^{-4}	Power (mw)
1	10/17/2012	1.74	1.44	4.8	1.45	30.7
2	10/18/2012	1.82	1.41	5.9	1.82	31
3	11/5/2012	1.95	1.79	5.6	1.61	28.5
4	11/12/2012	1.85	1.94	6.4	2.25	35.5
5	11/14/2012	1.7	1.94	5.8	1.8	31.1
Average		1.81	1.70	5.70	1.79	31.36
St.Dev		0.10	0.26	0.58	0.30	2.55

Figure 57: Downstroke Power Data for the 5 test specimens (first 3 with-wings, last two without wings).

The value of power obtained here is the absolute power required for these muscle groups to accomplish the respective wing movements. In order for comparison to other muscular groups and energy storage systems, the absolute power is divided by the mass of the working unit. In this case, the absolute power per stroke will be divided by their respective mass percentage of muscle. This term is referred to as the specific power density. For the purposes of the research, the moth’s muscles were not extracted and weighed because the dissection skills necessary were outside the scope of this project. However, extensive research was performed on mass percentages of the various segments of the *Manduca*. The chart shown in Figure 58 displays the body parameters, mass fractions, of the thorax, muscle, and abdomen weight with respect to the total mass of the specimen. The documentation detailed by Willmott and Ellington presents that an average muscle mass to body mass percentage is 27 percent for males and 17.7 percent for females (Willmott and Ellington 1997). An average of this value was taken for the purposes of the research to estimate a specific power density of the DVMs and DLMs. Figure 59 displays a chart plotting the specific power density of the DVMs, DLMs, and the combination of the two. The DVM and DLM plots vary with respect to percentage values, 15-40%, 85-60%, respectively of 22 percent assumed muscle mass of the specimen. This is a percentage of the assumed 22 percent muscle mass of the specimen. In varying the muscle mass percentages it was found that there is a ratio of DVM to DLM that equates to an equal power density between the two. This was approximately 30% DVM to 70% DLM muscle mass equaling the value of 112 W/kg muscle. The hawkmoth in nature exhibits muscle mass ratios of the order presented (30/70) therefore confirming what was found to be the muscle mass ratio which yielded an equal power density. The total power density was also plotted with respect to total muscle mass percentage (15-40%). This value analyzed over the muscle mass range that Willmott presented produces specific power density values of 140-91 W/kg muscle. Figure 60 contains a table with the specific power density values presented in the literature review and from a few other sources to compare these values with those developed by the experiment and technique presented.

This experiment yielded a power density which lies very close to the bulk of the accepted data presented. The most reliable results involve those that experimented directly with the specimen or muscles themselves. These were the work presented by Pennycuick, Stevenson and Josephson, and Tu. Their results fell within the range of 82-97 W/kg muscle. The other experiments values are less reliable as applied to muscles themselves because they obtain the power value indirectly with computational or numerical models and equations. In order to do this, the models typically require numerous assumptions and simplifications which make the results less reliable. One experiment in particular that yielded a value that is indeed high was Casey’s prediction. The main cause of the overestimation was the use of the 20% efficiency factor for the muscles. It has since been shown by Josephson and Tu that this value lies more in the range of 5-10% which drives Casey’s estimate to 102-135 W/kg muscle mass. Using the now more accepted value for the muscle efficiency Casey’s estimates fall within the rest of the presented results. These values particularly fall exactly within the results of the dynamic load experiment.

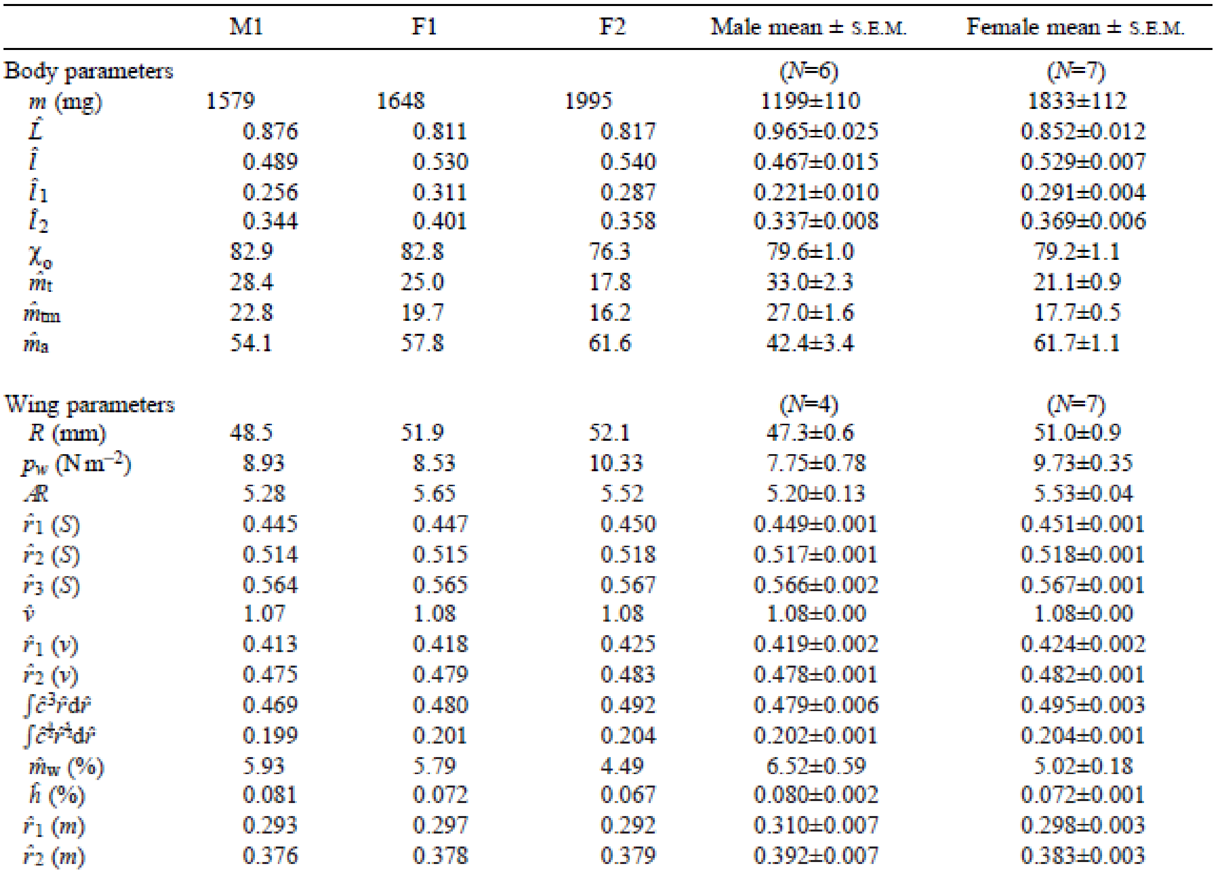

	M1	F1	F2	Male mean ± S.E.M.	Female mean ± S.E.M.
Body parameters				(*N*=6)	(*N*=7)
m (mg)	1579	1648	1995	1199±110	1833±112
$\hat{L}$	0.876	0.811	0.817	0.965±0.025	0.852±0.012
$\hat{l}$	0.489	0.530	0.540	0.467±0.015	0.529±0.007
$\hat{l}_1$	0.256	0.311	0.287	0.221±0.010	0.291±0.004
$\hat{l}_2$	0.344	0.401	0.358	0.337±0.008	0.369±0.006
χ_o	82.9	82.8	76.3	79.6±1.0	79.2±1.1
$\hat{m}_t$	28.4	25.0	17.8	33.0±2.3	21.1±0.9
$\hat{m}_{tm}$	22.8	19.7	16.2	27.0±1.6	17.7±0.5
$\hat{m}_a$	54.1	57.8	61.6	42.4±3.4	61.7±1.1
Wing parameters				(*N*=4)	(*N*=7)
R (mm)	48.5	51.9	52.1	47.3±0.6	51.0±0.9
p_w ($\mathrm{N\,m^{-2}}$)	8.93	8.53	10.33	7.75±0.78	9.73±0.35
$\mathcal{R}$	5.28	5.65	5.52	5.20±0.13	5.53±0.04
$\hat{r}_1$ (S)	0.445	0.447	0.450	0.449±0.001	0.451±0.001
$\hat{r}_2$ (S)	0.514	0.515	0.518	0.517±0.001	0.518±0.001
$\hat{r}_3$ (S)	0.564	0.565	0.567	0.566±0.002	0.567±0.001
$\hat{v}$	1.07	1.08	1.08	1.08±0.00	1.08±0.00
$\hat{r}_1$ (v)	0.413	0.418	0.425	0.419±0.002	0.424±0.002
$\hat{r}_2$ (v)	0.475	0.479	0.483	0.478±0.001	0.482±0.001
$\int \hat{c}^3 \hat{r} d\hat{r}$	0.469	0.480	0.492	0.479±0.006	0.495±0.003
$\int \hat{c}^{\frac{1}{2}} \hat{r}^{\frac{3}{2}} d\hat{r}$	0.199	0.201	0.204	0.202±0.001	0.204±0.001
$\hat{m}_w$ (%)	5.93	5.79	4.49	6.52±0.59	5.02±0.18
$\hat{h}$ (%)	0.081	0.072	0.067	0.080±0.002	0.072±0.001
$\hat{r}_1$ (m)	0.293	0.297	0.292	0.310±0.007	0.298±0.003
$\hat{r}_2$ (m)	0.376	0.378	0.379	0.392±0.007	0.383±0.003

Figure 58: Weight Parameters of *M.sexta* as determined by Willmott

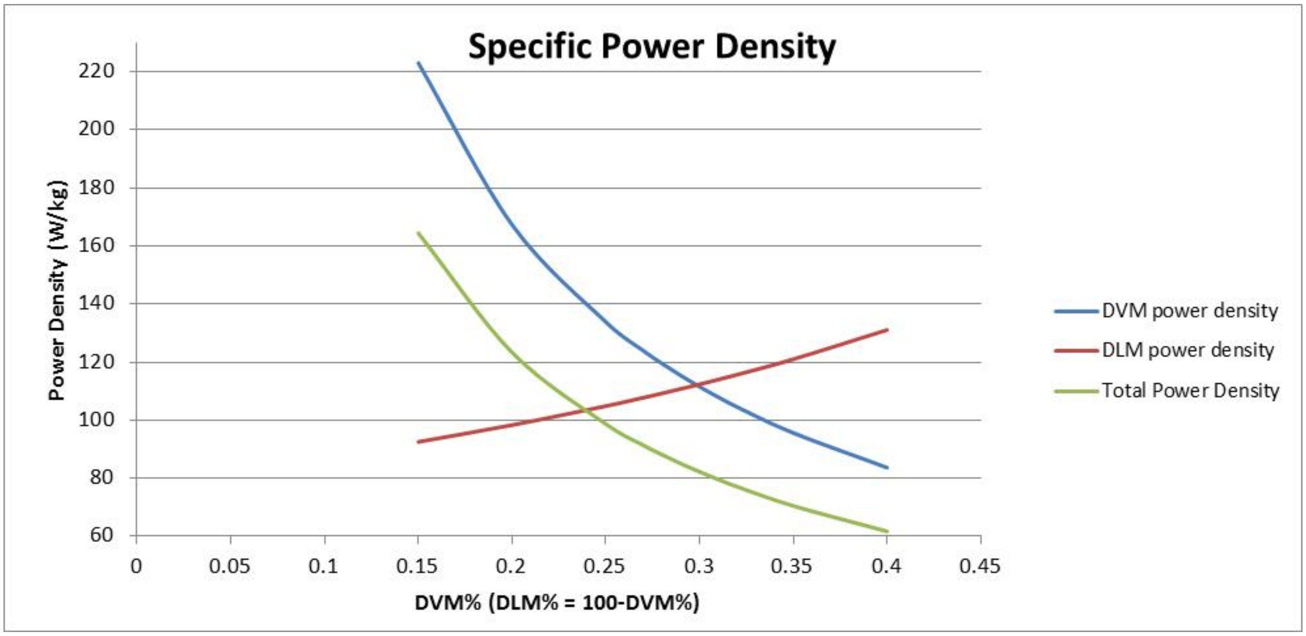

Figure 59: Specific power density of the DVM's and DLM's ranging in percentage density and Total power density ranging in total muscle mass weight percentage.

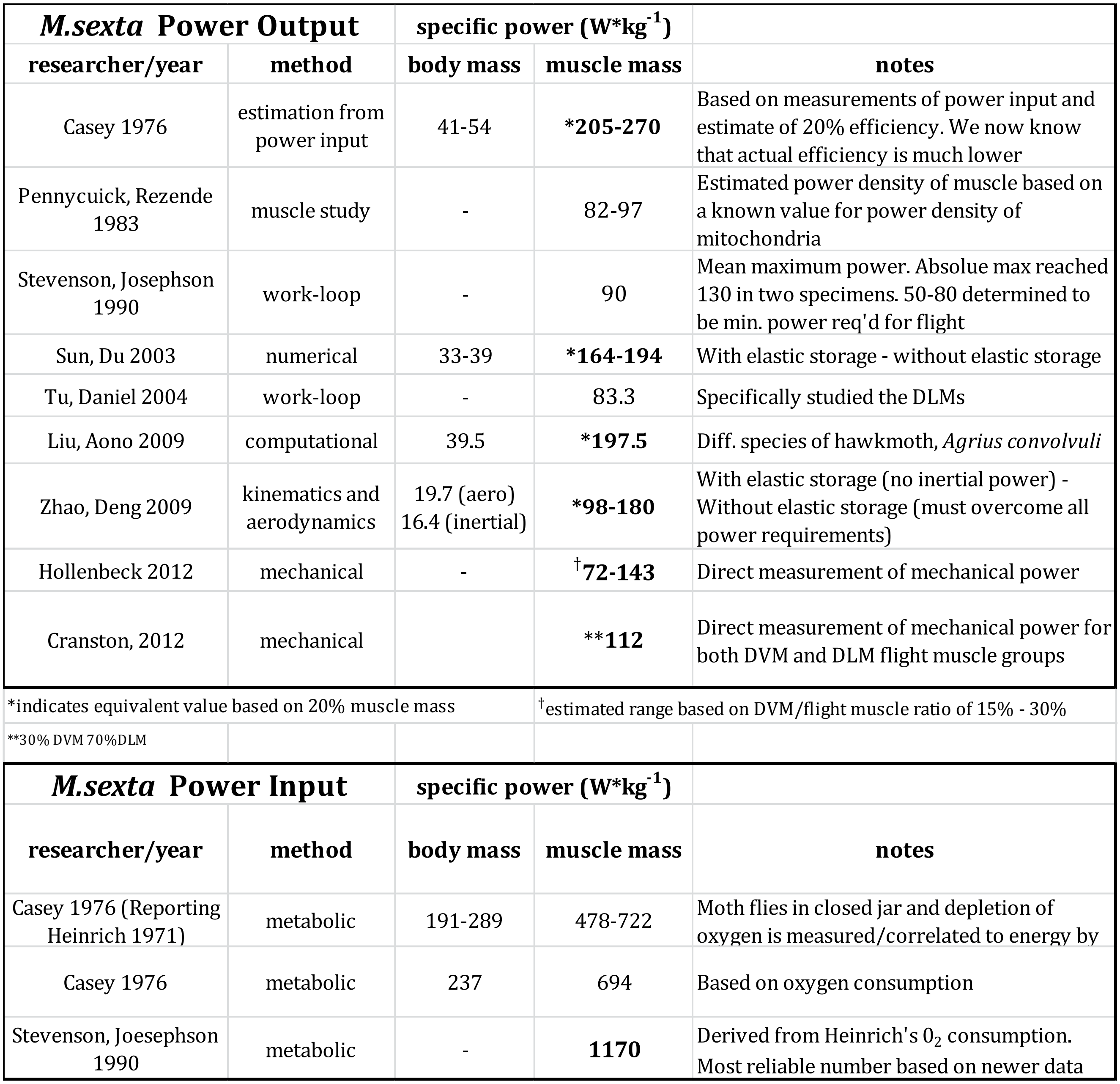

M.sexta Power Output		specific power (W*kg^{-1})		
researcher/year	**method**	**body mass**	**muscle mass**	**notes**
Casey 1976	estimation from power input	41-54	***205-270**	Based on measurements of power input and estimate of 20% efficiency. We now know that actual efficiency is much lower
Pennycuick, Rezende 1983	muscle study	-	82-97	Estimated power density of muscle based on a known value for power density of mitochondria
Stevenson, Josephson 1990	work-loop	-	90	Mean maximum power. Absolute max reached 130 in two specimens. 50-80 determined to be min. power req'd for flight
Sun, Du 2003	numerical	33-39	***164-194**	With elastic storage - without elastic storage
Tu, Daniel 2004	work-loop	-	83.3	Specifically studied the DLMs
Liu, Aono 2009	computational	39.5	***197.5**	Diff. species of hawkmoth, *Agrius convolvuli*
Zhao, Deng 2009	kinematics and aerodynamics	19.7 (aero) 16.4 (inertial)	***98-180**	With elastic storage (no inertial power) - Without elastic storage (must overcome all power requirements)
Hollenbeck 2012	mechanical	-	†**72-143**	Direct measurement of mechanical power
Cranston, 2012	mechanical		****112**	Direct measurement of mechanical power for both DVM and DLM flight muscle groups

*indicates equivalent value based on 20% muscle mass

†estimated range based on DVM/flight muscle ratio of 15% - 30%

**30% DVM 70%DLM

M.sexta Power Input		specific power (W*kg^{-1})		
researcher/year	**method**	**body mass**	**muscle mass**	**notes**
Casey 1976 (Reporting Heinrich 1971)	metabolic	191-289	478-722	Moth flies in closed jar and depletion of oxygen is measured/correlated to energy by
Casey 1976	metabolic	237	694	Based on oxygen consumption
Stevenson, Joesephson 1990	metabolic	-	**1170**	Derived from Heinrich's 0_2 consumption. Most reliable number based on newer data

Figure 60: Specific power output from the various sources in the literature review. Specific power density comparison chart.

Results Summary

The dynamic load experiment reproduced the entre wing stoke replicating hovering in the *M.sexta* while measuring the absolute power required to reproduce the wing motion. The absolute value was associated to the individual flight muscle groups and as an entire mass of unity. The results of this experiment were in agreement with other research presented on the measured mechanical specific power density of the *M.sexta* flight muscles. The value of specific power density found was to be 112 W/kg at a 70/30 ratio of DLM to DVM muscle mass percentage.

VI. Conclusions

Experimental Technique

The dynamic load apparatus is the only of its kind to mechanically compresses the thorax in such a manner that the wings travel through their full range of motion. This technique allows for testing of the specimen with all natural boundary conditions intact. All other techniques used required the muscle fibers to be partially or fully removed for instrumentation and experimentation. Sources of error can arise from adhesion of the muscles to the stretch rod and not having exact exoskeleton material to adhere to.

Power Density Analysis

The absolute power of the dorsoventral and dorsolongitudinal muscles as presented was 13.3 and 31 mW. If the assumption is made that both muscles groups are of the same biological composition then the specific power density of the muscular tissue must be a single value. This would then require that the DVMs and DLMs have the same power density. In varying the weight percentage of both muscle groups it was shown in Figure 59 that the point where both are equal to each other is 112 W/kg at 70% DLM and 30%DVM of the total muscle mass. This being true, implies that the muscle mass ratio within the thorax is 70% DLM to 30% DVM.

Actuator Analysis

In looking to create an actuator wing combination the actuator needs to be light enough to lift and provide enough force to lift the vehicle. This combination of constraints makes creating an actuator wing combination difficult because typically power is directly proportional to the mass of the object or material in an increasing fashion. The work performed here has produced a baseline for what should be targeted for in design of an actuator and wing mechanism. With reference to the hawk moth, the specific power density of the vehicle itself is 2.5 mW/kg or 44 mW/1.8kg. This encompasses the actuator, wings, and power source for the *M.sexta*. This value would be a baseline for what to target for on the design of a FWMAV actuator, wing, and power source system. One actuator type in particular that is being researched heavily and has seen itself on FWMAV's is a piezoelectric actuator which can have energy densities as high as 400 W/kg. Harvard has been able to utilize these actuators to produce a flying fly yet the power source of the vehicle is tethered to the vehicle, therefore not complete free flight. The set back at the moment is in the development of power sources that are light and energy dense enough to be carried by FWMAVs.

Flapping Angle Data

The intent of this investigation was to determine if the entire flapping motion of *M.sexta* could be artificially induced by applying external forces to the thorax in the direction of the muscles (tergum and phragma). It was confirmed that actuation of the thoracic structure did in fact actuate the indirect flapping mechanics of the hawkmoth producing the upstroke via a vertical thoracic compression and the downstroke via a longitudinal thoracic compression.

Muscle Attachment Point Significance

It was observed through the many different arrays of testing that the actuation positions on the thorax are extremely critical to the absolute power results. If the vertical push rod actuated the thorax too far aft of the specimen the absolute power was roughly double what was reported in the results. Strong evidence shows the reasoning for this is that there is a loss of mechanical advantage when the tergum is actuated aft of the actual muscle attachment point. This indicates that the muscle attachment points and the physical geometry of the specimen creates a kinematic system utilizing flexible joints and membranes in order to achieve the mechanical advantage necessary to flap the wings with minimal energy usage.

Elastic storage of inertial energy

Through high speed video observations and load data correlation, there is evidence that there exists elastic storage of inertial energy. This is particularly evident during the with-wings testing. When the thorax is loaded and unloaded its skeletal structure reacts like a spring within the system with the ability to store and release energy. The storing of the energy is due the contraction of the spring-like structure of the thorax. Through video observation, it was seen that the wings moved though intermediary positions of the wing stroke even though there was no movement of the thorax due to compression. With every stroke, the compression for the vertical direction would take approximately 10 ms and the longitudinal direction was approximately 5 ms, the moth flaps at approximately 25 Hz meaning 40 ms per flap, if the muscle actuation is only for 15 ms out of the 40 ms and wing displacement is occurring over the 40 ms then there is work being done by the structure on the wings which is due to the elastic inertial stored energy.

Passive Pitching and Rotation

Wing pitching is an extremely important aspect for flight of most insects because it is one of the major reasons why insects can actually fly. The pitching upward of the wing allows for lower drag force during the upstroke as well as developing vortices which assist in the overall lift and thrust generation. A major point of debate is whether the pitching is passively or physically controlled by the specimen. For past studies it was impossible to reproduce the flapping motion of the specimen without interaction with the muscles themselves. The experiment presented is the first of its kind to offer a solution to that problem. The reproduction of the flapping motion was produced utilizing no direct muscle activation, in other words the specimen were reanimated producing the natural flapping stoke with no electrical stimuli. Wing pitching and rotation was clearly observed utilizing the high speed camera imagery. The wings at the bottom of the downstroke were observed to pitch up for the upstroke and rotate/pitch forward for the thrust/lift producing downstroke.

Wings vs. No-Wings

During experimentation it was determined after many days of video observation and force data comparison, that the wings aerodynamic and inertial forces were affecting the force data acquired for actuating the thorax. The effect producing a dampening effect on the force data acquired. Therefore, a test was run where a moth was tested with wings on and wings off without disturbing the position of the moth and the power results were near identical. Acquiring force data for the with-wings case that appeared as if the wings forces were not prevalent in the signal data was rather exhausting. It required many positional adjustments and quick analysis of the images and forces to determine if there was interaction at play. If the two cases could be confirmed to have nearly equal results then testing could be carried out with removal of the wings. Removal of the wings allows for a simpler testing procedure and overall easier data acquisition and analysis. Taking a step back now and further analyzing the actual basic principles to how flight is achieved within the hawkmoth it is known that the moth operates under an indirect flight mechanism. Meaning that the actuation of the wings is not directly affected by the flight muscles themselves however a combination of the muscles and thoracic structure do. As known the muscles perform work to deform the structure of the thorax which yields a wing deflection as an outcome. It is therefore proposed that the majority of the power required to flap the wings is devoted to the deformation of the thoracic structure itself. Only until recently has this thought become more concrete. Work performed at AFIT under PhD Ryan O'Hara showed that the power required for the downstroke to be approximately 3 mW of power for the biological wing utilizing his designed and constructed piezoelectric flapper. This implies that the power required for the wings to produce sufficient lift for flight is approximately 10% of the power required to deform the thoracic structure to yield the same flapping stroke. Since the power required by the wings is small with respect to that of the structure actuation, a nearly exact approximate for the power necessary to achieve flight of the muscles can be extracted from a thoracic study alone.

Muscle contraction and relaxation timing

During the experimental testing and force/displacement data observations it was found that the time of muscle contraction was 15.7 ms and the time of relaxation was 20 ms. This relationship is shown in Figure 61. This shows that the mechanism produced a 43 % on cycle and a 57 % off cycle for the contraction and relaxation respectively.

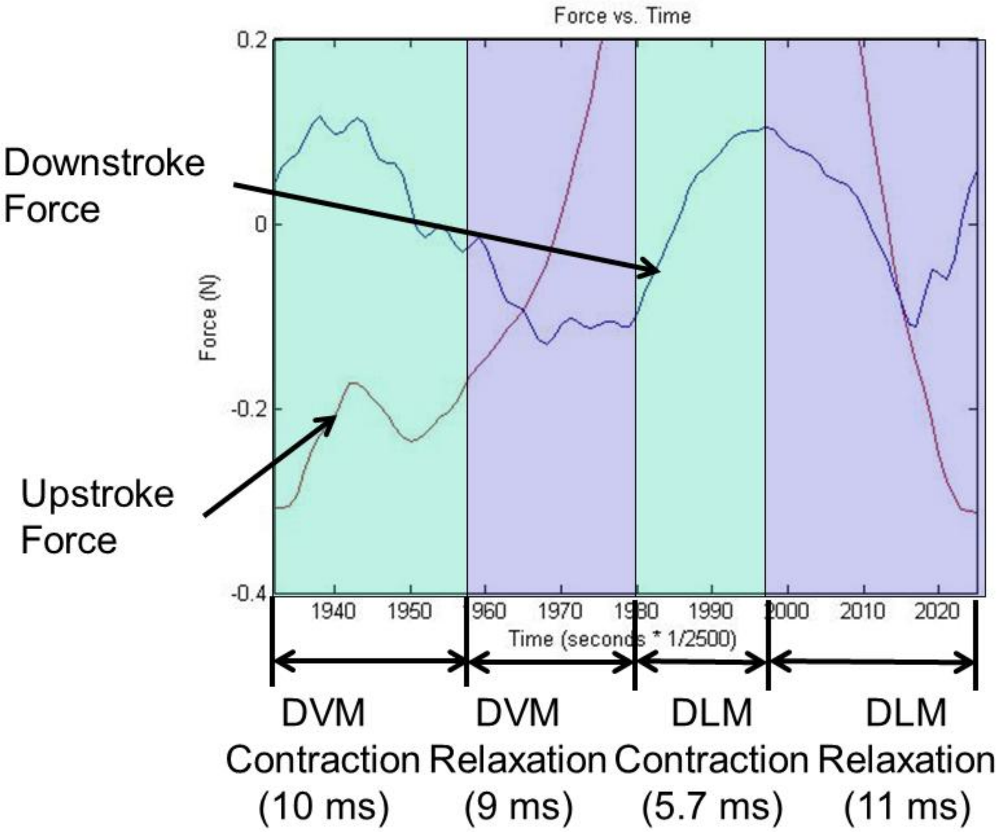

Figure 61: Contraction and Relaxation timing of the DVM and DLM muscles during a single flap.

APPENDIX

Appendix A. Raising Hawkmoths

The AFIT FWMAV research group receives hawkmoth pupae on a regular basis from Dr. Mark Willis at Case Western University. Dr. Willis' lab contains of a thriving colony of *Manduca Sexta*, which produces scores of moths each week. The most challenging part of raising the hawkmoths, hatching the eggs and feeding the caterpillars, is already complete when we receive the pupae in the mail (refer to (Reinecke, Buckner and Grugel 1980) for an excellent exposition on the full life cycle). All they need are a proper light cycle and the right temperature in order to eclose (hatch into adulthood). Figure 62 shows a hawkmoth pupa. The specimen is on its back with the head pointed toward the left. The right forewing can be seen wrapped around midsection of the body. The abdomen with its many segments and spiracles, points to the right. The "handle" object protruding from the head is the proboscis, folded several times. When extended, the proboscis of the adult *M.sexta* can be as long as it's body, and is used for feeding on flower nectar while hovering.

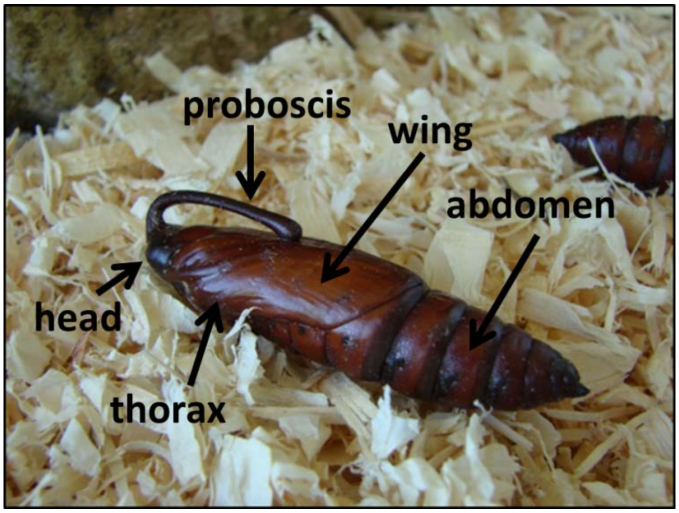

Figure 62 - Typical *M.sexta* pupa. The wings are small and wrapped around the thorax and upper abdomen. In the wild, these pupa use the segmented abdomen to burrow under soil or leaves for protection from the elements until it is time to eclose.

APPENDIX

A.1. The Enclosure

A 1x1x1 foot cubic terrarium holds the pupae prior to eclosion. The bottom of the terrarium is lined with approximately 1 inch of wood shavings beneath a layer of paper towels. This, along with frequent cleaning, is necessary because with each moth's eclosion comes a release of large quantities of waste (*meconium*) which is the by-product of the transformation from caterpillar to moth (Reinecke, Buckner and Grugel 1980). The front of the terrarium has doors which can swing open for access from the front and the entire top glass pane can be removed for access from the top. The most important feature is the back wall made of textured foam. This wall gives the freshly eclosed moth a surface to climb up, which is an absolute necessity. The moth must climb off of the ground in order to pump fluids through the veins in its wings to stretch them out before they harden. Typically, the moth finds a position on the wall in about 10 minutes and has fully inflated its wings 20 minutes later. Figure 63 shows two young adult hawkmoths which hatched only a few minutes apart.

APPENDIX

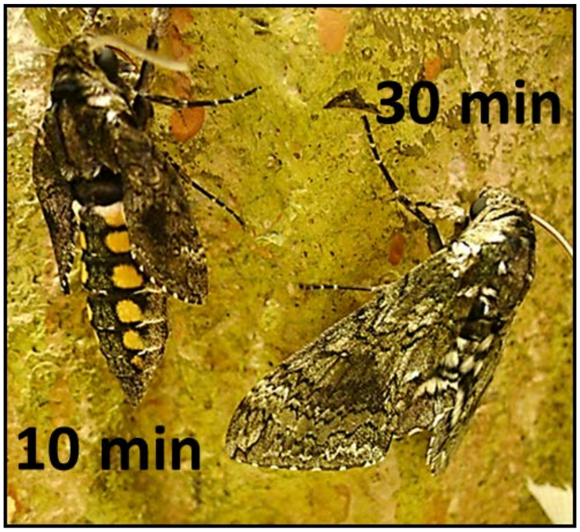

Figure 63 - Two freshly-eclosed *M.sexta* specimens. One is only 10 minutes old and has not inflated its wings.

A.2. Light Cycle and Environment

M.sexta thrives in the warm temperatures of the southern North American summer. The pupae prefer a summertime light cycle of long days and short nights, as well as warm summertime temperatures. The light cycle for the AFIT moths has been set to 14 hours of light and 10 hours of darkness (Willis 2011). The light cycle is accomplished using a standard outlet timer wired to a string of LED lights secured around the inner walls of a cardboard box (Figure 64). The terrarium with the pupae is placed within this box and the lid is then closed, allowing no light from the outside. The temperature of the vivarium is set to 80 degrees Fahrenheit and the humidity is kept at 40 percent in order to replicate summertime conditions.

APPENDIX

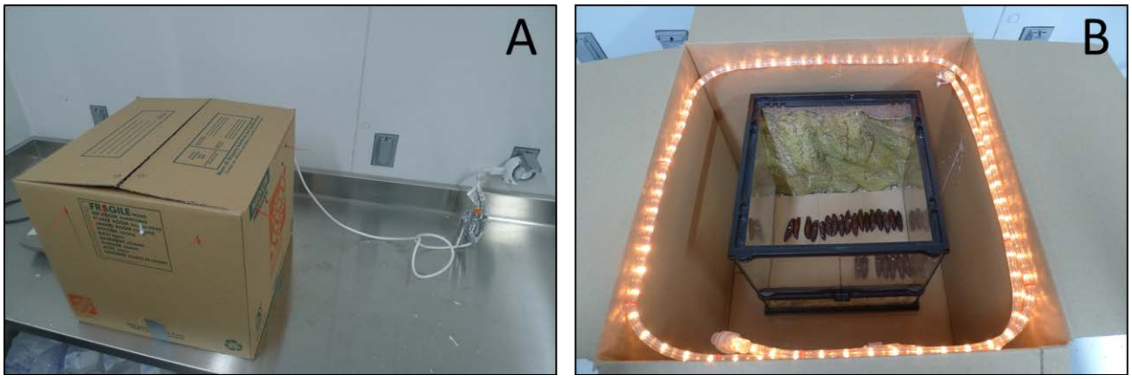

Figure 64 - Enclosure for the pupae: **(A)** Closed box creates day/night conditions with a timer controlling the LED lights, shown in part **(B)**

A.3. Eclosion

The terrarium is checked daily for newly emerged adult moths. They tend to eclose at “dusk,” or shortly after their light cycle switches from light to dark. Since the cardboard box enclosure around the terrarium allows this light cycle to be set for any time of day, the light-to-dark transition has been set to occur mid-afternoon. That way, the moths will eclose in the afternoon and the terrarium can be checked for adults when heading home for the day. When an adult moth is found in the pupa terrarium during daily inspections, it is transferred to a mesh cage which is constantly open to the light of the vivarium (Figure 65). *M.sexta* is a nocturnal specimens, and as such is inactive during daylight. The adults are therefore docile and essentially dormant as long as the lights are kept on. If the lights are switched off, however, the adults will fly for hours against the walls of the enclosure and damage their wings. This is to be avoided because much of the research that goes on among the AFIT FWMAV research group requires intact forewings.

APPENDIX

Figure 65 - Adult enclosure: (C) Moths sit dormant on the mesh wall, (B) Lid closed, light can pass through. The cage sits inside a cardboard box lined with paper bags to facilitate cleaning. Adults often emit meconium hours or even days after eclosion.

A.4. Preparation for Experimentation

When an adult *M.sexta* is required for an experiment it is removed from the vivarium and placed in a container. Paper towels soaked with acetone are then added to the container. The acetone vapor asphyxiates the moth within 1 hour. Additionally, the integrity of the wings is of utmost importance, the container is also placed into the refrigerator. The cold air immobilizes the moth but will not cause tissue damage. Immobilizing the moth with refrigeration helps prevent excessive flapping inside the container which could damage the wings. The container is then removed from the refrigerator. An alternative option is to place the specimen in a freezer for more than 45 minutes. This is long enough to kill the specimen without crystallizing most of the liquid in the muscles. This method was only used for dissection specimens, as it was deemed too harsh on the material properties of the cuticle and muscles for the purposes of the experiments.

APPENDIX

A.5. Removal of Scales

Scales cover nearly the entire body of the adult moth. The wings and abdomen are covered with a thin layer of scales that tends to stay on the moth unless purposefully brushed away. The scales on the thorax, however, are very densely packed and easily become airborne when a specimen is handled. It is therefore necessary to remove the scales from the thorax before beginning experimentation. The scales can be brushed off under running water either with a toothbrush or by hand. Moving water carries the scales away and prevents them from becoming airborne, which could be an eye irritant.

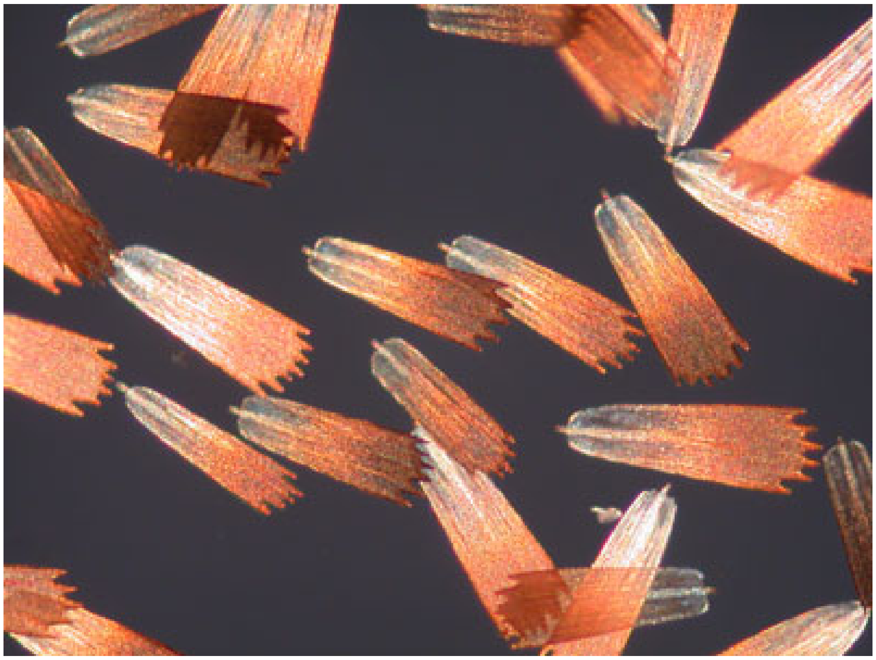

Figure 66 – 200x Magnified image of moth scales **(Jenikova 2005)**

APPENDIX

The following Appendices B-F details all of the Matlab code in full that was used for the data acquisition and data analysis of the experiment.

APPENDIX

Appendix B. Signal and Load Code for Dynamic Experiment

```
clc,clear,close all
%% Set the Sampling Options
SampleSeconds = 1; % Time in Seconds
SampleRate    = 2500; % Hz
SampleNumber = SampleRate * SampleSeconds; % Total Samples
SampleTime = linspace(0,SampleSeconds,SampleNumber); %Time Vector

%% Calculate the output signal based on the SampleNumber of the data
g = 2;   % Gain (amplitude of sine wave)
bias=-1.8;  % Bias for the shaker sine wave signal (neg. bias for pos.
movement)
OmegaDeg = 25;                  % Frequency in Hz
OmegaRad = OmegaDeg*2*pi;       % Frequency in Radians

% Output 1 - Camera Trigger
data1 = 5 * ones(1,SampleNumber)';
data1(end)=0;

% Output 2 - Shaker Signal
data2=0*ones(1,SampleNumber)';  % Establish a SampleNumber:1 matrix to
fill
t=200;  % Number of samples used to tare the load cell before shaker
starts
data2(1:t) = 0*ones(1,t);  % Signal is zero for duration of "t"
data2(t+1:SampleNumber) =
sin(linspace(0,OmegaRad*SampleSeconds,SampleNumber-t))'; % Sinusoidal
signal
data2 = g * data2;     % Apply Amplitude (gain)
data2 = data2 + bias;  % Apply Bias to sine wave
data2(1:t) = 0*ones(1,t);  % after bias so tare will still be at zero
data2(end)=0;
%% Check sine wave signal, only necessary for setting up test runs
%figure
%plot(data2);
%% Get NI USB-6251 Data
NI = daqhwinfo('nidaq');

%% Create Device object
ao = analogoutput('nidaq',NI.InstalledBoardIds{1});
ai = analoginput('nidaq',NI.InstalledBoardIds{1});

%% Set Channels
chans_ao = addchannel(ao,0:1); % Analog Out Channel 0 & 1
chans_ai = addchannel(ai,0:1); % Analog In  Channel 0

%% Set AO Sample Options
ao.SampleRate = SampleRate;

%% Set AI Sample Options
```

```
ai.SampleRate = SampleRate;
ai.TriggerRepeat = 0;
ai.SamplesPerTrigger = SampleNumber;

%% Obtain the actual rate set in case hardware limitations
ActualRate = get(ao,'SampleRate');

%% Set TriggerType to Manual for fastest triggering
set([ai ao],'TriggerType','Manual')

%% Queue the output on 2 channels
putdata(ao,[data1 data2]);

%% Start and Trigger the Output
start([ai ao]);   % Start Analog Output
trigger([ai ao]); % Start Analog Input

%% Capture Analog Input Data from the buffer
data_ai = getdata(ai);

%% Clean and Remove ai & ao from memory
delete(ai)
delete(ao)

%% Convert voltage signal to grams and grams to Newtons for channel 0
tare1=sum(data_ai(1:t,1)/t); % gets average voltage signal from tare
period
slope1 = 0.0119; % grams/volt slope of the load cell as calibrated
force1 = -84.033*data_ai(:,1) + tare1/slope1; % Determines equivalent
mass in grams
forceN1 = force1/101.971; % Convert mass (grams) to Newtons

%% Convert voltage signal to grams and grams to Newtons for channel 1
tare2=sum(data_ai(1:t,2)/t); % gets average voltage signal from tare
period
slope2 = 0.0123; % grams/volt slope of the load cell as calibrated
force2 = -81.300*data_ai(:,2) + tare2/slope2; % Determines equivalent
mass in grams
forceN2 = force2/101.971; % Convert mass (grams) to Newtons

%% Make figures of force vs time for channel 0
figure
plot (1:SampleNumber,forceN1)
title('Longitudinal Force vs. Time with tare')
xlabel('Time (seconds * 1/2500)')
ylabel('Force (N)')
%% Make figures of force vs time for channel 1
figure
plot (1:SampleNumber,forceN2)
title('Vertical Force vs. Time with tare')
xlabel('Time (seconds * 1/2500)')
ylabel('Force (N)')
```

APPENDIX

Appendix C. Video Proc. and Tracking for Dynamic Experiment

```
%% Modified to select triangle and square and log excessive shifts in x
and y
clc,clear all ,close all

%% Get .tif files
Files=dir('*.tif');
NumPoints=input('How many points are you tracking?\n');
NumFrames=input('How many frames are you using?\n');

l=1;
k=1;
n=2;
m=1;
while m<=NumFrames-1;

    I(1).I = imread(Files(m).name);
    I(2).I = imread(Files(m+1).name);
    for p=1:NumPoints
        if m == 1

            fprintf('Select point %d.\n',p);
            [I(1).Point(p).Sub,I(1).Point(p).SubRect] = imcrop(I(1).I);
% Choose the Subimage of square from I1
            [I(2).Point(p).Sub,I(2).Point(p).SubRect] =
imcrop(I(2).I,I(1).Point(p).SubRect);    % Choose the Subimage from I2
            if p==NumPoints
                fprintf('Go play pinball or minesweeper on the
nanoindenter computer.\n');
            end
        end
        if m>3
            checks =(abs(Point(p).x(m-1)-Point(p).x(m-2))>10);
            if checks == 1
                fprintf('Select the %d.\n',p);
                [I(1).Point(p).Sub,I(1).Point(p).SubRect] =
imcrop(I(1).I);                  % Choose the Subimage of square from I1
                [I(2).Point(p).Sub,I(2).Point(p).SubRect] =
imcrop(I(2).I,I(1).Point(p).SubRect);   % Choose the Subimage from I2
                fprintf('Go back to your coffee.\n');
                m=m-1;
            end
        end
        % Compute Normalized Xcorr2 Sub-Image 1 to Image 2
        c = normxcorr2(I(n-1).Point(p).Sub,I(n).I);
        %figure, surf(I(n).c(:,:,1)), shading flat
        [MaxC,Imax] = max(abs(c(:)));
        [y_peak, x_peak] = ind2sub(size(c),Imax);
        corr_offset_xs = x_peak-size(I(n-1).Point(p).Sub,2);
        corr_offset_ys = y_peak-size(I(n-1).Point(p).Sub,1);
        Point(p).x(m) = corr_offset_xs+I(n-1).Point(p).SubRect(3)/2;
        Point(p).y(m) = corr_offset_ys+I(n-1).Point(p).SubRect(4)/2;
```

```
        fprintf('Process Frame %d of %d\n',[m NumFrames-1])
    end
    m=m+1;
end

%% Make Avi of Tracking progress
% Create Video Object
vidObj = VideoWriter('Moth 3.avi');

% Set and view the frame rate.
vidObj.FrameRate = 30;

% Open Video Object
open(vidObj);
figure
for m=2:NumFrames-1
    imshow(imread(Files(m).name))
    hold on
    for p=1:NumPoints
        plot(Point(p).x(m),Point(p).y(m),'r+')
    end
    hold off
    currFrame = getframe;
    writeVideo(vidObj,currFrame);
end

% Close the file.
close(vidObj);

%% plot the vertical displacement
Disp = [1:length(Point.y)]'*0;
Disp(:) = Point(1).y(:);
figure
%plot((1:NumFrames)/2500,atand(abs((Point(1).y(:)-
Point(3).y(:))/(Point(1).x(:)-Point(3).x(:)))),'r');
% ^^ can be used to calculate wing angles, just click where you would
for the static test
conv=5.8; % pixels per mm
plot(1:NumFrames-1,(Disp(:)/-conv)+abs((Disp(100)/conv)))
title('Vertical Displacement')
xlabel('frame # or time (sec/2500)')
ylabel('Vertical displacement (mm)')

%% plot the horizontal displacement of linkage
cl = 9; %crank length
sl = 8; %shaft length
vertdisp = (Disp(:)/-conv)+abs((Disp(100)/conv));
linkang = 18*(pi/180); %initial linkage back angle
vertbias = cl-(cl*cos(linkang))+sl-sqrt(sl^2-(cl*sin(linkang))^2);
newvertdisp = vertbias+vertdisp;
figure
plot(newvertdisp);
angle = [1:length(Point.y)]'*0;
```

```
for i = 1:length(Point.y)
    angle(i) = acos((2*cl^2+2*cl*sl-2*cl*newvertdisp(i)-
2*sl*newvertdisp(i)...
        +newvertdisp(i).^2)/(2*cl*(cl+sl-newvertdisp(i))));
end

horzbias = cl*sin(linkang);
horzdisp = cl*sin(angle);
newhorzdisp = horzdisp-horzbias;

figure
plot(angle*(180/pi));
title('Angular Rotation of Crank')
xlabel('frame # or time (sec/2500)')
ylabel('Angle (deg)')

figure
plot(newhorzdisp);
title('Longitudinal Displacement')
xlabel('frame # or time (sec/2500)')
ylabel('Longitudinal displacement (mm)')

figure
plot(vertdisp)
title('Vertical Displacement')
xlabel('frame # or time (sec/2500)')
ylabel('Vertical displacement (mm)')
```

APPENDIX

Appendix D. Point 1 and Point 2 Location Finder Code (Vertical and Longitudinal)

Vertical Power P1 array locator

```
clc;
clear I;
c = 273; %iniital point left end of scan range
d = 285; %initial point right end of scan range
I = 0;
i = 1;
p1_array = zeros(24,1); %initialize the p2 array
while I < 2480 %scans the whole data set
    [p1,I] = min(y(c:d)); %finding the minimum force and idicie over a
period
    I = I + c; %rescaling indice valve for 1:2500 scale
    c = I+80; %period of negative amplitude peak to peak minus 10
frames added to previous minima location
    d = I+95; %the period value plus 5-10 frames, this establishes the
range to be scanned for the next flap
    p1_array(i,1) = I-1; %writing the current value of p1 to the array
    i = i+1;
end
```

Vertical Power P2 array locator

```
clc;
clear I;
c = 295;
d = 310;
I = 0;
i = 1;
p2_array = zeros(24,1); %initialize the p2 array
while I < 2480
    [p2,I] = max(y2(c:d)); %finding the maximum displacement and idicie
over a period
    I = I + c; %rescaling indice valve for 1:2500 scale
    c = I+85; %period of positive amplitude peak to peak minus 10
frames added to previous maximum location
    d = I+95; %the period value plus 5-10 frames, this establishes the
range to be scanned for the next flap
    p2_array(i,1) = I-1; %writing the current value of p2 to the array
    i = i+1;
end
```

Longitudinal Power P1 array locator

```
clc;
clear I;
c = 320;
d = 328;
I = 0;
i = 1;
```

```
p1_array_horz = zeros(24,1); %initialize the p1 array
while I < 2400
    [p1,I] = min(abs(y4(c:d))); %finding the starting value
displacement and idicie over a period
    I = I + c; %rescaling indice valve for 1:2500 scale
    c = I+88; %period of negative peak to peak
    d = I+98; %moves value off of previous minima
    p1_array_horz(i,1) = I-1; %writing the current value of p1 to the
array
    i = i+1;
end
```

Longitudinal Power P2 array locator

```
clc;
clear I;
c = 330;
d = 345;
I = 0;
i = 1;
p2_array_horz = zeros(24,1); %initialize the p2 array
while I < 2400
    [p2,I] = min(y4(c:d)); %finding the maximum displacement and idicie
over a period
    I = I + c -1; %rescaling indice value for 1:2500 scale
    c = I+85; %moves value off of previous peak
    d = I+95'; %period of peak to peak
    p2_array_horz(i,1) = I; %writing the current value of p2 to the
array
    i = i+1;
end
```

APPENDIX

Appendix E. Power Calculation Code for Dynamic Experiment (Vertical and Longitudinal)

Vertical Power Computation

```
%% Before running this code, load the workspaces for the force and
tracking data and data for p1 and p2 array
num = 24;
power_array = zeros(num,1);
work_array = zeros(num,1);
disp_array = zeros(num,1);
time_array = zeros(num,1);
force_array = zeros(num,1);
%% Create an array of displacement values over the desired range of
time
for j = 1:num
    clear D
    clear disp
    conv=5.8; % pixels per mm
    p1 = p1_array(j,1);
    p2 = p2_array(j,1);
    Disp = y2(:);
    disp(1:p2-p1)=(1:p2-p1)'*0;
    for i=2:p2-p1+1;
        disp(i) = disp(i-1) + (Disp(p2)-Disp(p1))/(p2-p1)/(1000);
    end
    D = disp'; % simplify name and invert the matrix
    %% Plot the force over distance
    F = y + abs (min(y(p1:p2))); % adjusts the force so the smallest
value is set to zero
    %figure
    plot (D,F(p1:p2))
    xlabel ('Distance (m)')
    ylabel ('Force (N)')
    title ('Force over Distance for a Single Upstroke')
    F2 = F(p2)-F(p1);
    force_array(j,1) = F2;

    %% present the total displacement in mm
    displacement = (D(end)-D(1))*1000;
    disp_array(j,1) = displacement;

    %% Integrate over this region to get the work
    Work = trapz (D,F(p1:p2)); % this is the total work or energy in
Joules
    work_array(j,1) = Work;
```

```
    %% Divide work by total time interval during application of the
force
    time=(p2-p1)/2500; % The time interval in seconds during which the
force is imparted
    time_array(j,1) = time;
    Power = Work / time; % This is what we're after!!!
    power_array(j,1) = Power;
end
power_average = mean(power_array)
work_average = mean(work_array)
disp_average = mean(disp_array)
time_average = mean(time_array)
force_average = mean(force_array)

blah = ones(1,num)*mean(power_array(3:24));
figure; plot(power_array,'o'); hold on; plot(blah,'r--')
xlabel ('Flap Number, (#)')
ylabel ('Power, (W)')
title ('Power per Flap')
```

Longitudinal Power Computation

```
%% Before running this code, load the workspaces for the force and
tracking data and p1,p2 horz arrays
power_array_horz = zeros(24,1);
work_array_horz = zeros(24,1);
disp_array_horz = zeros(24,1);
time_array_horz = zeros(24,1);
force_array_horz = zeros(24,1);
%% Create an array of displacement values over the desired range of
time
for j = 1:24
    clear D
    clear disp
    clear Disp
    conv=5.8; % pixels per mm
    p1 = p1_array_horz(j,1);
    p2 = p2_array_horz(j,1);
    Disp = y4(:);
    disp(1:p2-p1)=[1:p2-p1]'*0;
    for i=2:p2-p1+1;
        disp(i) = disp(i-1) + (Disp(p2)-Disp(p1))/(p2-p1)/(-1*1000);
    end
    D = disp'; % simplify name and invert the matrix

    %% Plot the force over distance
    F = y3 + abs (min(y3(p1:p2))); % adjusts the force so the smallest
value is set to zero
    %figure
    plot (D,F(p1:p2))
    xlabel ('Distance (m)')
```

```
    ylabel ('Force (N)')
    title ('Force over Distance for a Single Downstroke')
    F1 = F(p2)-F(p1);
    force_array_horz(j,1) = F1;

    %% present the total displacement in mm
    displacement = (D(end)-D(1))*1000;
    disp_array_horz(j,1) = displacement;

    %% Integrate over this region to get the work
    Work = trapz (D,F(p1:p2)); % this is the total work or energy in
Joules
    work_array_horz(j,1) = Work;

    %% Divide work by total time interval during application of the
force
    time=(p2-p1)/2500; % The time interval in seconds during which the
force is imparted
    time_array_horz(j,1) = time;
    Power = Work / time; % This is what we're after!!!
    power_array_horz(j,1) = Power;
end
power_average_horz = mean(power_array_horz)
work_average_horz = mean(work_array_horz)
disp_average_horz = mean(disp_array_horz)
time_average_horz = mean(time_array_horz)
force_average_horz = mean(force_array_horz)
% figure
% plot (power_array_horz,'o')
% xlabel ('Flap Number (#)')
% ylabel ('Power (W)')
% title ('Power per Flap')
blah2 = ones(1,num)*mean(power_array_horz(6:24));
figure; plot(power_array_horz,'o'); hold on; plot(blah2,'r--')
xlabel ('Flap Number, (#)')
ylabel ('Power, (W)')
title ('Power per Flap')
```

APPENDIX

Appendix F. 2nd Order Low-Pass Filter Code

```
clear conv
wm = 30*pi/180; %cutoff frequency
test = tf(wm^2,conv([1 wm],[1 wm]));
% figure;
% bode(test)
% grid on

dTest2 = c2d(test,1);
y = filter(dTest2.num{1},dTest2.den{1},forceN2);
figure;
plot(y)
title('Vertical Force vs. Time with tare')
xlabel('Time (seconds * 1/2500)')
ylabel('Force (N)')
%  hold on
%  plot(forceN2,'r')


y2 = filter(dTest2.num{1},dTest2.den{1},vertdisp);
figure;
plot(y2)
title('Vertical Displacement vs. Time with tare')
xlabel('Time (seconds * 1/2500)')
ylabel('Displacement (mm)')
% % hold on
% % plot(vertdisp,'r')

wm = 30*pi/180; %cutoff frequency
test = tf(wm^2,conv([1 wm],[1 wm]));

y3 = filter(dTest2.num{1},dTest2.den{1},forceN1);
figure;
plot(y3)
title('Longitudinal Force vs. Time with tare')
xlabel('Time (seconds * 1/2500)')
ylabel('Force (N)')
% hold on
% plot(forceN1,'r')

y4 = filter(dTest2.num{1},dTest2.den{1},newhorzdisp);
figure;
plot(y4)
title('Longitudinal Displacement vs. Time with tare')
xlabel('Time (seconds * 1/2500)')
ylabel('Displacement (mm)')
% % hold on
```

```
% % plot(newhorzdisp,'r')
```

APPENDIX

Appendix G. Instrumentation and Equipment Used

Bruel & Kjaer Small Vibration Exciter Type 4810

Figure 67: Bruel & Kjaer Small Vibration Exciter

Max displacement 6 mm

Max force 10 N or 7 N pending on the frequency

Force rating 10 newton (2.25 lbf) sine peak

Frequency range DC to 18 kHz

First axial resonance above 18 kHz

Maximum bare table acceleration 550 m/s2

Rugged construction

Optimised to obtain full output force when used with Power Amplifier Type 2718

National Instruments USB-6251 BNC Data Acquisition Device

Figure 68: NI USB-6251 BNC DAQ

8 differential BNC analog inputs (16-bit), 1.25 MS/s single-channel (1 MS/s aggregate)

2 BNC analog ouputs (16-bit, 2.8 MS/s); 24 digital I/O (8 clocked, 8 BNC); 32-bit counters

Use mass termination version with SCC signal conditioning

NI Signal Streaming for bidirectional high-speed data streams over USB; OEM version available

Compatible with LabVIEW, ANSI C/C++, C#, Visual Basic .NET and Visual Basic 6.0

APPENDIX

NI-DAQmx driver software and NI LabVIEW SignalExpress LE interactive data-logging software

Dantec Dynamics NanoSense MkII high-speed

512x512 pixel at 5140 fps

MK II goes up to 140.000 fps at reduced resolution

Shutter time: 1000 ns – 30 ms

USB2 interface

Sensor chip CMOS 512x512 pixel, 10 bit+

Figure 69: Dantec Dynamics NanoSense MkII

3 kg Cantilever Beam Load Cell

Figure 70: 3kg Cantilever beam load cell

APPENDIX

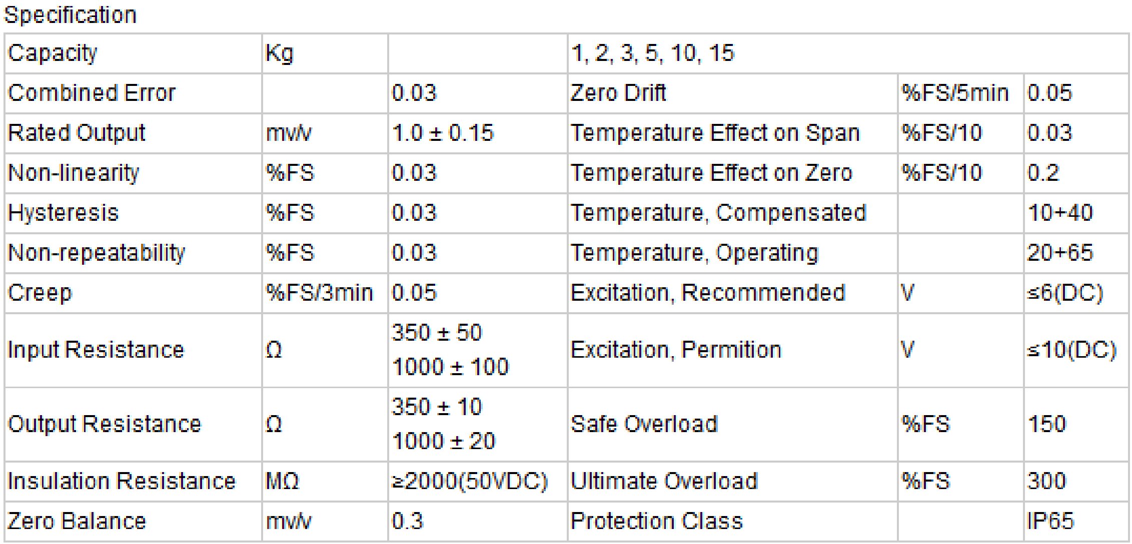

Specification

Capacity	Kg		1, 2, 3, 5, 10, 15		
Combined Error		0.03	Zero Drift	%FS/5min	0.05
Rated Output	mv/v	1.0 ± 0.15	Temperature Effect on Span	%FS/10	0.03
Non-linearity	%FS	0.03	Temperature Effect on Zero	%FS/10	0.2
Hysteresis	%FS	0.03	Temperature, Compensated		10+40
Non-repeatability	%FS	0.03	Temperature, Operating		20+65
Creep	%FS/3min	0.05	Excitation, Recommended	V	≤6(DC)
Input Resistance	Ω	350 ± 50 1000 ± 100	Excitation, Permition	V	≤10(DC)
Output Resistance	Ω	350 ± 10 1000 ± 20	Safe Overload	%FS	150
Insulation Resistance	MΩ	≥2000(50VDC)	Ultimate Overload	%FS	300
Zero Balance	mv/v	0.3	Protection Class		IP65

Figure 71: Load Cell Specifications

Objet Eden500V™ 3-dimensional printer

Figure 72: Object Eden500V

APPENDIX

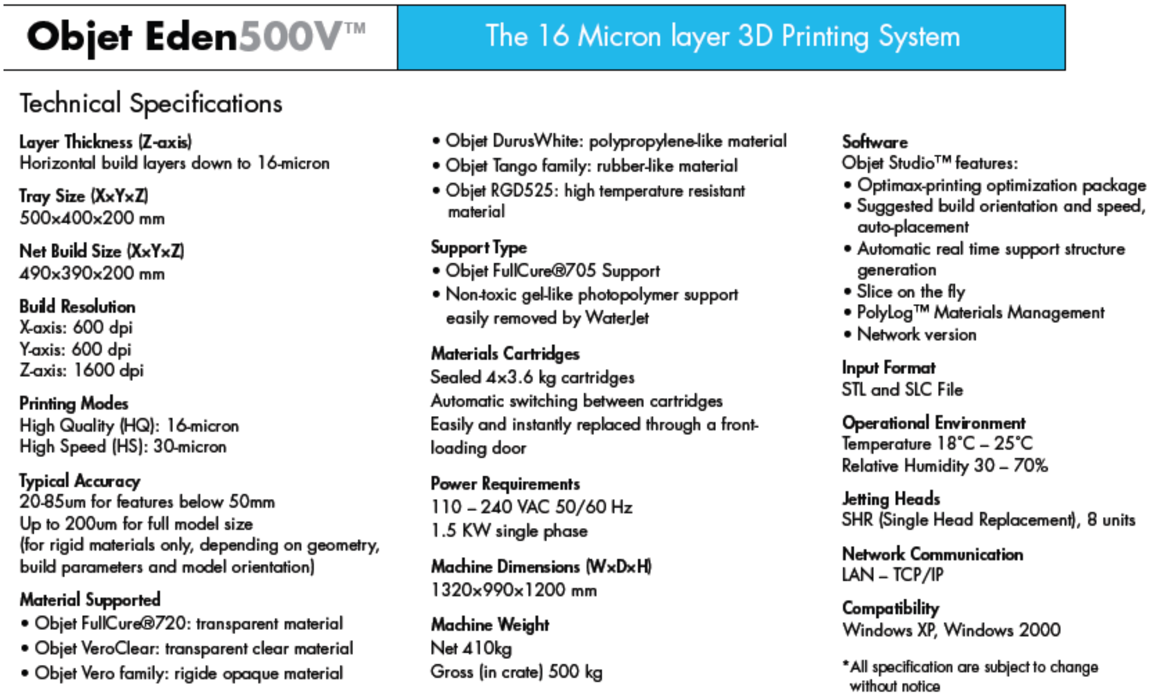

Objet Eden500V™ The 16 Micron layer 3D Printing System

Technical Specifications

Layer Thickness (Z-axis)
Horizontal build layers down to 16-micron

Tray Size (XxYxZ)
500x400x200 mm

Net Build Size (XxYxZ)
490x390x200 mm

Build Resolution
X-axis: 600 dpi
Y-axis: 600 dpi
Z-axis: 1600 dpi

Printing Modes
High Quality (HQ): 16-micron
High Speed (HS): 30-micron

Typical Accuracy
20-85um for features below 50mm
Up to 200um for full model size
(for rigid materials only, depending on geometry, build parameters and model orientation)

Material Supported
- Objet FullCure®720: transparent material
- Objet VeroClear: transparent clear material
- Objet Vero family: rigide opaque material
- Objet DurusWhite: polypropylene-like material
- Objet Tango family: rubber-like material
- Objet RGD525: high temperature resistant material

Support Type
- Objet FullCure®705 Support
- Non-toxic gel-like photopolymer support easily removed by WaterJet

Materials Cartridges
Sealed 4x3.6 kg cartridges
Automatic switching between cartridges
Easily and instantly replaced through a front-loading door

Power Requirements
110 – 240 VAC 50/60 Hz
1.5 KW single phase

Machine Dimensions (WxDxH)
1320x990x1200 mm

Machine Weight
Net 410kg
Gross (in crate) 500 kg

Software
Objet Studio™ features:
- Optimax-printing optimization package
- Suggested build orientation and speed, auto-placement
- Automatic real time support structure generation
- Slice on the fly
- PolyLog™ Materials Management
- Network version

Input Format
STL and SLC File

Operational Environment
Temperature 18°C – 25°C
Relative Humidity 30 – 70%

Jetting Heads
SHR (Single Head Replacement), 8 units

Network Communication
LAN – TCP/IP

Compatibility
Windows XP, Windows 2000

*All specification are subject to change without notice

Figure 73: Object Eden500V Specfications

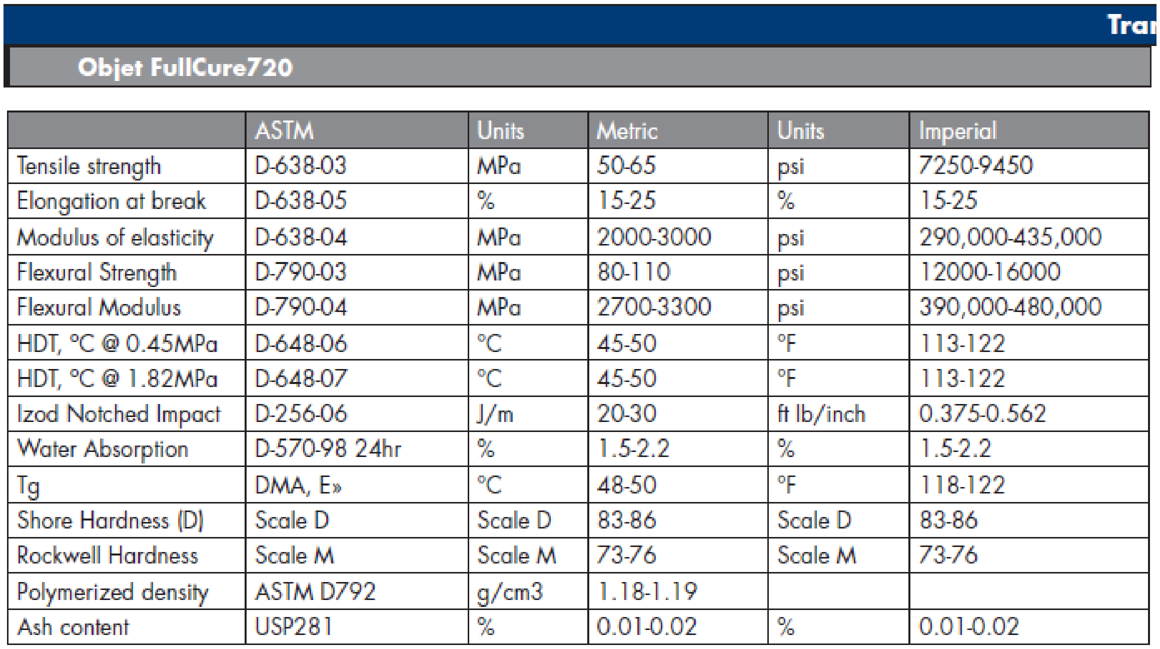

Tra

Objet FullCure720

	ASTM	Units	Metric	Units	Imperial
Tensile strength	D-638-03	MPa	50-65	psi	7250-9450
Elongation at break	D-638-05	%	15-25	%	15-25
Modulus of elasticity	D-638-04	MPa	2000-3000	psi	290,000-435,000
Flexural Strength	D-790-03	MPa	80-110	psi	12000-16000
Flexural Modulus	D-790-04	MPa	2700-3300	psi	390,000-480,000
HDT, °C @ 0.45MPa	D-648-06	°C	45-50	°F	113-122
HDT, °C @ 1.82MPa	D-648-07	°C	45-50	°F	113-122
Izod Notched Impact	D-256-06	J/m	20-30	ft lb/inch	0.375-0.562
Water Absorption	D-570-98 24hr	%	1.5-2.2	%	1.5-2.2
Tg	DMA, E»	°C	48-50	°F	118-122
Shore Hardness (D)	Scale D	Scale D	83-86	Scale D	83-86
Rockwell Hardness	Scale M	Scale M	73-76	Scale M	73-76
Polymerized density	ASTM D792	g/cm3	1.18-1.19		
Ash content	USP281	%	0.01-0.02	%	0.01-0.02

Figure 74: Object Eden500V FullCure720 Material Data Sheet

Bibliography

AeroVironment. "DARPA Contract Goals." *AVinc.* 2009. http://www.avinc.com/downloads/NAVPRLongDARPAV4.doc.pdf (accessed 2012).

—. *Nano Hummingbird.* 2012. http://www.avinc.com/nano.

Ahn, Anna. "How muscles function- The work loop technique." *The Journal of Experimental Biology*, 2010: 1051-1052.

Alexander, D.E. *Nature's Flyers; Birds, Insects and the Biomechanics of Flight.* Baltimore: The Johns Hopkins University Press, 2002.

Ashley, Steven. "Palm-Size Spy Plane." *Mechanical Engineering, ASME.* February 1998. http://www.memagazine.org/backissues/membersonly/february98/palmsize/palmsize.html.

Bao, X.Q., A. Bontemps, T. Vanneste, J-B Paquet, S. Grondel, and E. Cattan. "Fabrication and Actuation of Flapping-Wing Robotic Insect Prototype using Selected Polymer." *Bionic Robots Workshop.* 2011. http://www.emn.fr/z-dre/bionic-robots-workshop/uploads/Abstracts%20BRW%202011/26.pdf (accessed 2012).

Barbakedze, N., S. Enders, S. Gorb, and E. Arzt. "Local Mechanical Properties of the Head Articulation Cuticle in the Beetle Panchnoda Marginata (Coleoptera, Scarabaeidae)." *Journal of Experimental Biology* 209, no. 4 (February 2006): 722-730.

Bayline, Ronald J., Carsten Duch, and Richard B. Levine. "Nerve–Muscle Interactions Regulate Motor Terminal Growth and Myoblast Distribution during Muscle Development." *Developmental Biology*, 2001: 348–363.

Bertrand, Tanner, Michael Regnier, and Thomas Daniel. "A spatially explicit model of muscle contraction explains a relationship between." *The Journal of Experimental Biology*, 2008: 180-186.

Bolsman, Caspar. *Flapping Wing Actuation Using Resonant Compliant Mechanisms.* PhD Dissertation, PhD Dissertation, Delft University of Technology, The Netherlands: Ipskamp, ISBN 9789090256856, 2010.

Bonsor, Kevin. *HowStuffWorks.com.* January 08, 2012. http://www.science.howstuffworks.com/spy-fly.htm (accessed 2012).

butterfliesandmoths.org. 2012. http://www.butterfliesandmoths.org (accessed January 2012).

Casey, T.M. "A Comparison of Mechanical and Energetic Estimates of Flight Cost for Hovering Sphinx Moths." *Journal of Experimental Biology* 91 (1981): 117-129.

Casey, T.M. "Flight Energetics of Sphinx Moths: Power Input During Hovering Flight." *Journal of Experimental Biology* 64 (1976): 529-543.

Chakravarty, U.K., and R. Albertani. "Energy Absorption Behavior of a Hyperelastic Membrane for Micro Air Vehicle Wings: Experimental and Finite Element Approaches." *International Journal of Micro Air Vehicles* 3, no. 1 (2011): 13-21.

Chapman, Reginald F. *The Insects, 4th edition.* Cambridge: University Press, 1998.

Combes, S.A., and T.L. Daniel. "Into Thin Air: Contributions of Aerodynamic and Inertial-Elastic Forces to Wing Bending in the Hawkmoth Manduca sexta." *Journal of Experimental Biology* 206 (2003): 2999-3006.

Cook, R.D., D.S. Malkus, M.E. Plesha, and R.J. Witt. *Concepts and Applications of Finite Element Analysis, 4th ed.* John Wiley and Sons, Inc., 2002.

Daniel, T.L., and S.A. Combes. "Flexing Wings and Fins: Bending by Inertial or Fluid-Dynamic Forces?" *International Computational Biology* 42 (2002): 1044-1049.

Daniel, T.L., and T.L. Hedrick. "Flight Control in the Hawkmoth Manduca sexta: The Inverse Problem of Hovering." *Journal of Experimental Biology* 209 (August 2006): 3114-3130.

Daniel, Thomas L., and Michael S. Tu. "Submaximal Power Output from the Dorsolongitudinal Flight Muscles of the Hawkmoth Manduca Sexta." *Journal of Experimental Biology* 207 (2004): 4651-4662.

Delft, TU. *Dossier DelFly*. 12 12, 2012. http://tudelft.nl/en/current/dossiers/archive/delfly/ (accessed 10 05, 2012).

Demasi, Luciano, Anthony Palazotto, and Alex Hollenbeck. "Structural Investigation of a MAV's Thorax." *53rd Structures, Structural Dynamics and Materials Conference (SDM).* Honolulu HI: AIAA, 2012.

Dickinson, M. "Mechanical Properties of an Arthropod Exoskeleton." *Hysitron.com.* 2012. www.hysitron.com/LinkClick.aspx?fileticket=x-hOMSdlj3E%3d&tabid=324.

DoD. "DARPA Selects Micro Air Vehicle Contractor." *US Department of Defense News Release No. 676-97.* December 12, 1997. http://www.defense.gov/releases/release.aspx?releaseid=1538 (accessed January 2012).

Dumont, E.R., I.R. Grosse, and G.I. Slater. "Requirements for Comparing the Performance of Finite Element Models of Biological Structures." *Journal of Theoretical Biology* 256 (2009): 96-103.

Eaton, J.L. "Morphology of the Head and Thorax of the Adult Tobacco Hornworm, Manduca sexta (Lepidoptera: Sphingidae)." *Annals of the Entomological Society of America* 64 (1971): 437-445.

Ellington, C.P. "Power and Efficiency of Insect Flight Muscle." *Journal of Experimental Biology* 115 (1985): 293-304.

Ellington, C.P. "The Aerodynamics of Hovering Insect Flight VI. Lift and Power Requirements." *Philosophical Transactions of the Royal Society B: Biological* 305 (1984): 145-181.

Enders, S., N. Barbakadse, S.N. Gorb, and E. Arzt. "Exploring Biological Surfaces by Nanoindentation." *Materials Research Society* 19, no. 3 (March 2004): 880-887.

FedScoop. *Time Honors DARPA Projects on 2011 50 Best Inventions List.* November 2011. fedscoop.com/time-honors-darpa-projects-on-2011-50-best-inventions-list/.

FishbowlNY. *Time Lists 50 Best Inventions.* November 2011. http://www.mediabistro.com/fishbowlny/time-lists-50-best-inventions_b47098.

Flannigan, William C. "Finite Element Modeling of Arthropod Exoskeleton." MS Thesis, Department of Mechanical and Aerospace Engineering, Case Western Reserve University, Cleveland, 1998.

Frye, Mark A. "Effects of stretch receptor ablation on the optomotor control of lift in the hawkmoth Manduca sexta." *The Journal of Experimental Biology*, 2001: 3683-3691.

Guiler, Richard W. *BIoinspired Aerostructural Design for In-flight MAV Collison Recovery.* Technical, Andover: Physical Sciences Inc, 2011.

Harvard. *Harvard Microrobotics Laboratory.* 2012. http://www.micro.seas.harvard.edu/research.html.

Hay, J. "Introduction to Instrumented Indentation Testing." *Society for Experimental Mechanics: Characterization of Materials by Nanoindentation Series*, 2009: 66-72.

Hay, J., P. Agee, and E. Herbert. "Continuous Stiffness Measurement During Instrumented Indentation Testing." *Experimental Techniques: Nanomechanical Characteristics of Materials by Nanoindentation Series*, 2010: 86-94.

Highfield, Roger. *The Telegraph.* Jan 31, 2007. http://www.telegraph.co.uk/news/1541106/Bumble-bee-paradox-solved.html (accessed 10 5, 2012).

Hillerton, J.E. "Cuticle: Mechanical Properties." In *Biology of the Integument I. Invertibrates*, by J. Bereiter-Hahn, A.G.Matolsky, & K.S. Richards, 626-637. New York: Springer-Verlag, 1984.

Hoffmann, K. *An Introduction to Measurements using Strain Gages.* Darmstadt: Hottinger Baldwin Messtechnik GmbH, 1989.

Hollenbeck, Alex C. *Evaluation of the thorax of manduca sexta for flapping wing mirco air vehicle applications.* Masters Thesis, Dayton: Air Force Institute of Technology, 2011.

Hollenbeck, Alex, Anthony Palazotto, and Mark Willis. "Evaluation of the Hawkmoth Thorax for Flapping-Wing Micro Air Vehicles." *Dayton Engineering and Sciences Symposium (DESS).* Dayton: Wright-State University OH, 2011.

Ifju, P., B. Stanford, and L. Kyu-Ho. "The Mechanics of Micro Air Vehicle Flexible Wings." University of Florida, 2008. Virginia Tech CSM Conference Presentation.

Jenikova, Zdenka. *Nikon Small World Gallery.* 2005. http://www.nikonsmallworld.com/gallery/year/2005/53 (accessed 2012).

Jensen, M., and T. Weis-Fogh. "Biology and Physics of Locust Flight V. Strength and Elasticity of Locust Cuticle." *Philisophical Transactions of the Royal Society B: Biological* 245 (1962): 137-169.

Kammer, A. E. "The motor output during turning flight in a hawkmoth, Manduca sexta." *Journal of Insect Physiology*, 1971: 1073-1086.

Karpelson, M., G.Y. Wei, and R.J. Wood. "A Review of Actuation and Power Electronics Options for Flapping-Wing Robotic Insects." *IEEE International Conference on Robotics and Automation.* Pasadena CA, USA, 2008.

Khan, Zaeem A., and Sunil K. Agrawal. "Study of Biologically Inspired Flapping Mechanism for Micro Air Vehicles." *AIAA Journal* 49, no. 7 (July 2011): 1354-1365.

Knospe, Carl R. *Insect Flight Mechanisms: Anatomy and Kinematics.* University of Virginia. Fall 1998. people.virginia.edu/~crk4y/research/flight.PDF.

Liu, H., and H. Aono. "Size Effects on Insect Hovering Aerodynamics: An Integrated Computational Study." *Bioinspiration and Biomimetics* 4 (March 2009): 13pp.

loadcelltheory.com. 2012. http://www.loadcelltheory.com/loadCellTheory.html.

Machin, K.E., and J.W.S. Pringle. "The Physiology of Insect Fibrillar Muscle II. Mechanical Properties of a Beetle Flight Muscle." *Proceedings of the Royal Society of London* B 151 (1959): 204-225.

Martin, M., M. Olek, M. Giersig, and H. Schmitz. "Micromechanical Properties of Consecutive Layers in Specialized Insect Cuticle: The Gula of Pachnoda marginata (Coleoptera, Scarabaeidae) and the Infrared Sensilla of Melanophila acuminate (Coleoptera, Buprestidae)." *Journal of Experimental Biology* 211 (2008): 2576-2583.

McMichael, J.M., and M.S. Francis. "Micro Air Vehicles - Toward a New Dimension in Flight." *Unmanned Systems* 15, no. 3 (1997): 8-17.

Meyer, John R. *The Exoskeleton.* Feb 17, 2006. http://www.cals.ncsu.edu/course/ent425/tutorial/integ.html (accessed Oct 05, 2012).

Morisak, J. *Design of a 5th order butterworth low-pass filter using sallen & key circuit.* Jan 12, 2012. http://www.ece.uic.edu/~jmorisak/blpf.html (accessed Oct 05, 2012).

MTS. "Nano Indenter G200 User's Manual." *MTS Systems Corporation.* Doc. No. G2A-13192-0, April 2007.

Mueller, Thomas J. *Aerodynamic Measurments at Low Reynolds Number for Fixed Wing Micro-Air Vehicles.* Instructional, Notre Dame: University of Notre Dame, 1999.

—. *Fixed and Flapping Wing Aerodynamics for Micro Air Vehicle Applications.* Massachusetts: American Institute of Aeronautics and Astronautics, Inc , 2001.

Murray, Jeremy, Ryan O'Hara, and Anthony Palazotto. "The Use of Photogrammetry to Evaluate Dynamic Characteristics of a Manduca Sexta Wing." *Dayton Engineering Sciences Symposium (DESS).* Dayton: ASME, 2011.

Norris, A., A. Palazotto, and R. Cobb. "Structural Dynamic Characterization of an Insect Wing: Toward the Development of Bug Sized Flapping Wing Micro Air Vehicles." *American Institute of Aeronautics and Astronautics,* 2006: 2010-2790.

Oliver, W.C., and G.M. Pharr. "An Improved Technique for Determining Hardness and Elastic Modulus Using Load and Displacement Sensing Indentation Experiments." *Journal of Materials Research* 7 (1992): 1564-1583.

Omega. *The Strain Gage.* 2012. www.omega.com/literature/volume3/strain2.html.

Pennycuick, C.J., and M.A. Rezende. "The Specific Power Output of Aerobic Muscle Related to the Power Density of Mitochondria." *Journal of Experimental Biology* 108 (1984): 377-392.

Ramesh, K.T. *Nanomaterials, Mechanics and Mechanisms.* New York: Springer, 2009.

Reeder, Mark. *International Journal of Micro Air Vehicles.* Vol. 3. Multi-Science Publishing, 2011. Editorial, inside front cover.

Reinecke, J.P., J.S. Buckner, and S.R. Grugel. "Life Cycle of Laboratory-Reared Tobacco Hornworms, Manduca sexta: A Study of Development and Behavior using Time-Lapse Cinematography." *Biological Bulletin* 158 (February 1980): 129-140.

Shyy, Wei. *Aerodynamics of Low Reynolds Number Flyers.* New York: Cambridge University Press, 2008.

Sims, T. "A Structural Dynamic Analysis of a Manduca Sexta Forewing." MS Thesis, Air Force Institute of Technology, Wright-Patterson AFB, OH, 2010.

Sims, T., A Palazotto, and R. Cobb. "A Structural Dynamic Analysis of a Manduca Sexta Forewing." *International Journal of Micro Air Vehicles* 2, no. 3 (September 2010).

Slocum, Alexander. *Fundamentals of Design: Linkages.* Dec 12, 2008. http://web.mit.edu/2.75/resources/FUNdaMENTALs%20Book%20pdf/FUNdaMENTALs%20Topic%204.PDF (accessed Oct 05, 2012).

Steltz, E., M. Seeman, S. Avadhanula, and R.S. Fearing. "Power Electronics Design Choice for Piezoelectric Microrobots." *IEEE International Conference on Intelligent Robots and Systems.* Beijing, China, 2006.

Stevenson, R.D., and R.K. Josephson. "Effects of Operating Frequency and Temperature on Mechanical Power Output form Moth Flight Muscle." *Journal of Experimental Biology* 149 (1990): 61-78.

Stilson, Tim. *5.1 Anti-aliasing.* Oct 17, 1996. https://ccrma.stanford.edu/CCRMA/Courses/252/sensors/node21.html (accessed Oct 05, 2012).

Sun. "High-Lift Generation and Power Requirements of Hovering Insect Flight." *Fluid Dynamics Research* 37 (2003): 21-39.

Sun, J.Y., J. Tong, and J. Zhou. "Application of Nano-Indenter for Investigation of the Properties of the Elytra Cuticle of the Dung Beetle (Copris ochus Motschulsky)." *Institution of Electrical Engineering Proceedings, Nanobiotechnology* 153, no. 5 (October 2006): 129-133.

Sun, M., and G. Du. "Lift and Power Requirements of Hovering Insect Flight." *Acta Mechanica Sinica* 19, no. 5 (2003): 458-469.

Tu, Michael S., and Thomas L. Daniel. "Submaximal power output from the dorsolongitudinal flight muscles of the hawkmoth Manduca sexta." *The Journal of Experimental Biology*, 2004: 4651-4662.

Tubbs, T.B. "Biological Investigation of the Stimulated Flapping Motions of the Moth, Manduca Sexta." MS Thesis, Air Force Institute of Technology, Wright-Patterson AFB OH, 2011.

Upton, James. *Micro Air Vehicles.* Jun 05, 2005. http://people.bath.ac.uk/ju205/mav/flappingwing.html (accessed Oct 05, 2012).

Vincent, Julian F.V., and Ulrike G.K. Wegst. "Design and Mechanical Properties of Insect Cuticle." *Arthropod Structure and Development* 33, no. 3 (July 2004): 187-189.

Wainwright, S.A., W.D. Biggs, J.D. Currey, and J.M. Gosline. *Mechanical Design in Organisms.* Princeton: Princeton University Press, 1982.

Wasserthal, Lutz T. "Flight-Motor-Driven Respiratory Air Flow in the Hawkmoth Manduca Sexta." *Journal of Experimental Biology* 204 (July 2001): 2209-2220.

Weis-Fogh, T. "Tetanic Force and Shortening in Locust Flight Muscle." *Journal of Experimental Biology* 33 (1956): 668-684.

Willis, Mark. Associate Professor of Biology, Case Western Reserve University, Cleveland OH. Personal Correspondence, July 26, 2011.

—. Associate Professor of Biology, Case Western Reserve University, Cleveland OH. Personal Correspondence, February 10, 2012.

Willmott, A.P., and C.P. Ellington. "The Mechanics of Flight in the Hawkmoth Manduca Sexta." *Journal of Experimental Biology* 200 (1997): 2705-2722.

Wood, R.J. "The First Takeoff of a Biologically Inspired At-Scale Robotic Insect." *IEEE Transactions on Robotics* 24, no. 2 (April 2008): 341-347.

WSU. *Wright State Micro Air Vehicle Open House.* March 21, 2011. http://www.webapp2.wright.edu/web1/newsroom/2011/03/21wright-state-micro-air-vehicle-open-house.

Wu, P., B. Stanford, and P. Ifju. "Insect-Inspired Flapping Wing Kinematics Measurements with Digital Image Correlation." *SEM Annual Conference.* Albuquerque: Society of Experimental Mechanics, Inc., 2009.

Zhao, L., and X. Deng. "Power Distribution in the Hovering Flight of the Hawk Moth Manduca Sexta." *Bioinspiration and Biomimetics* 4 (2009): 7pp.

REPORT DOCUMENTATION PAGE	*Form Approved* *OMB No. 0704–0188*

1. REPORT DATE (DD–MM–YYYY) 21-12-2012	2. REPORT TYPE Master's Thesis	3. DATES COVERED (*From — To*) Oct 2010 – December 2012

4. TITLE AND SUBTITLE Evaluation of the Thorax of Manduca Sexta for Flapping Wing Micro Air Vehicle Applications	5a. CONTRACT NUMBER
	5b. GRANT NUMBER
	5c. PROGRAM ELEMENT NUMBER
6. AUTHOR(S) Cranston, Brian C.	5d. PROJECT NUMBER
	5e. TASK NUMBER
	5f. WORK UNIT NUMBER
7. PERFORMING ORGANIZATION NAME(S) AND ADDRESS(ES) Air Force Institute of Technology Graduate School of Engineering and Management (AFIT/ENY) 2950 Hobson Way WPAFB OH 45433-7765	8. PERFORMING ORGANIZATION REPORT NUMBER AFIT-ENY-12-D-03
9. SPONSORING / MONITORING AGENCY NAME(S) AND ADDRESS(ES) Air Force Office of Scientific Research 875 North Randolph Street Arlington, VA., 22203-1768	10. SPONSOR/MONITOR'S ACRONYM(S) AFOSR
	11. SPONSOR/MONITOR'S REPORT NUMBER(S)

12. DISTRIBUTION / AVAILABILITY STATEMENT
APPROVED FOR PUBLIC RELEASE; DISTRIBUTION UNLIMITED

13. SUPPLEMENTARY NOTES This material is declared a work of the U.S. Government and is not subject to copyright protection in the United States.

14. ABSTRACT

The tobacco hornworm hawkmoth (*Manduca sexta*) provides an excellent model from which to gather knowledge pertaining to the development of a Flapping Wing Micro Air Vehicle (FWMAV). One of the major challenges in design of a FWMAV is the energy demanding nature of low Reynolds number flapping flight. Therefore, an understanding of the power required by the flight muscles to actuate the wings is essential for the design of a FWMAV. The *M.sexta* wing/thorax mechanism was evaluated as a mechanical system in order to gain insight to the mechanical power required to produce the full natural wing stroke. A unique dynamic load device was designed and constructed to mechanically actuate the upstroke and downstroke of the *M.sexta* in order to achieve the full flapping motion. Additionally, the forces applied through the flight muscles were directly measured in order to attain the power requirements of the flight muscles simultaneously. The experiment yielded wing stroke amplitudes of + 60 and – 35, which is what is seen in nature during hovering. The DVM and DLM muscle groups were calculated to have a power density of 112 W/kg with the vehicle energy density being 2 W/kg. The power output requirement indicates the need for a lightweight and energy-dense power source/actuator combination for the development of FWMAVs.

15. SUBJECT TERMS
FWMAV, Manduca sexta, MAV, power density

16. SECURITY CLASSIFICATION OF: U			17. LIMITATION OF ABSTRACT	18. NUMBER OF PAGES	19a. NAME OF RESPONSIBLE PERSON Dr. Palazotto (ENY)
a. REPORT U	b. ABSTRACT U	c. THIS PAGE U	UU	148	19b. TELEPHONE NUMBER (Include Area Code) (937)255-3636, ext 4599